An Experimental and Economic Analysis of Electrochemical Technologies to Reduce Greenhouse Gas Emissions

Thesis by

Cody Enslin Finke

In Partial Fulfillment of the Requirements for the degree of

Doctor of Philosophy

CALIFORNIA INSTITUTE OF TECHNOLOGY

Pasadena, California

2020

(Defended July 29, 2019)

Cody Enslin Finke
ORCID: 0000-0002-1343-1737

ACKNOWLEDGEMENTS

I would never have been able to get to Caltech without the good fortune and privilege of having such excellent and supportive advisors, mentors, and friends. First, I would like to thank my PhD thesis advisor Mike Hoffmann for allowing me to have unlimited freedom to work on whatever I wanted. His acceptance of my far afield work allowed me to be creative with problem solving. Also, his willingness to pick me up after dropping out of my MD/PhD program was life changing.

My various thesis committee members Donnie Pinkston, Jess Adkins, Jonas Peters, and Harry Gray were all supportive and nurturing of my ideas and I am very grateful for that. Harry was always kind and encouraging of my ideas. Jonas pushed me to drill down and interrogate all of my assumptions and I am a more honest and better scientist for it. Jess would sit with me in his office for hours as we brainstormed usually ridiculous and sometimes non-physical ideas for technologies that could stop CO_2 emissions today. I would never have had my good ideas without being able to flesh them out with him. Donnie helped me learn to code and was patient with me as I did even the most basic things. With their encouragement and challenging questions, they truly made me feel free to explore academically and respected as a peer. I have grown enormously as scientist form their help.

Caltech also could not be what it is without the support staff including those who helped me do many, many things that I should have done earlier, but did not want to do, but needed to do, like write this very document.

My education and path to Caltech has always been grounded in an interest in chemistry and mitigating environmental pollution. In high school, I had excellent science teachers and one excellent math teacher who helped me think creatively. Freshman year, Heidi Neff taught me laboratory science and she always encouraged me to make connections where I did not see them before. Chanuche Terranella taught me sophomore chemistry and was always willing to talk to me about fringe topics and let my imagination run wild. Melinda Mueller taught me biology and biotechnology and introduced me to genetics. Melinda was able to stimulate my creativity and I still have fond memories of trying to build a climate model with a stella box model program.

Bill woodman helped me integrate math into science in senior year physics class and I loved realizing how important is calculus with him. Don Zwiers was my sophomore year precalculus teacher and he taught me how to think logically about problems. Every time he would demonstrate something in class he would start by saying ‘I don’t know how to figure this out, what are our options?’. That method helped me in math but also notably organic chemistry. Tommy Adams, was my advanced chemistry teacher and I will be grateful for him for telling me to go to Carleton College.

Sophomore year when Cameron McCulloch joined my class my grades really boosted. His study habits were excellent and I glommed onto him and he taught me how to work hard and have good humor about it. We are still best friends today. Oliver Miska has been my best friend since high school and he has always reminded me to think about my life in the context of the world.

At Carleton I was again blessed with excellent mentors and friends who helped me learn collaboratively. Professors Gretchen Hoffmeister, Daniela Kohen, and Stefan Zweifel were all amazing teachers and supporters. Matt Rand also encouraged me to start a business (although he probably doesn’t remember) and Matt Whited encouraged me to go to Caltech and learn about energy. All of them were approachable and creative. Stefan especially helped me see the fun in science. I am grateful for their mentorship. I also should thank my friends who spent long hours in the library and the chemistry conference room helping me learn things that I did not understand especially Erik Olson, Kenneth Lum, Kaz Scubi, Owen Demke, Sean Roberts, Sam Althauser, and Allie Cardiel who all taught me to be a better student and chemist.

At Caltech friends post docs and graduate students taught me all the electrochemistry I know including Sonja Francis, Justin Jasper, Clement Cid, Hugo Leandri, Axl Le Van, Sean Seungkyeum, David Zheng, Kangwoo Cho, Yan Qu, Jackie Dowling, and Many others. Other Mentors like Neil Fromer and Stephanie Yanchinski helped me grow to think about the big picture and the pesky non-scientific details that are preventing us from transitioning to clean energy.

Finally, I want to thank my amazing community of friends and my partner who helped me get into the mountains enough to stay motivated and sane. Nafeesa Andrabi, Matt Shaner, Stefan

Omelchenko, Teddy Albertson, Ben Broer, Graham Baskett, Thuy Jacobson, Aaron Cooper, Patrick Gasparro, Justin Jasper, Marisa Palucis, Aaron Markowitz, Hayden Miller, Jennifer Buz.

ABSTRACT

Global warming and the related problem of water scarcity are predicted to cause widespread environmental, humanitarian, and economic challenges. New technologies may be able to reduce greenhouse gas emissions enough to prevent many of the worst consequences of climate change However, in order to be competitive in the market, new, low emissions technologies must be affordable. In this thesis, I present work on building a technology to lower the cost of decentralized, electrochemical wastewater treatment technologies by improving maintenance. I also show that atomic layer deposition of TiO_2 can be used to tune the catalytic activity and stability of multiple electrocatalysts for both the chlorine and oxygen evolution reactions (two of the most common electrochemical reactions used in industry). With more development, this phenomenon has the potential to be used to reduce the cost of many electrochemical systems. I modeled the techno-economics of a low-cost industrial hydrogen production technology and found the first process, to my knowledge, which is able to make industrially relevant quantities of cost-competitive clean hydrogen. I conclude by urging researchers who are trying to solve environmental problems to consider the potential for the cost of the entire technology to be competitive with existing technologies. Finally, I propose that cogeneration of hydrogen and other chemicals may be a viable strategy to producing large quantities of inexpensive, clean hydrogen.

PUBLISHED CONTENT AND CONTRIBUTIONS

Chapter three was reproduced from:

Finke, C. E.; Omelchenko, S. T.; Jasper, J. T.; Lichterman, M. F.; Read, C. G.; Lewis, N. S.; Hoffmann, M. R. Enhancing the Activity of Oxygen-Evolution and Chlorine-Evolution Electrocatalysts by Atomic Layer Deposition of TiO_2. *Energy Environ. Sci.* **2019**, *12* (1), 358–365. https://doi.org/10.1039/C8EE02351D.

with permission from the Royal Society of Chemistry.

Finke, C. E. participated in the conception of the project, conducted electrochemistry work, contributed to sample preparation, and prepared initial manuscript drafts.

Omelchenko, S participated in the conception of the project, developed sample recipes, prepared samples, and prepared initial manuscript drafts.

Jasper, J. T. aided in electrochemistry work and helped edit manuscript drafts.

Lichterman, M. F. helped in solid state analysis.

Read, C. G. preformed TEM work.

Lewis, N. S. edited and provided critical feedback to the manuscript.

Hoffmann, M. R. participated in the conception of the project, edited and provided critical feedback to the manuscript and funded the project.

TABLE OF CONTENTS

NOMENCLATURE

Non-sewered. Wastewater systems that do not involve the use of a sewer.

Levelized Cost. The price that a product must be sold in order to break even with capital and operating costs assuming a discount rate and lifetime of a producing plant.

Discount Rate. The rate of return that is required to break even on investment.

Evolution. The chemical production of a species (e.g. oxygen evolution)

Chapter 1

Introduction

The Greenhouse Gas Problem

Anthropogenic emissions of greenhouse gases are diverse in type and source, some types being more difficult to eliminate than others[1]. Growing concentrations of greenhouse gases in the atmosphere are leading to global warming and it is unknown exactly what this may cause, but best estimates indicate that global warming has the potential to raise sea levels, increase storm frequency and intensity, increase drought and flooding, and inflict grave economic, humanitarian, and environmental damage by the year 2100[2]. In terms of cumulative global warming potential, the largest anthropogenic greenhouse gas is carbon dioxide (CO_2; ~80%) followed by methane (CH_4; ~10%) and nitrous oxide (N_2O; ~5%) and then a diverse suite of compounds, especially halogenated organic molecules[2]. Each greenhouse gas molecule is associated with its own set of mitigation challenges.

Approximately 70% of the total greenhouse gas emissions are CO_2 from burning fossil fuels. CO_2 emissions from fossil fuel combustion, like greenhouse gas emissions in general, are diverse. Fossil fuels are burned as a transportation fuel (14% of total emissions), for electricity generation (20% of total emissions), for heating buildings with low grade heat (20% of total emissions), and for heating industrial processes with high grade heat (20% of total emissions)[2]. Each of these categories are also not monolithic. Electricity, for example, includes base load power plants (constant output, low cost, low ramp rate), load following (demand based output, mid cost, mid ramp rate), and peaker plants (low capacity factor, high cost, high ramp rate), captive generation (onsite electricity generation at a chemical plant), and others. The remaining, non-fossil-fuel fraction of CO_2 emissions are process CO_2 (i.e. CO_2 produced stoichiometrically as part of an industrial chemical reaction). Process CO_2 is primarily emitted by the production of hydrogen, cement, and metals. This means that even with clean sources of heat and electricity, process CO_2 emissions would not be eliminated. As such, process CO_2 emissions are generally thought of as difficult to decarbonize[1].

CH_4 emissions are primarily fugitive emissions from leaky processes involving natural gas (e.g. hydrogen production, electricity production, and natural gas extraction and transportation). It is thought that with improved sensing and pipe fixes, these emissions could be substantially decreased.

Anthropogenic N_2O emissions are largely due to incomplete reduction of NO_3^- by microorganisms after fertilizer addition[3]. These emissions are also considered difficult to remove with strategies mostly revolving around more controlled fertilizer practices such that fertilizer uptake matches fertilizer demand[4].

My dissertation focuses on the largest fraction of greenhouse gas emissions, CO_2, by exploring ways to make the electrification of industrial processes cheaper. First, I develop a maintenance technology which could reduce the cost of an electrified wastewater treatment system. Second, I present a method to tune electrocatalysts that maximizes their efficacy for processes that produce key commodity chemicals including hydrogen, caustic soda, and chlorine. Finally, I develop a model to understand the economics of electrochemical hydrogen generation, a process that has the potential to reduce greenhouse gas emissions by roughly 80 percent. The chapters in this thesis are guided by thinking about near-term solutions to climate change which can both compete in and integrate into the market with existing technologies.

Important Concepts and State of the Field

Strategies for Reducing Energy Related Emissions

One strategy for CO_2 emissions reduction is the electrification of energy. Electricity can be generated fairly cheaply via solar and wind energy, in some cases for $0.01 to $0.02/kWhr, and turned into low or high grade heat by applying a potential to a resistor[5]. These prices are cheap enough to compete with electricity when the renewable source of electricity is available. However, when electricity is needed outside of that availability, the price of storing that electricity becomes far more expensive (commonly > $0.20 /kWhr) than simply generating that electricity by burning fossil fuels[6]. Similarly, making heat by burning fossil fuels is considerably cheaper (~$0.12/kWhr) than making electricity due to both the reduced capital cost of boilers compared with generators and increased efficiency of not needing to do the energy conversion from heat to electricity. A good heuristic is that heat energy is 5X cheaper than electricity from fossil fuels[7]. Generating heat from electricity is nearly 100% efficient but due to the price of electricity it is still not cheap enough to compete with other types of heat. However, with dramatic cost reductions in both energy demand and storage, clean electricity could replace all energy-related CO_2 emissions.

Strategies for Reducing Process Emissions

The process CO_2 emissions largely come from thermal decomposition of limestone to make cement, the reductive thermal decomposition of iron oxides to make iron metal, and the hydrolysis of methane to make hydrogen[1]. The process emissions associated with these reactions are responsible for around five, two, and one percent of global greenhouse gas emission respectively[1]. In these processes, electrification cannot solve the problem because the greenhouse gas emissions come as a direct result of the chemistry, not from making energy to power the chemistry. New chemistry or carbon capture and storage is necessary to eliminate these process CO_2 emissions.

Economic Realities of Reducing Greenhouse Gas Emissions

While electrification is a promising pathway to reducing greenhouse gas emissions, new and low-CO_2 technologies still will likely need to compete in the marketplace with existing CO_2 intensive technologies. Some countries, like Canada, have introduced a carbon tax or tax credits to help facilitate this process[8,9]. However, taxes are policy decisions that can be repealed; as such, it may be risky to rely on taxes to be profitable. New, low emissions technologies must not only reduce CO_2 emissions but also be cheaper than current technologies if they are to be widely adopted in the near-term.

In some cases, a cost competitive solution may still not be cheap enough to be considered a viable replacement. Many emissions reduction scenarios require decommissioning existing CO_2 generating plants and commissioning new clean technologies. However, the cost of a product is calculated by assuming a known lifetime of a plant and allowing the CapEx to depreciate over the lifetime of that plant. If a plant is decommissioned early, it raises the effective price of that commodity considerably. In order to allow for decommissioning plants, the "low carbon" solution must be cheap enough to offset the entire price of decommissioning. A good heuristic is that the levelized cost of a given commodity must be 70% less than the levelized cost of a current commodity to make replacement of existing technologies worth the financial burden of decommissioning. New low-emissions technologies are often too expensive to compete with their high emission counterparts. The cheapest strategy to reduce emissions then immediately becomes carbon capture and storage or utilization which sometimes has low cost estimates of around $100 per tonne of CO_2[10].

Carbon Capture, Carbon Storage, and Carbon Utilization

Even if new technologies are cheap, simply reducing or even eliminating anthropogenic greenhouse gas emissions in the near term may not be enough to mitigate the potential impact of

global warming. The residence time of CO_2 in the atmosphere is between 20 and 500 years depending on the rate of carbon burial. Under business as usual cases, the symptoms of climate change are likely to persist long after the CO_2 faucet is shut off[11]. In this case, carbon capture and utilization or symptom management are the main viable options.

Climate Change and Water

There is continued uncertainty around the tangible and lasting consequences of climate change. While admittedly we cannot predict the future, one major symptom of climate change is likely to be increased water scarcity. The precise degree to which global warming will redistribute water is unknown. The best approximations suggest that the general trend is for freshwater to precipitate more intensely, less frequently, and more often as liquid (e.g. rain) than solid (e.g. snow), though major climate models disagree about the magnitude[12]. This means that the frequency of both drought and flooding are likely to increase with a warming globe while natural water storage (e.g. seasonal snowpack) is likely to decrease[12]. More intense rain also gives less time for water to be absorbed into aquafers, causing more water to run to the ocean[12]. Furthermore, many estimates believe that the world population is likely to increase meaning that under a business as usual scenario, water demand and water pollution will likely also increase[12].

Preview of the Chapters

This thesis is broken into three projects centered around the idea of electrifying industrial processes and making solutions to global environmental problems cheaper and therefore more realistic. In the following sections, I provide context and background for each project as well as a brief preview of the chapter.

Electrochemical Wastewater Treatment

Water scarcity is an especially large problem in low income countries where there is minimal existing wastewater treatment infrastructure. Where water treatment is scarce, the existing water resources are at risk of becoming contaminated by human waste resulting in pollution driven water scarcity. Modern wastewater treatment relies on sewers to convey waste to centralized wastewater treatment plants. In general, when communities are built without adequate sewering, and when water treatment is scarce, it is far more expensive to retrofit than to install at the time of building. Water scarcity driven by water pollution may be best addressed by finding economical non-sewered

wastewater treatment solutions. In this chapter, I discuss the lack of sustainable maintenance solutions, one of the factors that drives up the cost of an electrochemical wastewater treatment system such that it is too expensive to be widely implemented. I introduce a novel technology that utilizes remote sensing to diagnose system failures and offers immediate instructions for fixing the complex electrochemical system that can be used by all individuals, regardless of education level or engineering background.

Typical wastewater treatment involves removing organic pollutants, removing phosphorous, and removing ammonia. Biological, chemical, and physical processes are capable of removing these components.[13] Biological components are generally passive, cheap, slow, and deliver low quality water while chemical and physical processes are energy intensive, expensive, fast, and deliver high quality water.[14] Most complete systems involve biological preprocessing to remove the contaminant followed by various advanced oxidation or filtration processes to treat the water to a standard suitable for reuse.

The two major advanced oxidants are Reactive Chlorine Species (RCS) and Reactive Oxygen Species (ROS). RCS are a good choice for an oxidant because, unlike ROS and many other oxidants, they will oxidize ammonia to N_2 and not beyond via breakpoint chlorination.[15] They therefore remove ammonia without producing polluting NO_x species. Unfortunately, RCS cannot mineralize carbon and instead end with halogenated small organic molecules or acids which are often toxic or carcinogenic (e.g. chloroform). ROS generation, which can be done electrochemically using ozonation, electro-fenton, the peroxone process, and others, may mineralize carbon.[16] Phosphate may be removed electrochemically if the hydrogen evolution reaction is present because it creates a localized zone of high pH where phosphate can precipitate as a salt of calcium, sodium, magnesium, or other cations in solution.[17]

In the Hoffman Group's wastewater treatment system, we include a biological pretreatment step (anaerobic bioreactor) followed by both a RCS polishing step and then a ROS polishing step.[18] This step involves using wastewater as an electrolyte and directly producing hypochlorous acid and hydrogen electrochemically in solution from sodium chloride.[18] This step breaks down the organic molecules, removes ammonia, and precipitates out the phosphate at the cathode[18].[19] After the RCS step, we use another electrochemical system to generate reactive oxygen species which will

mineralize the halogenated organic compounds.[19]. The final product is clear, disinfected, mildly salty water which is ready for reuse or for disposal.

As part of my thesis work, I traveled to India in 2014 and 2015 to help install and maintain prototype water treatment systems. One prevalent issue in implementing this system was poor maintenance. Field sites often relied on chemists and engineers to fly in, diagnose and fix the system due to the complexity of both the chemistry of the process and the construction of the system. It became clear to me during my fieldwork that for our, and any wastewater treatment system to be successful in the long-term, we needed to find a maintenance solution that would allow individuals with minimal education and engineering background to fix a complex electrochemical system. For this project, I applied for and was granted a Wireless Innovation Prize from Vodafone. I am proud to say that the technology which I helped develop is now being implemented in the field in South Africa.

Catalyst improvements for cost reduction in electrochemical oxygen and chlorine generation

Two important electrochemical reactions that have gained considerable attention are water electrolysis (equation 1) and the electrolysis of brine (equation 2).

$2H_2O \rightarrow 2H_2 + O_2$ (equation 1)

$2NaCl + 2H_2O \rightarrow Cl_2 + H_2 + 2NaOH$ (equation 2)

Water electrolysis is compelling because it could provide an “unlimited”, “clean burning” fuel to replace fossil fuels and organic reductants and therefore has the potential to reduce greenhouse gas emissions by up to 75%[2]. The Chlor-Alkali process has garnered attention because it is responsible for producing >95% of the world’s chlorine and caustic soda and ~3% of the world’s hydrogen[20]. This process also consumes around 2% of the world’s electricity demand.[20] Finally, it is one of the important reactions for electrochemical wastewater treatment. Given the potential impact of these processes, attention should be given to cost-reduction strategies to make these processes economically viable in the near-term (i.e. catalyst improvement).

While the Chlor-Alkali process is already a large-scale reality, neither making hydrogen via water electrolysis nor electrolyzing wastewater are large scale industries. The problem, as is often the case, is that these technologies are too expensive to compete in the market.[21,22] Making a better catalyst could reduce the cost of these systems. There are many approaches to improve a catalyst. However, it is not always clear what approach should be used for a given reaction.

In any electrochemical system, the relationship between product produced (i.e. hydrogen or chlorine) and energy and resources consumed is controlled by the catalyst. The quality of the catalyst is dictated by the initial cost of the catalyst (C_m), the applied-potential versus current-density relationship ($V_E + \eta_{0,j,E}$), the faradaic efficiency of the catalyst (ε; the fraction of current that goes to the reaction of interest) and how all of these factors change over time in a given electrolyte (E), at a given current density (j). For a given catalyst, the total operational and capital cost associated with the catalyst (C_T) given a operation time (t) can be calculated using equation 1 where A is the amount of the material (area units) and C_e is the cost of electrical energy.

$$C_T = \int_0^t A\left(C_m + \frac{C_e * j}{\int_0^t (\varepsilon_{0,E,j} + \frac{d\varepsilon_{E,j}}{dt})\,dt} * \int_0^t \left(V_E + \eta_{0,j,E} + \frac{d\eta_{j,E}}{dt}\right)dt\right)dt \quad (1)$$

This relationship can be used to calculate the total cost associated with the catalyst over the lifetime of the plant (t), by multiplying the integral and dividing by the plant lifetime by the number of times the catalyst is replaced (x), equation 2.

$$C_T = x * \int_0^{t/x} A\left(C_m + \frac{C_e * j}{\int_0^{t/x} (\varepsilon_{0,E,j} + \frac{d\varepsilon_{E,j}}{dt})\,dt} * \int_0^{t/x} \left(V_E + \eta_{0,j,E} + \frac{d\eta_{j,E}}{dt}\right)dt\right)dt \quad (2)$$

This equation can be solved numerically for the cheapest possible number of times that a catalyst should be replaced in a given plant lifetime. Having the ability to tune the parameters of the catalyst (e.g. ε, η, and C_m) would allow us to optimize for the most important parameters. In chapter three of my thesis, I present work on tools to tune these parameters which could allow for a cheaper catalyst configuration. Utilizing novel catalyst tuning methods, there is potential to bring the cost of water electrolysis and electrochemical wastewater treatment via chlorine evolution closer to a market-competitive price.

Near-term, cost effective electrification of hydrogen generation

Hydrogen is the most demanded commodity chemical in the world, and a co-product of the electrolysis of both brine and water.[23] Currently, hydrogen is primarily produced from natural gas via Steam Methane Reforming (SMR) which produces 1) process CO_2 responsible for around 1-2% of global CO_2 emissions and 2) heating CO_2 which is responsible for another 0.5-1% of global emissions.[24] Hydrogen also has the potential to replace hydrocarbons as a chemical reductant used

in processes like iron refining which could eliminate another 3-5% of global CO_2 emissions in the form of process CO_2.[1] The example of iron refining illustrates the importance of driving down the cost of hydrogen. Iron production typically uses petroleum coke which can deliver 4-5 mols of electrons per mole of petroleum coke (petcoke).[25] Hydrogen can deliver 2 moles of electrons per mol. There are about 333,000 mols of electrons in a tonne of petcoke. Petcoke costs around $70/tonne meaning that petcoke costs around 0.02 pennies per mol of electrons.[26] Hydrogen has ~1,000,000 mols of electrons per tonne and costs around $125 per tonne meaning that hydrogen electrons cost around 0.01 pennies per mole of electrons.[26] Unfortunately, hydrogen is made from natural gas which is an even cheaper reductant and is beginning to replace petcoke in iron refining.[27] Hydrogen, of course, could replace more than the very difficult to decarbonize process CO_2 emissions. If it were to be produced cleanly at large scale, H_2 could replace all fossil fuels as a low or no emissions source of thermal and electrical energy.

It is well studied that making hydrogen via water electrolysis has a very narrow pathway to being cost competitive with hydrogen produced from SMR.[21,26] In fact, the only electrolytic processes that has proven hydrogen production economics is Chlor-Alkali. Electrochemical processes are not widely used in industry with the exception of the Chlor-Alkali, Metal Electrowinning, and a few niche, high value products like Adiponitrile.[21] It is difficult to find a widespread pattern for why some processes are electrochemical and some are thermochemical (e.g. alumina production is electrochemical while iron production is thermochemical). In many cases, economics likely has more to do with what process was figured out first and is now the more mature technology. The key to making an electrochemical technology effective is making it cheaper than the thermochemical competition and of course, a thermochemical process may also be electrified and decarbonized if resistive heat is used.

Despite a lack of a clear economic pattern in industrial electrochemical technologies hinting at how to make electrochemical hydrogen cheap, I believe that it may be useful to more closely examine the Chlor-Alkali process. Many studies cite the fact that the energy intensiveness of water electrolysis is driving the high cost.[26] Industrial size electrolyzers make hydrogen at 55 kWhr/kg while SMR reactors require only 35 kWhr/kg (heat converted into standard electricity units), making electricity a major contributor to cost [26]. However, the Chlor-Alkali process requires 70 kWhrs/kg H_2, far more electricity than water electrolysis, yet still makes cheap H_2.[20]

Electrolysis plants are also expensive because of high CapEx. A 400,000 kg H_2 per day electrolysis plant is estimated to have a CapEx of around 700M USD while an equivalent SMR plant capable of making 7X that much H_2 per day has a CapEx of only 180M USD[26]. High CapEx means that money must be spent now, not later and therefore the value of the spent money is higher. The reason that the Chlor-Alkali process can make cheap hydrogen despite high CapEx and energy consumption is that it makes three products for a single CapEx and energy consumption: chorine, caustic soda, and hydrogen. Cogeneration can allow electrochemical processes to outcompete existing fossil-based thermochemical processes. The fourth chapter of my thesis explores how cogeneration can be used to make electrochemical hydrogen production profitable in the near term via cogeneration of hydrogen and sulfuric acid.

Contribution/ Significance

Under current IPCC emissions scenarios, the problem of greenhouse gas emissions is urgent.[12] The longer it takes to develop solutions to greenhouse gas mitigation the worse things may get. Therefore, it is important to work on problems that are likely to have a near-term impact. This thesis attempts to determine whether or not current ideas for mitigating greenhouse gas emissions are near term, and if they are, how to make them cheaper immediately.

Chapter 2

Towards Engineering an Electrochemical Wastewater Treatment Technology Suitable for Long Term Deployment in the Developing World:

Cody E. Finke Eitam Shafran, Hugo Leandri, Clément Cid, Anastasia Hanan, Michael R. Hoffmann

Data presented in this chapter was primarily collected by ES and HL

Background and State of the Technology

The UN estimates that by 2025, the combined stresses of population growth and climate change may force as many as 1.8 billion people into absolute water scarcity on the Falkenmark Indicator (FI), meaning there may not be enough runoff or water storage in a region to support basic human activity (<500 m^3 water/capita/yr)[28]. Additionally by 2025, according to the UN, two thirds of the world's population will be forced into water stress on the FI meaning not enough water to support economic growth (<1700 m^3 water/capita/yr)[28–30]. Water scarcity like this will likely almost exclusively occur in the developing world where reverse osmosis or other water desalination/recycling methods are not financially or infrastructurally feasible. Physically, >1.8 billion people are predicted to get sick and millions of people are predicted to prematurely die from, out of necessity, drinking water polluted with human waste or from simply not having enough water. Economic growth in these regions may further stagnate as industries ranging from manufacturing to farming to mineral extraction may struggle to operate without sufficient water, compounding health and environmental damage. Beyond the direct anthropocentric problems associated with water scarcity, when there is not enough water to sustain human life, all the water tends to be syphoned away from the other species of the world causing myriad ecological crises. This can already be witnessed across the globe: the keystone riparian habitats of the now dry Lake Chad and Colorado River Delta are just two of many examples. Given that many models estimate that the world population is unlikely to stabilize until sometime after 2100[31] and given that the effective residence time of CO_2 in the atmosphere is about 400 years[32], the problem of water scarcity is likely to get worse for at least a century before it starts to get better. One possible solution for these billions of

people and ecosystems is a major new water management strategy that is feasible in the developing world.

Solutions fit for the developed world do not always translate to solutions for the water crisis in the developing world; the key in the developing world is infrastructure-free wastewater treatment and recycling systems. In developed countries, desalination, water catchment, and wastewater recycling technologies are all relatively affordable. Furthermore, the massive water and wastewater grid infrastructures required for these technologies already exist. This is why, for example, the people of the American Southwest feel almost no effect of the recent five year drought despite population growth in all Southwest states exceeding the national average of 9.6% between 2000 and 2010, in many cases by a factor of 2 or 3[33]. This is also why Israel and Saudi Arabia are experiencing almost no water scarcity despite being countries that are over 60% desert. The situation in developing countries is very different. In many cases there is little to no existing water grid infrastructure and the commercially available water recycling and desalination technologies are fiscally prohibitive. As such, new water management solutions must be created for the developing world. While water in these regions is occasionally scarce because it is missing, some estimates find that it is more often scarce because it has been contaminated with human waste due to no or poor sanitation facilities[34]. Sanitation (defecating, urinating, and body washing) is very water costly. In highly water scarce and impoverished regions, one study finds that, on average, sanitation accounted for 69% of personal water use[35]. In other words, for the 1.8 billion people that may be in absolute water scarcity by 2025, poorly managed toilet wastewater will likely be the dominant problem and a management plan that involves water recycling for sanitation is the key to preserving human and ecological health. Therefore, it has become the major focus of the water resource technology field to find inexpensive and infrastructure-free ways to eliminate water consumption due to sanitation and treat wastewater in the developing world.

2.5 billion people across the developing world lack access to any type of improved sanitation facility[36]. Therefore, one attractive strategy to conserve water in the developing world is the development of inexpensive, non-sewered sanitation technologies that recycle their water. To this end, many technologies have been developed. Highlighting a few examples: the Hoffmann group at Caltech has developed an electrochemical water treatment and toilet system for home or small public spaces; Janicki Bioenergy has developed a city-wide bio-char omniprocessor treatment system, and Marc Deshusses' group at Duke has invented a water neutral anaerobic bioreactor and toilet system

for household use. Every system has its problems. Bioreactors and bio-char systems both are attractive because they offer potentials for selling fertilizer byproducts. However, due to the high water content of waste, in practice, bio char facilities require too much energy to reasonably maintain (~3,600 Wh per kg for biochar vs ~30 Wh per kg for electrochemical)[37]. Bioreactors have very low energy consumption metrics, however, on the other hand do not satisfactorily kill pathogens (~1.5 log removal of fecal coliform for anaerobic bioreactors vs non detectible fecal coliform for electrochemical systems)[38]. Electrochemical systems, suffer from reduced activity and catalyst fouling and the production of toxic decontamination byproducts including halogenated organic acids. One problem that is common to all systems is maintenance. The problem of maintenance is well established for high tech solutions to problems in the developing world[39]. Taken together, these affordable systems can recycle wastewater for sanitation purposes without any grid infrastructure and therefore have the potential to secure sustainable water resources for nearly one third of the world's human population and many other ecosystems. Unfortunately, these technologies standing alone are estimated to be prohibitively expensive when maintenance costs are included.

Addressing the Maintenance Problem

One major challenge in operating these systems is maintenance. Experience from field testing treatment units by the Kohler Company and from the Research Triangle Institute has shown that even with extensive one on one training for a month, a master's level engineering degree is necessary to independently diagnose and repair these advanced wastewater treatment systems (personal communication, unpublished data). Given the dearth of master's level engineers in the developing world and the high cost of master's level labor, this makes maintenance impossible at a large scale. The problem of maintenance is also a well-established problem in high tech solutions to problems in the developing world, in fact, breakage with no maintenance is the number one reason why high tech solutions fail[39]. To address this problem, I developed a concept to use a suite of sensors to uniquely link states of the system to specific failure states. Then, simple pictorial repair instructions may be passed to an operator via the mobile phone network. This approach is very useful because, given that the world bank estimates that there are 96 mobile phone subscriptions for every 100 people in the world, it is reasonable to assume that there is at least one skilled mobile phone operator almost everywhere in the world (Fig. 1). For this proposed work, I won the 2013 Vodafone

Wireless Innovation Project Competition which contained a $300,000 grant to develop the project. Using this money, we designed and demonstrated a proof of concept prototype in the lab which is currently being integrated into existing systems for full-scale testing as a self-diagnosis and maintenance technology.

Device Concept

1) A Server which operates in the following way:

   Failure code and unit coordinates allow the server to establish communication with the wastewater treatment unit's operators and users. After receiving the data from the unit's computer, an SMS text is sent to the operator of the malfunctioning system with the following information: "Unit X in need of maintenance, failure mode number Y". This addresses the identified problem and the unit location. A second SMS is sent to the users of the system, referring them to an alternative location of a different unit, while the system is being repaired. The server will be capable of the following specific tasks:

   a) Will store information on maintenance technicians and users like name, contact information, and toilets that she is taking care of
   b) Will store information on treatment systems like location, failure status, and data after failure
   c) Will link operators to toilets that they take care of
   d) Will contact a technician when a toilet breaks to come fix the toilet
   e) Will contact users with other options to use the bathroom when a preferred toilet is broken
   f) Will provide a user interface to add and edit toilets and operators

2) A treatment system client which is described as:

   A network of sensors integrated in key locations inside the sanitation system. These sensors will monitor different water quality parameters during the wastewater treatment process, in addition to monitoring the electrical devices, pipes and containers for malfunctions. Data will be sent to

the onboard computer. During system operation, the onboard computer will send continuous "Ok" messages to the server, utilizing the mobile network or a wireless connection to report that no problem has been detected. In case of a malfunction, the computer will send a failure mode code and the unit coordinates to the server, followed by the data set collected during the last 24 hours before the malfunction. The client will be capable of the following specific tasks:

a) Will collect data on a suite of sensors
b) Will process sensor data to determine if and how the toilet system is broken
c) Will send failure status information to the server
d) Upon failure will send raw sensor data to the server
e) Will determine when the system has been fixed and restart standard operation

3) A mobile based application which is described as:

For system maintenance, the operator will be directed to the malfunction by the application. Utilizing the application and its displayed simple pictorial repair instructions, the operator will be enabled to fix the malfunction. After successful repair, the unit computer will resume sending “OK” messages to the server and inform the users.

Integration of the monitoring system to the sanitation unit will provide two main additional benefits:

1) With real-time monitoring of the water parameters, we can optimize the wastewater treatment process, allowing us to identify the optimal point in time to stop and to start every step of the electrochemical treatment. As a result, the creation of potentially harmful byproducts and the overall energy consumption of the system can be lowered.[1]
2) Creation of a local economic system of users and local operators with the common goal of keeping the sanitation units maintained.

In this report, we focus on the self-diagnosis stage of the system, addressing the system requirements, work that has been completed, challenges that occurred and planned future work.

The sensors included in the self-diagnosis system can be divided into three groups: (i) water quality measurement sensors which provide information on the status of the electrochemical treatment; (ii) humidity and level sensors which monitor the system for

leakages; (iii) voltage and current sensors which monitor the status of the electrical parts of the system.

a) Receive prompts from the server if the system fails
b) Automatically order a spare part for delivery to the unit
c) Store pictorial repair instructions for all possible repairs to minimize data sent over the network
d) Prompt a technician with an easy to follow set of repair instructions

Process Design

Long Term Proposed Project: An adequate solution to the problem of system maintenance must be simple, adaptable to many diverse treatment technologies, universally available, inexpensive, and quick. The World Bank estimates that as of 2014 there are 96.3 mobile phone subscriptions per 100 people in the world. In other words, there is likely at least 1 working phone with a skilled phone operator in every community everywhere on earth[40]. Our proposed technology would capitalize on the mobile network to diagnose maintenance issues and guide a toilet operator to fixing problems with non-sewered water treatment technologies. Self-diagnosis works in these treatment systems because the problem of water treatment is well constrained and easily monitored, especially as the water only needs to be sterile, odorless, and clear to recycle for sanitary purposes, not necessarily potable. Therefore, the problem becomes monitoring water quality which can be inverted for with clarity and turbidity, monitoring oxidant production which can be inverted for with current, pH, temperature, and oxygen content, and finally monitoring pathogen content which can be inverted for using the previous measures combined. The rest is a simple matter of assessing mechanical failure. The full algorithm for wastewater treatment monitoring is described in words as follows: each pipe has a leak sensor, each tank has a water level sensor, each pump has a pressure sensor, every electronic component has a multimeter, treated water clarity and turbidity sensors, and then each system has an oxidant production sensor. Caltech's unit would have an ammeter to detect current at the electrodes, Duke's system would have an oxygen meter to ensure respiration was depleting the oxygen of the system and a pH meter to ensure the fermentation was not occurring without methanogenesis, and Janicki's system would have a thermocouple and oxygen meter to ensure

temperatures were being reached in the presence of oxygen (a diagram of the Duke and Caltech sensor configuration is in Fig. 1). All sensors are commercially available.

A common problem with self-diagnosing technologies is sensor failure before part failure. Our system will address this issue in two ways. First, sensors will be installed in duplicate in physically distinct locations such that if one sensor gets physically damaged, the second sensor will likely still be functional. Then if the two sensors are reading significantly different values, the operator will be instructed to replace the sensors. The second safety check will be routine "dry runs" where a water free short run of the system will be conducted which, if sensors are working properly, trigger universal failure signals. If any sensor fails to give a failure signal, it will be replaced.

Once a unique failure mode is identified by the onboard processor, an SMS will be sent to the operator notifying her that the system is broken, and that the operator should go attend to the system ASAP. Similarly, the system will send an SMS to the users notifying them that the system is broken and identifying other toilets to use while it is being fixed. This creates a "wastewater recycling smart grid" where even in the absence of sewers there is never a time where people will need to resort to non-recycled water for their sanitation needs.

Once the operator arrives at the broken treatment system, she will go to the onboard display and see a series of step by step instructions on how to replace the broken parts and get the system running again. Or, if the operator has a smartphone (a recent Pew Research Center poll suggests smart phone use now represents a significant and rapidly increasing minority of phone users across the developing world[41] the operator will see the repair instructions on the smartphone app (images of this app can be seen in Fig. 2).

The technology will be first developed using bench scale partial models of the systems and sensors and then moved to the full system model on Caltech's campus. Once trouble-shooting and local field testing are complete, the system will be installed in field testing at water treatment locations in India using Caltech's units as well as any other non-sewered sanitation units that are willing to participate. Success will be measured by comparing days where the system is not functional with and without the self-diagnosing system and a decrease in the cost of repairing the system.

When successful, this technology will have the power to empower anyone with a mobile phone and a basic set of tools with the guidance they need to repair any water treatment system with the diagnosis technology installed.

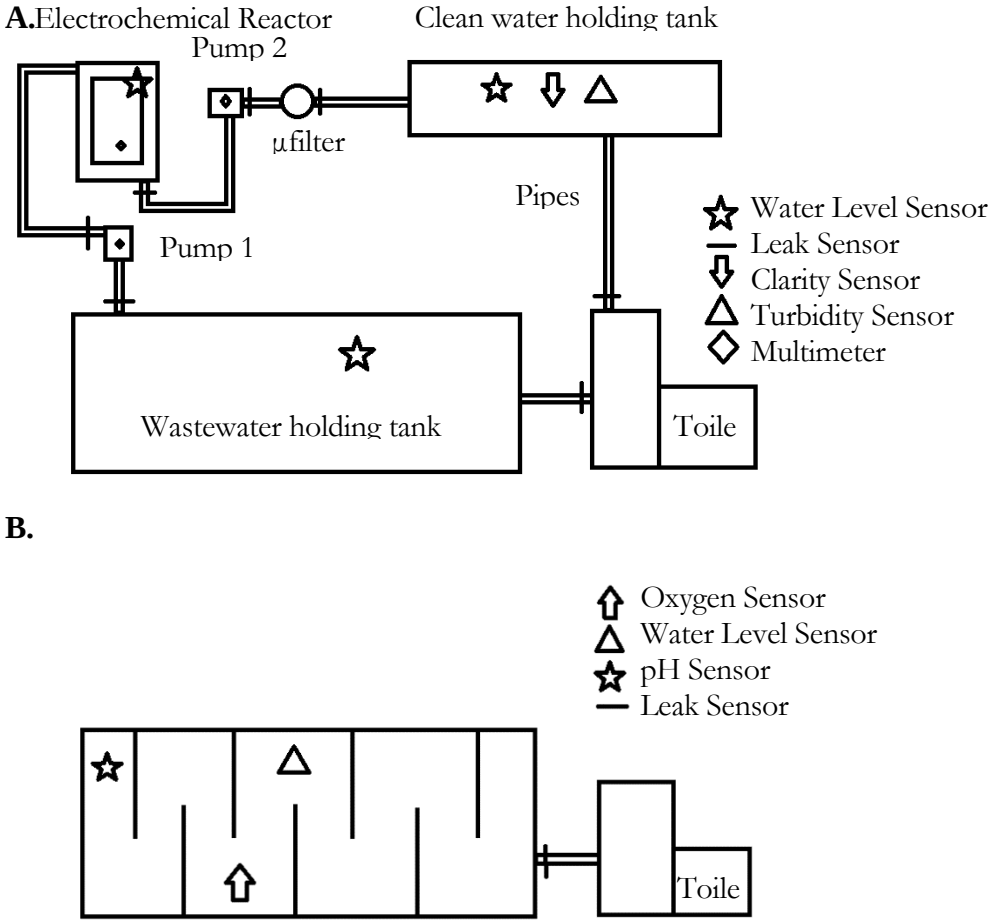

Fig. 1. A) A diagram of the Caltech non-sewered wastewater treatment system with probes necessary for self-diagnosis indicated. Locations of duplicate probes are not specified. B) A diagram of the Duke non-sewered wastewater treatment system with probes necessary for self-diagnosis indicated. Locations of duplicate probes are not specified.

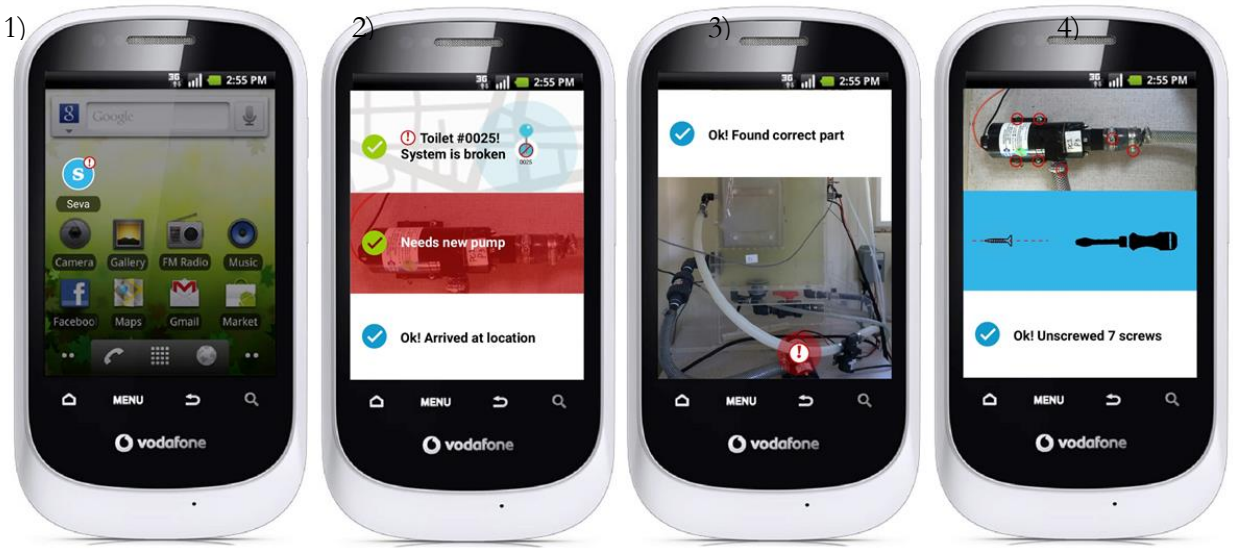

Fig. 2. Images from the operator's self-diagnosis app. From left to right. 1) When the treatment system is broken an operator with a smartphone would get a notification on their maintenance app. 2) the app will give a map of how to get to the system from the operator's current location and which part the system needs (spare parts come with the unit, they do not need to be purchased, just identified). 3) The app will show a picture of the system with the broken part indicated. 4) The app will indicate exactly what needs to be done to replace the part. If the operator does not have a smartphone, she will be given the address of the broken treatment system and once she arrives at the system, images similar to these would appear on the onboard display.

Long term design overview:

The general concept of the project is shown in Fig 3. In words, the idea is to create a "self diagnosing algorithm" for wastewater treatment technology that is useful in the developing world. In order to do this, we will have a series of sensors (outlined below and in Fig. 1) that generate data which can be uniquely matched to failure states of the system (failure modes). The data analysis (to see if the system is in a failure mode) will occur on a small computer that is located inside the treatment system. Under normal operation, at a regular frequency this computer would send an "I'm OK" message to a server which would be recorded on a webpage but will trigger no action. If an "I'm OK" message is not received regularly or if the treatment system computer detects a failure mode, the failure mode and toilet location will be sent to a server and an operator will be notified to go to the system via SMS, email and a notification on a smartphone application.

Once at the treatment system, both the onboard computer and the operator's smartphone application will display step by step pictorial instructions on how to replace the broken part (see Fig. 2).

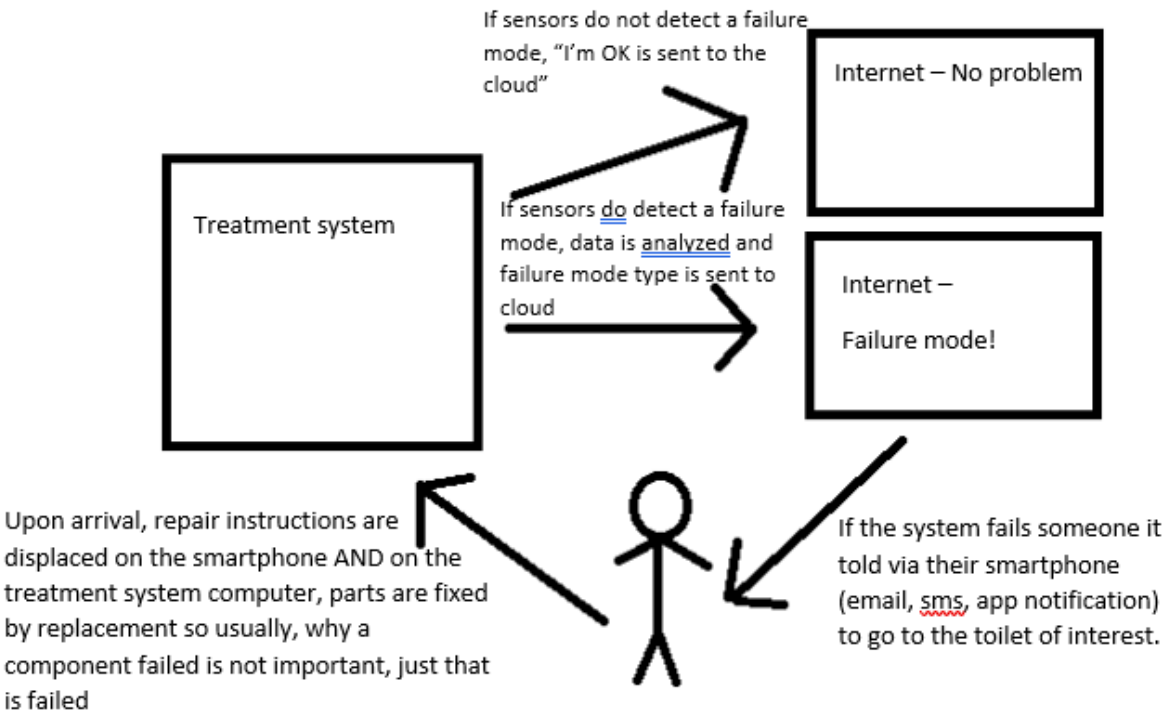

Fig. 4. An overview of how the system works.

Failure modes are occasionally dependent on multiple sensors, i.e. water level sensors in the tank should be going down when a pump is draining the tank but should not be going down if there is a leak. For our system located on campus I have listed all the failure modes:

Failure modes and corresponding sensors states of the Caltech Electrochemical Wastewater Treatment System:

Leaks:

1) Anaerobic Bioreactor Tank (ABRT) If [(ABRT water level sensor is on) and (Pipe 1 leak sensor is off) and (pump 1 ammeter is off)]
2) Electrochemical Reactor Tank (ECRT) If [(ECRT water level sensor is on) and (Pipe 3 leak sensor is off) and (Pipe 4 leak sensor is off) and (pump 2 ammeter is off)]
3) Clean Water Tank (CWT) If [(ABRT water level sensor is on) and (Pipe 4 leak sensor is off) and (Pipe 5 leak sensor is off)]
4) Toilet (TT) If [(TT water level sensor is on) and (Pipe 1 leak sensor is off)]
5) Pipe 1 If (pipe 1 leak sensor goes on)
6) Pipe 2 If (pipe 2 leak sensor goes on)
7) Pipe 3 If (pipe 3 leak sensor goes on)
8) Pipe 4 If (pipe 4 leak sensor goes on)
9) Pipe 5 If (pipe 5 leak sensor goes on)
10) Pipe 6 If (pipe 6 leak sensor goes on)

11) Electronic Failures:
12) Pump 1 If [(Voltmeter is on) and (ammeter is off)]
13) Pump 2 If [(Voltmeter is on) and (ammeter is off)]
14) Electrodes If [(Voltmeter is on) and (ammeter is off)]

Treatment Failure:

15) Electrodes If (clarity falls below threshold)
16) Filter If (turbidity falls below threshold)

Because some failure modes are depended on one another the program checks sensors with minimal lag time in between checking. Under standard operating conditions, the system reads data from sensors in a loop and prints to a file, executing one loop every minute (Fig. 4):

1) First checking the volt meters, ammeters and tank level sensors in simultaneous sets in the order of system flow.
2) Then check water level and leak sensors simultaneously in relevant pairs/triples.
3) Check turbidity
4) Check clarity
5) Check order of operations (should see current in electronics in a particular order)
6) Print data after each step to a file.

The program is customizable such that it could be suited for any number of sensors and users.

The program operates in the following way:

The class 'Sensor' creates a sensor object with details about its name, the kind of data it records, the time of data recording, and the units. Below I gave example values

Class: Sensor

Instance Variables:

 # The name of the sensor object

Name -> Water Level 1

 # The most recent data read

CurrentData -> 13.7

 # The sensor type (numeric (reports a number), threshold (reports if a threshold was exceeded), binary (records # # on/off))

Type -> double

 # What (if any) are the units associated with the data

Units -> cm

 # Time Current Data is Set

Time -> Current time

Constructor:

Sensor(name, type, units) -> Sensor(WaterLevel1, numeric, cm, 1)

SetName(name)

Type = type

Units = units

Methods of Sensor:

 # Set the sensor name

SetName(str name) -> Water Level 1etc

Sensor.Name = name

 # Look up a sensor's name

GetName() ->

Return Sensor.Name

 # Look up the sensor's type.

GetType() ->

return Sensor.Type.

 # Get the sensor's units.

GetUnits() ->

Return Sensor.Units

 # Set the current data value to be stored in the sensor

SetData(data, time) -> 1

CurrentData = data **# Data input will have different data types for different sensors**

Time = time

 # Get the current data value from the sensor file.

GetData() ->

Return CurrentData

Class: GetData

Instance Variables:

Whatever is needed from the python USB package to read the data

ListOfSensors (Sensor(name, type, units)) -> Sensor(WaterLevel1, numeric, cm, 1)

Filename

Constructor:

GetData(Sensor)

Methods:

#Read Data from USB

ReadData

Read Data using the appropriate USB package

For each sensor in ListOfSensors

Read data from each sensor in the order specified above and update Sensor.SetData(), Sensor.SetTime()

PrintFile(timestamp):

DeleteFile(Filename)

CreateFile

setFilename

For sensors in list of ListOfSensors

Print Sensors.GetName()

Print Sensors.GetType()

Print Sensors.GetData()

DeleteFile(Filename)

Delete current file.

Class: MainRunLoop

Instance Variables:

Sensors (list of all the sensors)

GetData Constructor

Methods:

Run

GetData.PrintData

The full set of code can be found in the uploaded data accompanying this thesis.

Sensor data:

Water quality parameters

Three water quality parameters were chosen] to be monitored inside the electrochemical reactor.

ORP (Oxygen Reduction Potential) is a measurement of the tendency of a chemical species to acquire electrons and thereby be reduced. Reduction potential is measured by a 2-electrode probe in millivolts (mV). The more positive the potential, the greater the species' affinity for electrons and their tendency to be reduced.

Continuous monitoring of the ORP in the reactor, will allow us to identify the chlorination break point. At this point, a complete ammonium removal will occur. A "complete ammonium removal (breakpoint chlorination) is a reasonable goal when electrochemically treating latrine wastewater. Disinfection occurs well before the breakpoint (see Fig. 5), while formation of toxic byproducts is generally minimized prior to the breakpoint.[19]

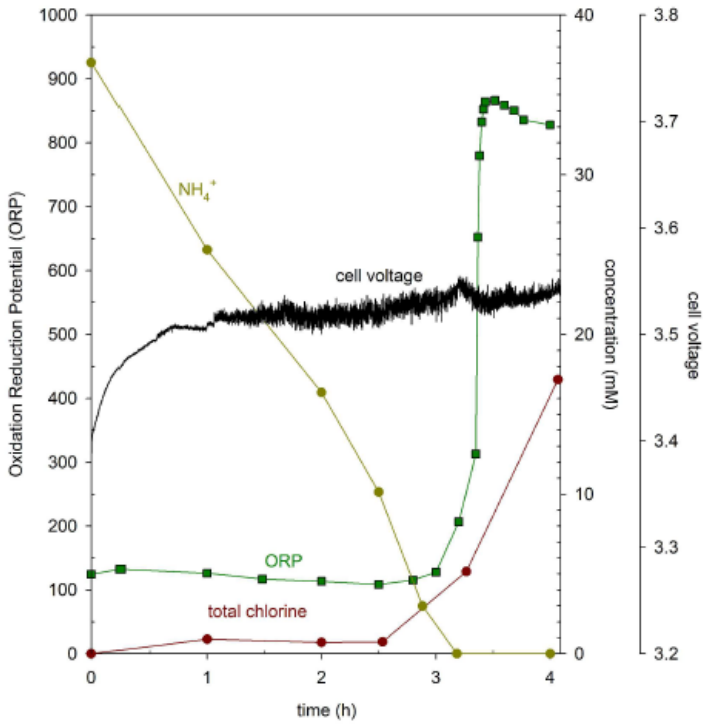

Fig. 5. ORP, total chlorine concentration, cell voltage and ammonium concentration during electrolysis of latrine wastewater amended with sodium chloride($^{TiO_2}/_{IrO_2}$anodes; 7.5 A L^{-1}; $[Cl^-]_{initial} = 100mM$. Near the breaking point (complete ammonium removal; ~3.2h) total concentration and ORP spiked. At the same point, cell voltage showed a distinct peak. Lines added for clarity[19].

Color

Color in water may result from the presence of minerals, inorganic chemicals, metal ions, decomposition of organic matter from soils, aquatic organisms and vegetation. True color, is defined as the color of water from which turbidity has been removed. Apparent color includes true color and color caused by suspended matter. Color in the yellow to brown range is determined by a visual comparison of samples with either a known colored chemical solution or calibrated color disk, in a process called platinum-cobalt method. The unit of measurement is the true color unit. Color in the treated water is removed to produce a pleasing and acceptable appearance. Furthermore, color removal during electrochemical treatment has been observed to happen after pathogen disinfection. Color may also indicate high levels of organic compounds, which may produce high levels of trihalomethanes and other disinfection by-products upon contact with chlorine or other disinfectants[42].

Turbidity

Turbidity**,** is an optical characteristic of a liquid sample, expressing the amount of light scattered by particles and solid materials in the liquid when a light beam passes through. High concentrations of particulate matter affect light penetration. Particles may also provide attachment points for other pollutants, notably metals and bacteria. For this reason, turbidity measurements can be used as an indicator of potential pollution in a water body.

Proof of Concept:

At the current stage of the project, all chosen sensors have been integrated to the lab-scale electrochemical reactor (Fig. 6) and a simple program was established to allow for continuous data readout and recording in order to perform data analysis.

In the following paragraph the current state of development for each of the individual sensors will be described:

Software:

Extensive testing on the server, client, and app with artificial sensor data indicates that the system is able to communicate and execute commands based on predefined triggers. Additionally, the software was able to send commands between server, toilet, and mobile phone in all directions. These data indicate the software portion of the concept is ready for rea data.

ORP sensor:

Due to the nature of electrochemical measurements at the ORP sensor, it is prone to disturbances arising from the electrochemical water treatment and current generated inside the ECR. Thus, to

prevent inaccurate measurements of ORP, a solution for sampling and analysis separate from the ECR is needed.

In order to integrate ORP measurements to the monitoring system while ensuring no influence of the electrochemical water treatment on the recorded data, two different solutions are currently being investigated: (i) utilization of the existing circulation pump to sample from the ECR and measure ORP in an external loop and (ii) use of an additional peristaltic pump to move samples from the ECR to an external ORP measurement loop and back. For both of these solutions, a sensor-chamber with appropriate plumbing was designed and 3D printed (see Fig. 7) to enable interference-free ORP measurement in a closed-loop circuit, parallel to the ECR. Herein, the established Caltech-Eram Solar Toilet system design was considered and the sampling system was laid out to match all requirements and space constraints.

The ORP-sensor manufacturer software was adapted to allow for integration and continuous real-time measurement of ORP data and transfer to the monitoring system platform. Preparations for a lab test of both proposed solutions have been completed – on engineering and programming sides.

Following the laboratory tests, the solution provided more consistent measurements as well as more reliable performance under prolonged operation will be selected. Therein, specific focus will be laid on the identification of the breaking point during electrochemical wastewater treatment by ORP measurements. Furthermore, no interference of the ECR with ORP measurements need to be proven and ensured. Sensor-chamber and piping layouts may be adjusted and redesigned accordingly.

Finally, sampling system and sensor code will be integrated and embedded to the final sanitation system design and the monitoring application.

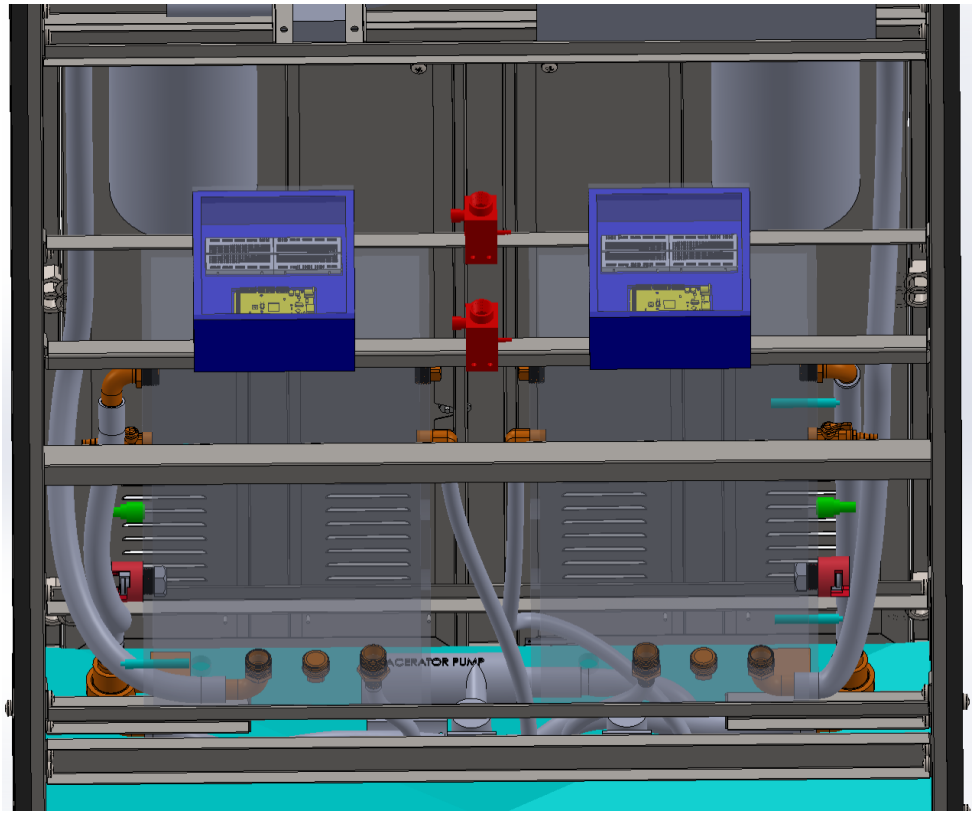
ACERATOR PUMP

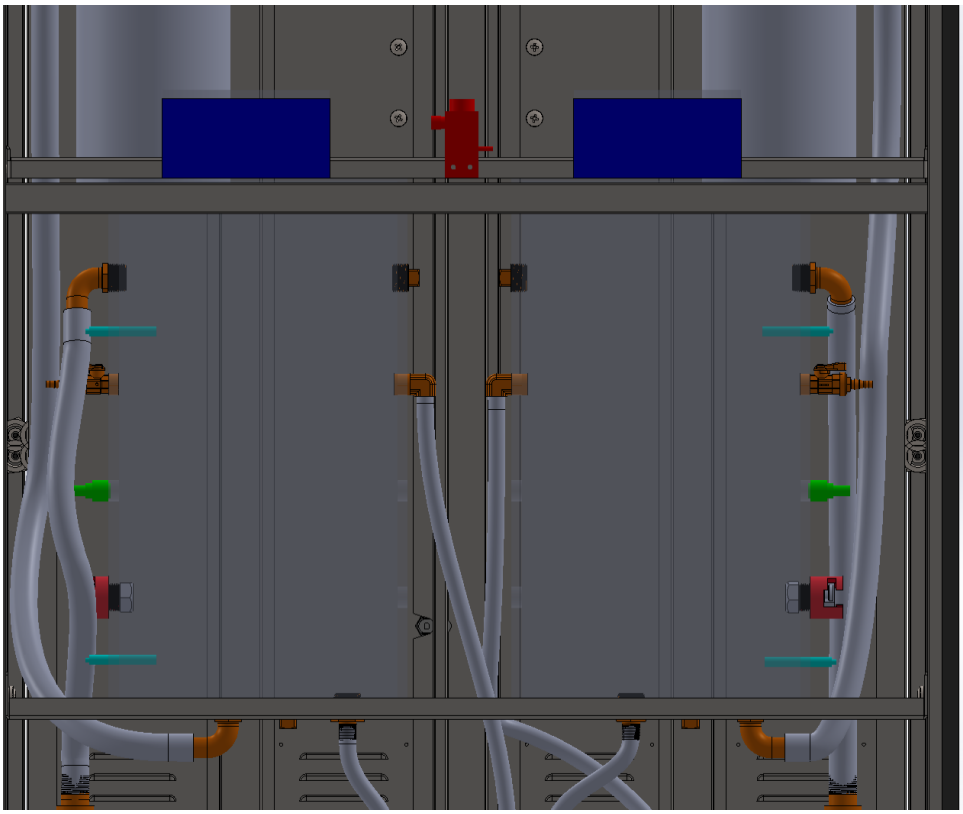

Fig. 6. 3D models (top and high view) of the sensors and Seva module (dark blue) integrated to the electrochemical reactors of the Caltech-Eram Solar Toilet. Model based on two electrochemical reactors running independently. Sensors are highlighted in different colors: switch level sensors (light blue), ORP sensor loop (red, top), turbidity sensor (red), and colorimeter (green).

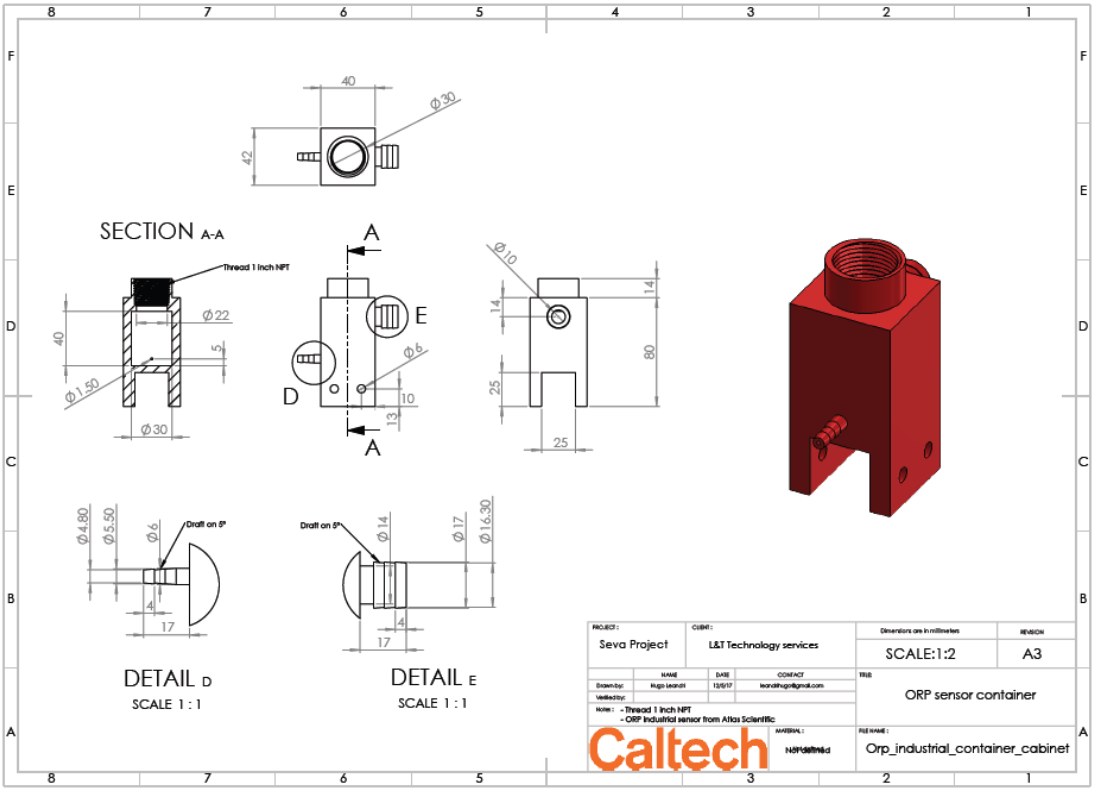

Fig. 7. Industrial ORP sensor chamber design (drawing not to scale).

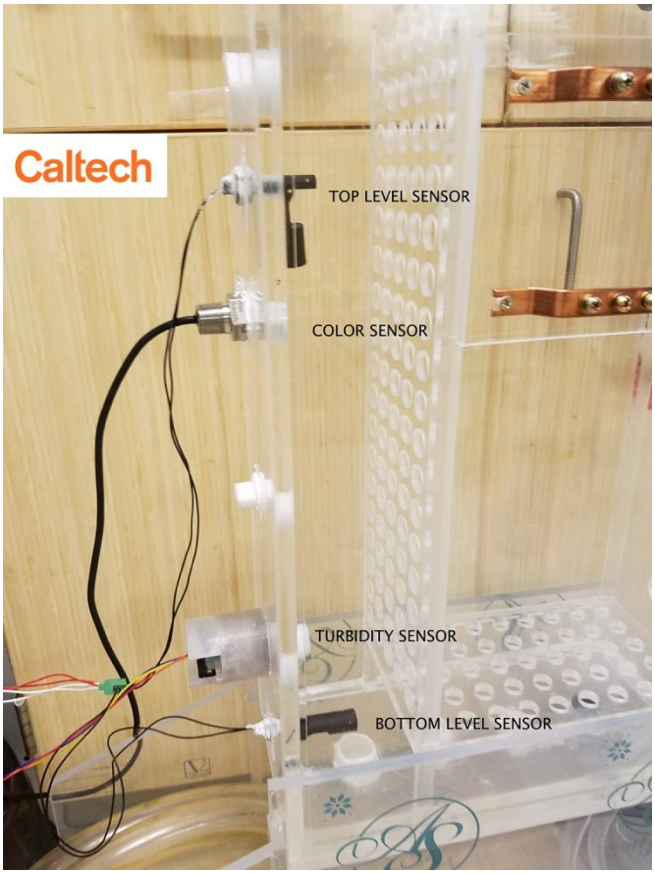

Fig. 8. Typical electrochemical reactor tank used in Caltech Solar Toilets retrofitted with level sensors, color sensor, and turbidity sensors.

Color sensor:

A colorimetric color sensing device manufactured by "Atlas Scientific" was installed to the prototype scale electrochemical reactor (Fig. 8). The sensor's dimensions and waterproof properties allowed for easy integration within the ECR.

The software included by the manufacturer was adapted to allow for integration and continuous real-time measurement of color data and export to the monitoring system platform.

Preparations for a laboratory test of the proposed sensor have been completed – on engineering and programming sides.

In the current setup, color is measured as apparent color and recorded as Tristimulus values (three values that represent the coordinates of the color on a three dimensional graph). Following the lab-scale experiments, a conversion of the data to the platinum-cobalt scale system will be evaluated. Furthermore, the impact of turbidity on color measurements will be determined and subsequently, solutions to minimize it interference may be investigated.

In a later stage, an additional low-cost sensor (TCS34725) will be examined. For this sensor, a more detailed design for integration to the ECR will need to be developed.

Finally, the chosen sensor will be integrated and embedded in the final sanitation system design and the monitoring application.

Turbidity sensor:

Generally, turbidity sensors use a light source and one or more detectors to measure light scattered by particles in water samples.

Due to the high cost of standard industrial instruments ($1000+), which usually measure turbidity using the Nephelometry method (wherein light source and photodetector are arranged at a 90-degree angle to each other), we chose to examine the performance of a low cost sensor typically used in household dishwashing and clothes washing machines. This sensor is based on the Attenuation method (light source and photodetector are at a 180-degree angle to each other).

During this part of the project, several sensor shells were designed and redesigned in order to integrate the turbidity sensor inside the ECR. The shell (see Fig. 9) was constructed to allow the placement of the

sensor inside the ECR for continuous reading, while preventing leakage and penetration of water to the sensor wiring.

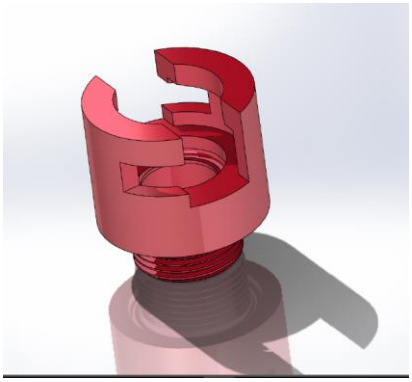

Fig. 9. Turbidity sensor shell design

In addition, several laboratory bench tests were preformed, in order to examine the performance of the sensor – in terms of detection limits and stability – and to convert the raw data to the standard unit of turbidity NTU (Nephelometric Turbidity Unit).

Herein, a standard solution of formazin was prepared and subsequently diluted. The turbidity of each dilution was measured using the low cost sensor and with a standard laboratory turbidity sensor (Hana HI 93414) for comparison. The results are presented in Fig. 10. While a good linear relationship (R^2 = 0.99) between measurements performed with the laboratory device and the low cost sensor was observed, it became apparent that the low-cost sensor is highly sensitive to the surrounding conditions and manual

handling. Thus, additional experiments under constant conditions are required to fully characterize the sensor performance.

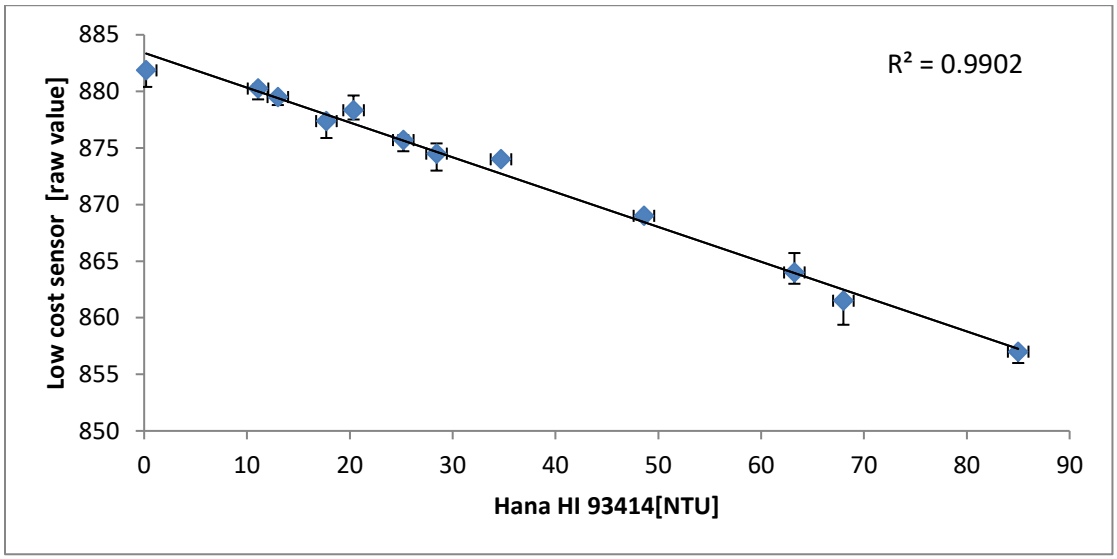

Fig. 10. LCS(Low cost sensor) raw value vs LS(lab sensor-Hana HI 93414) measurements in NTU. LCS raw values decrease as the turbidity is increasing.

At the current stage, a basic program recording the data from the sensor and export to a text file, was established and the newest design of the shell has been 3D printed and is ready to be installed in the lab-scale ECR.

Following the laboratory experiments, a detailed characterization of the sensor properties will be performed. Focusing on the data trends during the electrochemical treatment process, sensor sensitivity, accuracy and consistency in relation to tolerances in the ECR system will be determined.

In addition, readjustment of the shell and its fabrication method will be considered.

Finally, the sensor will be integrated and embedded to the final sanitation system design and the monitoring application.

Water level:

A simple approach to monitor the water level in two different points in the ECR has been chosen. Two float switch sensor have been installed in the lab-scale ECR and a simple code has been written in order to record and save the data.

In a later stage, the sensors will be embedded in the final sanitation system design and the monitoring application.

An additional solution to enable continuous monitoring of the water level will be evaluated in the future.

Other sensors:

In addition to sensors monitoring the water quality in the reactor, several other sensors will be integrated in the system to keep track of power supply and to identify any leakage in the system.

A simple code was written to operate the voltage, current and humidity sensors. These sensors still need to be integrated in the system and an efficient design to utilize the humidity sensor (or alternative sensors) for leakage detection are relatively straightforward but need to be developed.

Finally, a storage solution for the Arduino microcontroller and the Raspberry Pi needs to be designed and subsequently integrated to the Caltech-Eram prototype.

Outlook

While these data are not complete, they have demonstrated that the bulk of the sensors may provide useful data and that the program works in general to collect data. These data will focus on detailed data analysis during the laboratory experiments, evaluation of the sensor performances in the ECR, adjustment and redesign of the shells and sensors, according to the obtained results.

Based on the experimental results, in combination with literature survey, tolerances and limitations for each of the water quality parameters will be defined and integrated into the software, in order to allow a more efficient operation of the sanitation system and minimization of system down time due to malfunctions.

Subsequently, integration of the sensor network with the server and the mobile phone application will be in focus for the next steps.

The Bill and Melinda Gates Foundation has provided grant funding for the engineering firm L&T Technology Services in partnership with Eram Scientific to integrate this self-diagnosing sensor system into the a real prototype. This invention is protected under the following patent application: US20170008775A1[43].

References

1. Net-zero emissions energy systems | Science. https://science.sciencemag.org/content/360/6396/eaas9793/tab-figures-data.
2. Intergovernmental Panel on Climate Change. *Global warming of 1.5°C*. (2018).
3. Global Nitrous Oxide Production Determined by Oxygen Sensitivity of Nitrification and Denitrification - Ji - 2018 - Global Biogeochemical Cycles - Wiley Online Library. https://agupubs.onlinelibrary.wiley.com/doi/full/10.1029/2018GB005887.
4. The Kyoto Protocol and non-CO2 Greenhouse Gases and Carbon Sinks | SpringerLink. https://link.springer.com/article/10.1023/A:1020910820102.
5. Giant batteries and cheap solar power are shoving fossil fuels off the grid | Science | AAAS. https://www.sciencemag.org/news/2019/07/giant-batteries-and-cheap-solar-power-are-shoving-fossil-fuels-grid.
6. Wilson, M. Lazard's Levelized Cost of Storage Analysis—Version 4.0. 60.
7. Powering the Planet: Where in the World Will Our Energy Come From? - Nate Lewis - 5/25/2005 - YouTube. https://www.youtube.com/watch?v=EUKqx2uk-Gs.
8. British Columbia's Carbon Tax - Province of British Columbia. https://www2.gov.bc.ca/gov/content/environment/climate-change/planning-and-action/carbon-tax.
9. Waltzer, K. The Role of 45Q Carbon Capture Incentives in Reducing Carbon Dioxide Emissions. 3.
10. A Process for Capturing CO2 from the Atmosphere | Elsevier Enhanced Reader. https://reader.elsevier.com/reader/sd/pii/S2542435118302253?token=94C153D93CD1105CB152A64E509F13D1B4BA8AF8CB094A5A14CFC1FC96E505F69DA439AAE6342A3907B24539CB694923 doi:10.1016/j.joule.2018.05.006.

11. Implications for climate and sea level of revised IPCC emissions scenarios | Nature. https://www.nature.com/articles/357293a0.
12. Global water cycle agreement in the climate models assessed in the IPCC AR4 - Waliser - 2007 - Geophysical Research Letters - Wiley Online Library. https://agupubs.onlinelibrary.wiley.com/doi/full/10.1029/2007GL030675.
13. Biological Wastewater Treatment - Google Books. https://books.google.com/books?hl=en&lr=&id=41JButufnm8C&oi=fnd&pg=PA1&dq=biological+wastewater+treatment&ots=nSH1f3xB5i&sig=MqMlR69u-ju3gvnuKxy6keyNnZc#v=onepage&q=biological%20wastewater%20treatment&f=false.
14. Developments in wastewater treatment methods - ScienceDirect. https://www.sciencedirect.com/science/article/pii/S0011916404003558.
15. Breakpoint chlorination and free-chlorine contact time: Implications for drinking water N-nitrosodimethylamine concentrations - ScienceDirect. https://www.sciencedirect.com/science/article/abs/pii/S0043135406004441.
16. Contributions of electrochemical oxidation to waste-water treatment: fundamentals and review of applications - Anglada - 2009 - Journal of Chemical Technology & Biotechnology - Wiley Online Library. https://onlinelibrary.wiley.com/doi/abs/10.1002/jctb.2214.
17. Phosphate Recovery from Human Waste via the Formation of Hydroxyapatite during Electrochemical Wastewater Treatment | ACS Sustainable Chemistry & Engineering. https://pubs.acs.org/doi/abs/10.1021/acssuschemeng.7b03155.
18. Electrochemical disinfection of toilet wastewater using wastewater electrolysis cell - ScienceDirect. https://www.sciencedirect.com/science/article/pii/S0043135416300392.

19. Jasper, J. T., Yang, Y. & Hoffmann, M. R. Toxic Byproduct Formation during Electrochemical Treatment of Latrine Wastewater. *Environ. Sci. Technol.* **51**, 7111–7119 (2017).
20. Lee, D.-Y., Elgowainy, A. A. & Dai, Q. *Life Cycle Greenhouse Gas Emissions of By-product Hydrogen from Chlor-Alkali Plants*. https://www.osti.gov/biblio/1418333 (2017) doi:10.2172/1418333.
21. Shaner, M. R., Atwater, H. A., Lewis, N. S. & McFarland, E. W. A comparative technoeconomic analysis of renewable hydrogen production using solar energy. *Energy Environ. Sci.* **9**, 2354–2371 (2016).
22. Reinvent the Toilet Challenge & Expo - Bill & Melinda Gates Foundation. https://www.gatesfoundation.org/what-we-do/global-growth-and-opportunity/water-sanitation-and-hygiene/reinvent-the-toilet-challenge-and-expo.
23. Christopher, K. & Dimitrios, R. A review on exergy comparison of hydrogen production methods from renewable energy sources. *Energy Environ. Sci.* **5**, 6640–6651 (2012).
24. Wismann, S. T. *et al.* Electrified methane reforming: A compact approach to greener industrial hydrogen production. *Science* **364**, 756–759 (2019).
25. Petroleum Coke. https://www.eia.gov/dnav/pet/PET_PNP_CAPFUEL_A_(NA)_8FPP0_MBBL_A.htm.
26. H2A: Hydrogen Analysis Production Models | Hydrogen and Fuel Cells | NREL. https://www.nrel.gov/hydrogen/h2a-production-models.html.
27. How much carbon dioxide is produced per kilowatthour of U.S. electricity generation? - FAQ - U.S. Energy Information Administration (EIA). https://www.eia.gov/tools/faqs/faq.php?id=74&t=11.

28. webmaster. A Review of Water Scarcity Indices and Methodologies. *The Sustainability Consortium* https://www.sustainabilityconsortium.org/downloads/a-review-of-water-scarcity-indices-and-methodologies/.
29. Falkenmark, M. The Massive Water Scarcity Now Threatening Africa: Why Isn't It Being Addressed? *Ambio* **18**, 112–118 (1989).
30. 2015 - Water for a Sustainable World | United Nations Educational, Scientific and Cultural Organization. http://www.unesco.org/new/en/natural-sciences/environment/water/wwap/wwdr/2015-water-for-a-sustainable-world/.
31. Gerland, P. *et al.* World population stabilization unlikely this century. *Science* **346**, 234–237 (2014).
32. Lackner, K. S. CLIMATE CHANGE: A Guide to CO2 Sequestration. *Science* **300**, 1677–1678 (2003).
33. US EPA, O. Climate Impacts in the Southwest. /climate-impacts/climate-impacts-southwest.
34. The Water Crisis: Poverty and Water Scarcity in Africa. *The Water Project* https://thewaterproject.org/why-water/poverty.
35. Gleick, P. H. Basic Water Requirements for Human Activities: Meeting Basic Needs. *Water Int.* **21**, 83–92 (1996).
36. *Progress on drinking water and sanitation: 2014 update*. (World Health Organization, 2014).
37. Berge, N. D. *et al.* Hydrothermal Carbonization of Municipal Waste Streams. *Environ. Sci. Technol.* **45**, 5696–5703 (2011).
38. Abdeen, S., Di, W., Hui, L., Chen, G.-H. & van Loosdrecht, M. C. M. Fecal coliform removal in a sulfate reduction, autotrophic denitrification and nitrification integrated (SANI) process for saline sewage treatment. *Water Sci. Technol.* **62**, 2564–2570 (2010).

39. Solutions when the Solution is the Problem: Arraying the Disarray in Development - Working Paper 10. *Center For Global Development* https://www.cgdev.org/publication/solutions-when-solution-problem-arraying-disarray-development-working-paper-10.
40. Mobile cellular subscriptions (per 100 people) | Data. https://data.worldbank.org/indicator/IT.CEL.SETS.P2.
41. NW, 1615 L. St, Suite 800Washington & Inquiries, D. 20036USA202-419-4300 | M.-857-8562 | F.-419-4372 | M. Smartphone Ownership Is Growing Rapidly Around the World, but Not Always Equally. *Pew Research Center's Global Attitudes Project* https://www.pewresearch.org/global/2019/02/05/smartphone-ownership-is-growing-rapidly-around-the-world-but-not-always-equally/ (2019).
42. Water Quality and Treatment: A Handbook on Drinking Water, Sixth Edition. *AWWA-American Water Works Association* https://www.awwa.org/Store/{ProductName}/ProductDetail/{ProductId}?productId=6292.
43. Finke, C. E. *et al.* Maintenance self-diagnosis and guide for a self-contained wastewater treatment system. (2017).
44. Ogden, J. M. Prospects for building a hydrogen energy infrastructure. *Annu. Rev. Energy Environ.* **24**, 227–279 (1999).
45. Ave, H. Support for Cost Analyses on. 76 (2011).
46. Techno-Economic Analysis of Methane Pyrolysis in Molten Metals: Decarbonizing Natural Gas - Parkinson - 2017 - Chemical Engineering & Technology - Wiley Online Library. https://onlinelibrary.wiley.com/doi/abs/10.1002/ceat.201600414.
47. Catalytic molten metals for the direct conversion of methane to hydrogen and separable carbon | Science. https://science.sciencemag.org/content/358/6365/917/tab-figures-data.

48. A World of Sulfur. *World Fertilizer* https://www.worldfertilizer.com/special-reports/24122018/a-world-of-sulfur/ (2018).
49. Nieuwenhuyse, A. E. van. *Best Available Techniques for Pollution Prevention and Control in the Eiropean Fertilizer Industry*. vol. 8 (2000).
50. Kumareswaran Subasgar *et al.* Design of a Plant to Manufacture Sulfuric Acid from Sulfur. (2013) doi:10.13140/RG.2.1.1083.2724.
51. Weidner, J. W. Electrolyzer performance for producing hydrogen via a solar-driven hybrid-sulfur process. *J. Appl. Electrochem.* **46**, 829–839 (2016).
52. Nieuwenhuyse, A. E. van. *Best Available Techniques for Pollution Prevention and Control in the European Sulphuric Acid and Fertilizer Industries*. (European FertilizerManufacturers' Association, 2000).
53. Lulu, X., Ping, Z., Songzhe, C. & Laijun, W. Quantitative analysis of the cell voltage of SO2-depolarized electrolysis in hybrid sulfur process. *Nucl. Eng. Des.* **306**, 203–207 (2016).
54. Sulfuric Acid Corrosion | H2SO4 Corrosion | Sulphuric Acids. https://tubingchina.com/Sulfuric-Acid-H2SO4-Corrosion.htm.
55. Gorensek, M. B., Staser, J. A., Stanford, T. G. & Weidner, J. W. A thermodynamic analysis of the SO2/H2SO4 system in SO2-depolarized electrolysis. *Int. J. Hydrog. Energy* **34**, 6089–6095 (2009).
56. Economics and Chemical Engineering. in *Chemical Engineering for Non-Chemical Engineers* 79–87 (John Wiley & Sons, Ltd, 2017). doi:10.1002/9781119369196.ch6.
57. Li, F. *Situation and Practical Data of Sulfuric Acid Vacuum Concentration Unit of NCIC*.
58. EIA - Electricity Data. https://www.eia.gov/electricity/monthly/epm_table_grapher.php?t=epmt_5_6_a.

59. Shaner, M. R., Davis, S. J., Lewis, N. S. & Caldeira, K. Geophysical constraints on the reliability of solar and wind power in the United States. *Energy Environ. Sci.* **11**, 914–925 (2018).

60. Ardani, K. *et al. Installed Cost Benchmarks and Deployment Barriers for Residential Solar Photovoltaics with Energy Storage: Q1 2016*. http://www.osti.gov/servlets/purl/1338670/ (2016) doi:10.2172/1338670.

61. Jechura, J. Hydrogen from Natural Gas via Steam Methane Reforming (SMR). 21.

62. Green Markets. *Green Markets* https://fertilizerpricing.com/pricing-news/green-markets/.

63. Garrett, D. E. *Chemical Engineering Economics*. (Van Nostrand Reinhold, 1989).

64. Pierre Millet *et al.* Implementation of cobalt clathrochelates in polymer electrolyte water electrolysers for hydrogen evolution. *Chem. Eng. Trans.* **41**, 325–330 (2014).

65. O'Brien, T. F., Bommaraju, T. V. & Hine, F. *Handbook of Chlor-Alkali Technology: Volume I: Fundamentals, Volume II: Brine Treatment and Cell Operation, Volume III: Facility Design and Product Handling, Volume IV: Operations, Volume V: Corrosion, Environmental Issues, and Future Developments*. (Springer US, 2005).

66. SUMNER, J., BIRD, L. & DOBOS, H. Carbon taxes: a review of experience and policy design considerations. *Clim. Policy* **11**, 922–943 (2011).

67. Corgnale, C. & Summers, W. A. Solar hydrogen production by the Hybrid Sulfur process. *Int. J. Hydrog. Energy* **36**, 11604–11619 (2011).

68. Jayakumar, J. V. *et al.* Polybenzimidazole Membranes for Hydrogen and Sulfuric Acid Production in the Hybrid Sulfur Electrolyzer. *ECS Electrochem. Lett.* **1**, F44–F48 (2012).

69. Opperman, H., Kerres, J. & Krieg, H. SO2 crossover flux of Nafion® and sFS-PBI membranes using a chronocoulometric (CC) monitoring technique. *J. Membr. Sci.* **415–416**, 842–849 (2012).

70. Khan, H. A. *et al.* Pt encapsulated hollow mesoporous SiO2 sphere catalyst for sulfuric acid decomposition reaction in SI cycle. *Int. J. Hydrog. Energy* **44**, 2312–2322 (2019).

71. Kodera, F., Kuwahara, Y., Nakazawa, A. & Umeda, M. Electrochemical corrosion of platinum electrode in concentrated sulfuric acid. *J. Power Sources* **172**, 698–703 (2007).

72. Davie, M. G., Cheng, H., Hopkins, G. D., LeBron, C. A. & Reinhard, M. Implementing Heterogeneous Catalytic Dechlorination Technology for Remediating TCE-Contaminated Groundwater. *Environ. Sci. Technol.* **42**, 8908–8915 (2008).

73. Author, N. G. *Water and Wastewater Annual Price Escalation Rates for Selected Cities across the United States*. http://www.osti.gov/servlets/purl/1413878/ (2017) doi:10.2172/1413878.

74. Lalvani, S. B. & Dave, B. Simultaneous production of hydrogen and sulfuric acid from aqueous sulfur slurry. *Int. J. Hydrog. Energy* **11**, 639–646 (1986).

75. Ellis, L. D., Badel, A. F., Chiang, M. L., Park, R. J.-Y. & Chiang, Y.-M. Toward electrochemical synthesis of cement—An electrolyzer-based process for decarbonating $CaCO_3$ while producing useful gas streams. *Proc. Natl. Acad. Sci.* 201821673 (2019) doi:10.1073/pnas.1821673116.

Chapter 3

Enhancing the activity of oxygen-evolution and chlorine-evolution electrocatalysts by atomic layer deposition of TiO_2

Cody E. Finke[a,b,c]*, Stefan T. Omelchenko[c], Justin T. Jasper[a,b,c], Michael F. Lichterman[a], Carlos G. Read[b,d], Nathan S. Lewis[d], Michael R. Hoffmann[a,b,c]*

Affiliations:

[a]The Linde Center for Global Environmental Science, Caltech

[b]The Resnick Sustainability Institute, Caltech

[c]Division of Engineering and Applied Science, Caltech

[d]Division of Chemistry and Chemical Engineering, Caltech

*Corresponding Authors: finkec@caltech.edu, mrh@caltech.edu

Abstract

We report that TiO_2 coatings formed *via* atomic layer deposition (ALD) may tune the activity of IrO_2, RuO_2, and FTO for the oxygen-evolution and chlorine-evolution reactions (OER and CER). Electrocatalysts exposed to ~3-30 ALD cycles of TiO_2 exhibited overpotentials at 10 mA/cm^2 of geometric current density that were several hundred mVs lower than uncoated catalysts, with correspondingly higher specific activities. For example, the deposition of TiO_2 onto IrO_2 yielded an 8.7-fold increase in the OER-specific activity in 1.0 M H_2SO_4 (0.1 to 0.87 mA/cm$^2_{ECSA}$ at 350 mV overpotential). The oxidation state of titanium and the potential of zero charge were also a function of the number of ALD cycles, indicating a correlation between oxidation state, potential of zero charge, and activity of the tuned electrocatalysts.

Broader context:

Realizing a low anthropogenic CO_2 emissions future depends on the electrochemical production of fuels and commodity chemicals. In the absence of a substantial carbon tax, electrochemical production of these materials must be cost competitive with conventional production. The levelized cost of electrochemically produced chemicals depends heavily on operational expenses (OpEx; e.g., buying electricity) and the balance of systems costs, and depend relatively less on the price of the catalyst[1]. Therefore, one pathway to low cost electrochemical fuel and commodity chemical production is to reduce the OpEx by fabricating highly active catalysts. Current methods to enhance catalytic activity are limited or rely on computationally-expensive calculations. Simple tools that can be used to enhance the catalytic activity for a variety of chemical reactions, such as tuning catalysts

through atomic layer deposition as presented here, are essential to developing low-cost electrochemical systems that can meet global energy and chemical demands.

Introduction:

Highly active electrocatalysts are required for the cost-effective generation of fuels and commodity chemicals from renewable sources of electricity [2, 3]. Despite potential advantages (e.g., facile product separation), the industrial use of many heterogeneous electrocatalysts is currently limited in part by suboptimal catalytic activity and/or selectivity. In addition, there are limited methods to tune the selectivity and activity of heterogeneous electrocatalysts [2]. Methods and design tools such as doping, inducing strain, and mixing metal oxides have been used to improve the catalytic activity of heterogeneous electrocatalysts [4-7]. The activity of heterogeneous electrocatalysts can also be tuned by applying thin layers of another material, leading to an altered surface charge density on the resulting composite material relative to the bulk charge density of either individual material [8-13]. This approach has been widely used to alter the catalytic and electronic properties of core/shell nanoparticles, although additional tuning of the particle support structure is necessary to create an efficient heterogeneous electrocatalyst [14, 15]. Density functional theory calculations have shown that a single atomic layer of TiO_2 on RuO_2 should lead to enhanced selectivity for the chlorine-evolution reaction (CER) relative to the oxygen-evolution reaction (OER) [9]. Enhanced catalytic activity for the OER has been reported for WO_3 photocatalysts coated with 5 nm of alumina, with the activity increase ascribed to an alteration in the electronic surface-state density [16]. Enhanced catalytic activity has also been observed at the interface between TiO_2 and RuO_2, with charge transfer between RuO_2 and TiO_2 resulting in a mixed phase with an intermediate charge density [5].

Herein, atomic layer deposition (ALD; a stepwise deposition technique) has been used to tune the surface charge density, and consequently tune the catalytic activity, of electrocatalytic systems in a fashion consistent with estimates based on group electronegativity concepts (see Figs. S1-S5 in the Supplementary Materials for further discussion of ALD, surface homogeneity, and group electronegativity estimates). To test these predictions, the activities of the known electrocatalysts, IrO_2, RuO_2, and F-doped SnO_2 (FTO) were tuned and evaluated for the chlorine-evolution reaction (CER) and the oxygen-evolution reaction (OER). The CER provides a promising approach to infrastructure-free wastewater treatment as well as for the production of chlorine, an important

industrial chemical whose global annual demand exceeds seventy million metric tons [17, 18]. The OER is the limiting half-reaction for water splitting that could provide hydrogen for transportation and could also provide a precursor to energy storage via thermochemical reaction with CO_2 to produce an energy-dense, carbon-neutral fuel [19].

Results and discussion:

Each material tested was selected based on its theoretical group electronegativity (χ) relative to the group electronegativity of RuO_2 ($\chi \approx 2.72$), the most active catalyst for the OER in the benchmarking literature (Fig. S5) as well as the most active catalyst for the CER [20]. IrO_2 ($\chi \approx 2.78$) and FTO ($\chi \approx 2.88$) were also investigated because they have higher electronegativities than RuO_2, and therefore using ALD to overcoat these catalysts with TiO_2 ($\chi \approx 2.62$) is expected to shift their surface electronic properties (i.e., the potential of zero charge, E_{ZC}) and catalytic activities towards that of RuO_2, the optimal single metal oxide catalyst. These materials were also chosen because TiO_2, IrO_2, RuO_2, and other materials are commonly used to form mixed metal oxide electrodes, most notably the dimensionally stable anode (DSA), in which TiO_2 increases the anode's stability, but does not confer enhanced activity to the aggregated material [21].

Overpotentials (η; the excess potential beyond the equilibrium potential required to reach a given current density) were determined for IrO_2, RuO_2, and FTO as a function of the successive number of TiO_2 ALD cycles (see Supplementary Materials for additional details on electrode preparation and testing, and TiO_2 growth rate) for the OER at 10 mA/cm^2_{geo} in 1.0 M H_2SO_4 and for the CER at 1 mA/cm^2_{geo} in 5.0 M NaCl adjusted to pH 2.0 with HCl. Current densities were chosen to produce >95% measured Faradaic efficiency for each catalyst (Table S2), and current-potential data were corrected for the solution resistance (< 2.0 mV correction) as measured by electrochemical impedance spectroscopy (see Supplementary Materials for details). The three catalysts were prepared on substrates that had very low roughness to minimize effects in geometric overpotential measurements due to surface area differences. Specifically, electrocatalyst samples consisted of a ~300 nm metal-oxide film sputter deposited on a (100)-oriented Si substrate, in the case of IrO_2 and RuO_2, or commercially available TEC 15 FTO glass substrates, in the case of FTO-based electrocatalysts. TiO_2 overlayers were then deposited on top of the electrocatalysts. The

microstructure of a typical IrO_2-based electrocatalyst is shown in the cross-sectional scanning electron microscopy (SEM) image in Figure 1A. The resulting electrocatalysts were very smooth with low surface roughness (Fig. 1B) such that the surface area as measured by atomic-force microscopy (AFM) was roughly equivalent to the measured geometric surface areas (Table S1). Further characterization of the electrocatalysts' surface topology can be found in Fig S1-S4 and Table S1.

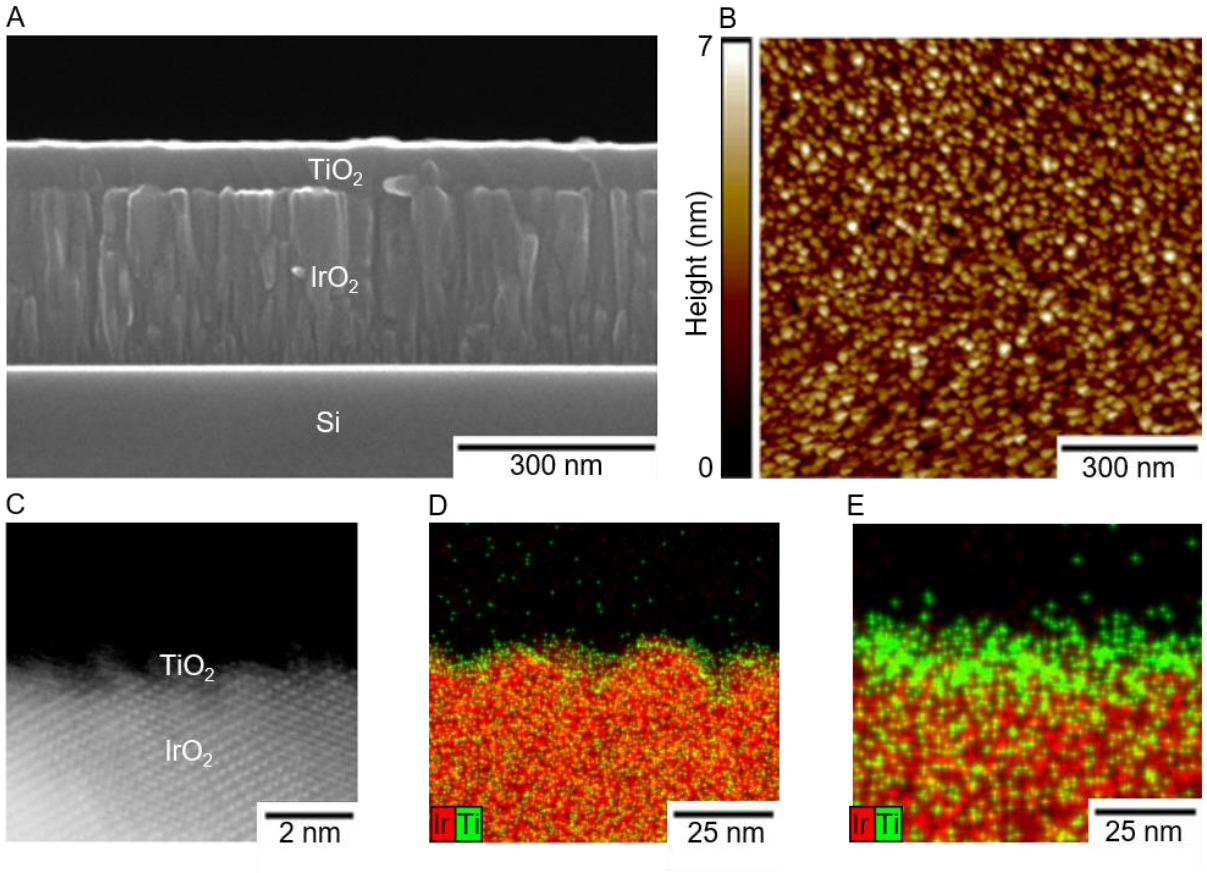

Fig. 1. Material characterization of typical electrocatalyst samples. (A) SEM image of an IrO_2 catalyst with 1000 ALD TiO_2 cycles. (B) AFM map of IrO_2 with 10 ALD cycles of TiO_2. (C) HAADF-STEM image of an IrO_2-based electrocatalyst with 10 ALD cycles of TiO_2. The underlying crystalline material is IrO_2 (labeled) while the hair-like, amorphous material at the surface is TiO_2 (labeled). (D,E) Energy dispersive X-ray spectroscopy (EDS) maps of IrO_2-based electrocatalysts with 10 and 40 ALD cycles of TiO_2, respectively. The red color indicates Ir and green indicates Ti. Note that green and red intermix throughout this cross section due to the inherent roughness of the sample.

The measured OER overpotentials at 10mA/cm$^2_{geo}$ for bare RuO_2 and IrO_2 agreed well with values reported for catalysts prepared on similarly flat surfaces, however we are unaware of comparable OER data for FTO or for CER catalysts [22]. The overpotentials for IrO_2 and FTO, for both the OER and CER, initially showed an improvement (i.e., reduction) with increasing ALD cycle number, before exhibiting a deterioration due to an increase in overpotential at higher ALD cycle numbers (Fig. 2). The triangular shape observed between the overpotential and the TiO_2 ALD cycle number is typical of a volcano-type relationship that exemplifies the Sabatier principle [23]. The overpotential reductions between bare IrO_2 and FTO catalysts and those at the peak of the volcano curve for the OER were $\Delta\eta_{OER} \approx$ -200 mV at 10 cycles and -100 mV at 30 cycles, respectively. For the CER, the observed overpotential reductions were $\Delta\eta_{CER} \approx$ -30 mV at 3 cycles and -100 mV at 10 cycles, for IrO_2 and FTO respectively (Fig. 2). A volcano-type relationship between cycle number and overpotential was also observed for RuO_2 facilitating the OER, with $\Delta\eta_{OER} \approx$ -350 mV between 0 and 10 cycles, Fig. 2. However, for the CER, the overpotential of the RuO_2-based catalyst increased with TiO_2 ALD cycle number (Fig. 2).

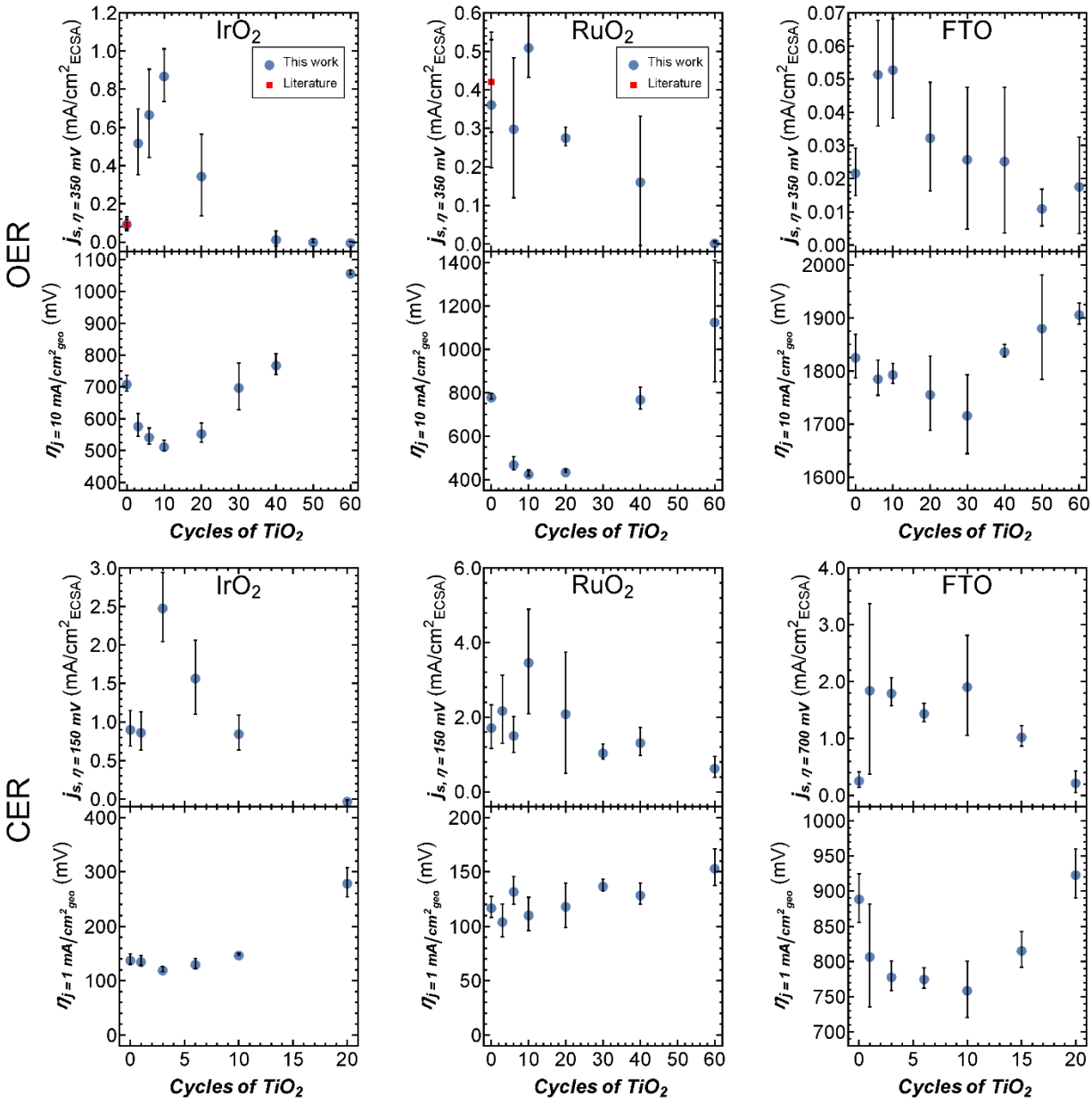

Fig. 2. Specific activities (j_s) and overpotentials (η) for the OER and CER on IrO_2, RuO_2, and FTO coated at various ALD cycles of TiO_2. Overpotentials were measured at 10 mA/cm^2_{geo} for the OER and at 1 mA/cm^2_{geo} for the CER (normalized to geometric surface area). Specific activities for the OER were measured at 350 mV (IrO_2 and RuO_2) or 900 mV (FTO). Specific activities for the CER were measured at 150 mV (IrO_2 and RuO_2) or 700 mV (FTO). The red squares indicate available literature values.

The specific activity (i.e., the current density normalized to the electrochemically active surface area (ECSA)) is a standard quantity for comparing the OER activity of heterogeneous electrocatalysts (see Figs. S9-S11, and the Supplementary Materials for details on specific activity calculations and additional discussion). While ECSA is limited by the assumption that Pt has 100% active surface area, it is generally believed to be more accurate than other surface area methods like geometric (which assumes rough surfaces are flat), BET (which assumes inert gases have the same ability to penetrate a catalyst as electrolytes), and atomic-force-microscopy-measured-surface-area (which is limited by the resolution of the AFM tip). For IrO_2 and RuO_2 catalysts, the OER specific activities of the uncoated catalysts were in good agreement with previously reported values [20]. We are unaware of reported specific activities for FTO for the OER or for any catalyst for the CER. The specific activities for the OER and CER were characterized by volcano-type relationships as a function of the TiO_2 ALD cycle number (Fig. 2). In fact, IrO_2 coated with 10 ALD cycles of TiO_2 showed an 8.7-fold increase in OER specific activity at $\eta = 350$ mV relative to uncoated IrO_2, resulting in the highest ECSA-based specific activity reported to date for Ir-based OER catalysts at $\eta = 350$ mV in 1.0 M H_2SO_4. Recently, $IrO_x/SrIrO_3$ has been reported as an especially active catalyst using current normalized to atomic force microscopy measured surface area (AFMSA) in 0.5 M H_2SO_4. To compare these catalysts, we measured the roughness of our catalysts using AFM (Table S1). For our catalysts, bare IrO_2 exhibited a Tafel slope of ~60 mV/dec in good agreement with previously reported OER catalysts [24]. As the activity of our IrO_2 based catalyst increased from bare IrO_2 to 10 TiO_2 ALD cycles, the Tafel slope remained constant at ~60 mV/dec while the exchange current density (i_0) increased from ~1×10^{-7} to ~2×10^{-5} mA/cm^2_{AFMSA}. Initially the $IrO_x/SrIrO_3$ catalyst also had an OER Tafel slope of ~60 mV/dec and an i_0 of ~7×10^{-6} mA/cm^2_{AFMSA}. For the $IrO_x/SrIrO_3$, however, after a period of activation the Tafel slope improved dramatically to ~40 mV/dec, which indicates a previously unknown OER mechanism, while the i_0 deteriorated to ~3×10^{-7} mA_{AFMSA} (see Fig. S12, Table S4, and Supplementary Materials for details on Tafel analysis). In our case, IrO_2 coated with 10 ALD cycles of TiO_2 exhibited lower overpotentials than the freshly prepared $IrO_x/SrIrO_3$ catalyst at current densities < 1 mA/cm^2_{AFMSA} and lower overpotentials than the activated $IrO_x/SrIrO_3$ catalyst at < 0.02 mA/cm^2_{AFMSA}, but substantially higher overpotentials at the more industrially relevant current densities of > 10 mA/cm^2_{AFMSA} [2, 25]. Further discussion on surface roughness, including AFM, and SEM sample characterization is presented in the Supplementary Materials (Figs. S1-S4 and Table S1).

To test the longevity of the enhanced catalytic performance with TiO_2 deposition, we performed 24 h stability tests at 10 mA/cm^2 for both the CER and the OER for the uncoated catalyst and the most active catalyst for each material system. The catalysts investigated herein were not optimized for stability and, as was previously reported for thin IrO_2 and RuO_2 catalyst depositions [20, 26], the overpotential on uncoated catalysts for the OER in 1 M H_2SO_4 degraded rapidly after < 1 h of operation at 10 mA/cm$^2_{geo}$. For thinly coated catalysts (3-10 cycles) the OER stability improved from about 1 h to about 4 h, while for thicker TiO_2 coatings (> 30 cycles) the OER stability increased to > 9 h (Fig. S7). The loss in activity for the OER for TiO_2 coated samples was associated with a loss in the TiO_2 coating as illustrated in X-ray photoelectron spectroscopy (XPS) measurements of the Ti 2p core level before and after electrochemical stability testing (Fig. S23). For the CER, all catalysts were relatively stable over the 24 h testing period except for the FTO-based catalysts which followed the same trend as the OER, with thicker TiO_2 coatings stabilizing the electrodes. XPS measurements of the stable CER catalysts indicated that the TiO_2 overcoating was still present even after 24 h of continuous operation (Fig. S24).

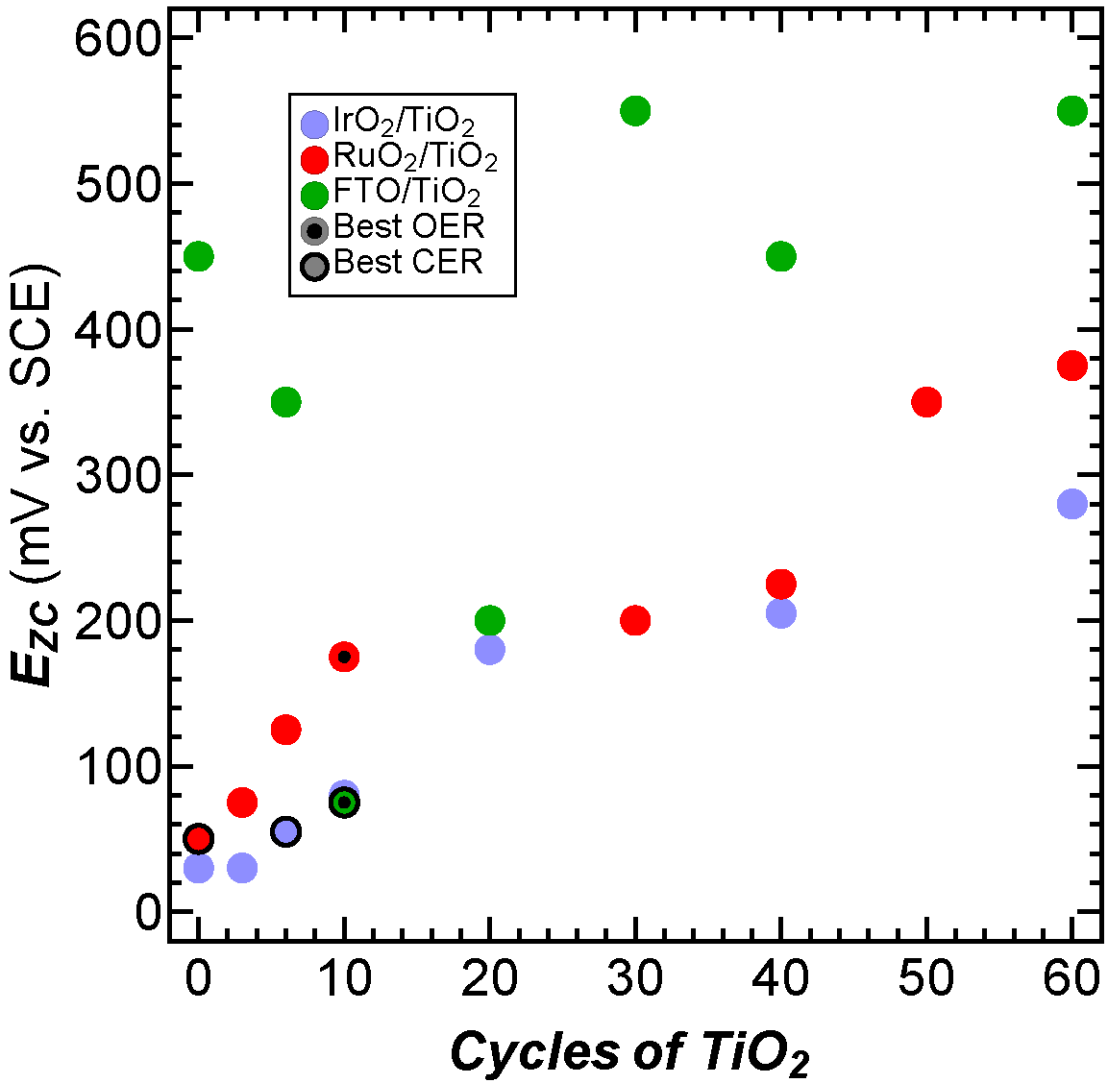

Fig. 3. E_{ZC} of IrO_2 (blue), RuO_2 (red), and FTO (green) anodes coated with various ALD cycles of TiO_2. Black dots and circles with black borders indicate the catalysts with the highest specific activity for each catalyst for the OER and CER, respectively. For FTO base samples there appears to be a cusp at 10 cycles, while for IrO_2 and RuO_2 based samples there does not appear to be a cusp. While this phenomenon is not fully understood, XPS data may provide some clues. In general, the oxidation state of the TiO_2 and the Ezc appear to be well correlated and infact, shows the same cusp for FTO (figure S20). These data would be consistent with the idea that a thin layer of TiO2 alters the chemical structure of the surface which may draw more electrons from fluoride or oxygen however thick layers do not behave that way. There is significant evidence for thin films behaving differently than bulk materials due to strain and strange molecular orbital hybridization, but a detailed computational study may be necessary.

The enhancement in catalytic performance observed with deposition of TiO_2 is not readily explained by surface morphological changes of the electrocatalyst. Deposition of TiO_2 does not substantially affect the electrochemically active surface area, a metric believed to be related to active site density, and changes in the surface area alone do not account for the magnitude of the enhancement in the specific activity (Fig. S11). Furthermore, while high-angle annular dark-field scanning transmission electron microscopy (HAADF-STEM) images and STEM electron dispersive X-ray spectroscopy (EDS) maps of IrO_2 samples with 10 cycles of TiO_2 (Figs. 1C, D) indicate that the TiO_2 film is semi-continuous with small areas of the underlying IrO_2 exposed, deposition of 40 cycles of TiO_2 results in a uniform, continuous film (Fig. 1E) and catalysis commensurate with the bare IrO_2 samples, while even lower activities are observed with more TiO_2 layers (fig. 1). These facts suggest the phenomenon does not arise from surface morphological effects alone, instead suggesting that TiO_2 is playing a partial role in enhancing the activity of the active sites

To investigate the electrocatalysts' surface electronic properties the potential of zero charge (E_{ZC}) of the electrocatalysts was measured as a function of TiO_2 thickness (Fig. 3). E_{ZC} is the potential that must be applied to produce a neutral surface and is an indicator of a material's willingness to lose electrons, with more positive E_{ZC} values indicating surfaces that are less willing to lose their electrons (see Supplementary Materials, eqs. S2 and S3, and Figs. S13 - S16 for details and discussion on handling thin TiO_2 layers in E_{ZC} measurements). E_{ZC} thus yields insight into the strength of the bonds on the catalyst surface [27, 28]. Measured E_{ZC} values for bare RuO_2 and IrO_2 (50 and 30 mV vs. SCE, respectively) were consistent with previously reported values for Ru and Ir [29]. We are unaware of reported E_{ZC} values for FTO. As the RuO_2 and IrO_2 samples were coated with increasing ALD cycles of TiO_2 the E_{ZC} shifted from lower to higher potentials in both cases and eventually reached the value for bulk TiO_2. This behavior is consistent with the expected trends for equilibrated group electronegativities. The E_{ZC} for bare FTO (450 mV vs SCE) was less than that for bulk TiO_2 and greater than bare IrO_2 or RuO_2. The FTO E_{ZC} decreased with increasing TiO_2 cycles up to 10 cycles and as the TiO_2 cycles increased beyond 10 the E_{ZC} increased until it reached the bulk value of TiO_2 at large cycle numbers. The overall trend of the FTO E_{ZC} increasing to higher values with increasing TiO_2 cycle number is consistent with group electronegativity arguments. However, the intermediate behavior where the E_{ZC} decreases and then increases is not well explained by group electronegativity and could, in part, arise from the complicated behavior of the F dopant atoms (further discussion on

the limits of group electronegativity are found in the Supplementary Materials). For all catalysts, the E_{ZC} continued to shift even beyond the point where TEM data indicated that the film is continuous (40 ALD cycles). This suggests that the exposed metal oxide is not fully responsible for the shift in E_{ZC} and that the surface TiO_2 is likely responsible in part for the *Ezc* shift. Shifts in E_{ZC} with incremental TiO_2 deposition suggest that ALD can be used to tune the catalytic performance. These data reveal that the catalysts with the highest activity for the CER have E_{ZC} values between 50 and 75 mV vs SCE (Fig. 3), consistent with the observation that addition of TiO_2 layers to RuO_2 decreased the activity of RuO_2 electrocatalysts (E_{ZC} = 50 mV vs SCE) for the CER. Additionally, active OER and CER catalysts for all systems investigated have E_{ZC} values between 25 and 200 mV vs SCE with the best OER catalysts having a somewhat higher E_{ZC} (~110 mV vs SCE) than the best CER catalysts (~60 mV vs SCE).

To further understand the surface states of the catalysts, X-ray photoelectron spectroscopy was used to measure the Ti oxidation state. Fig. 4 shows the Ti $2p_{3/2}$ core-level photoemission (for the full Ti 2p region see Fig. S17), stacked from bottom to top, for increasing ALD TiO_2 thickness, with 0 cycles indicating the bare catalyst substrate. Deposition of low cycle numbers of ALD TiO_2 on IrO_2 and RuO_2 produced Ti core-level peaks that were at ~456.6 eV and ~457.6 eV, which is consistent with previously reported binding energies for Ti^{3+} states [30, 31]. As the ALD cycle number increased, the Ti oxidation state for these samples gradually increased to its bulk oxidation state (~+4), and signals indicative of bulk TiO_2 were eventually observed (Fig. 4). In the case of ALD TiO_2 on FTO, the lower cycle number thicknesses instead produced binding energies primarily at the bulk position, in addition to a peak at a higher binding energy. This additional peak can be ascribed to a mixed phase between the substrate (FTO) and the thin TiO_2 film, in which the chemical nature of the phase produces a more oxidized metal, with the mixed phase most likely dominated by Ti^{4+} sites.

The variation in the Ti oxidation state with ALD TiO_2 cycles is accompanied by a peak shift of the $Ti2p_{3/2}$ peak relative to the bulk TiO_2 peak position (Fig. S20). The $Ti2p_{3/2}$ peak of the IrO_2- and RuO_2-based catalysts shifts from reduced, lower binding energies to the more oxidized, higher binding energies typical of bulk TiO_2. The FTO-based $Ti2p_{3/2}$ peak shifts from more oxidized, high binding energies at low TiO_2 cycles to lower binding energies for intermediate TiO_2 cycles (10-40 cycles) before increasing again to higher binding energies at large TiO_2 thicknesses (>60 cycles).

The $Ti2p_{3/2}$ peak shift is qualitatively consistent with the variation in E_{zc} with TiO_2 cycle number suggesting that the change in the surface charge density is correlated with a change in the Ti oxidation state.

The variation in the Ti oxidation state with TiO_2 thickness can be explained by charge transfer from the underlying metal oxide substrate. In this scenario, a more reduced Ti species present at low deposited cycles of TiO_2 on IrO_2 and RuO_2 would be accompanied by a more oxidized metal oxide substrate. In order to confirm this hypothesis, we measured the Ir 4f, Ru 3d, and Sn 3d core-level photoemission (Fig. S21). Unlike in the case of the Ti 2p spectra, the Ir 4f, Ru 3d, and Sn 3d core-level photoemission exhibited very small changes between the bare metal oxide substrate and those with varying thicknesses of TiO_2. This was reflected in the peak shifts of the main peak for the Ir 4f, Ru 3d, and Sn 3d spectra with TiO_2 thickness relative to that of the bare substrate (Fig. S22), which were an order of magnitude lower than those for the Ti 2p core-level photoemission and mostly within the error of the measurement (± 0.1 eV). While peak fitting (see the Supplementary Materials for details) of these spectra indicates that initial deposition of TiO_2 leads to a slightly more oxidized Ir and Ru state, and a slightly more reduced Sn state for FTO, no trend with thickness was observed for any of the substrates, and changes in the oxidation state of the underlying catalyst are likely below the detection limit for the techniques used in this study (Fig S21, S22, and Table S5).

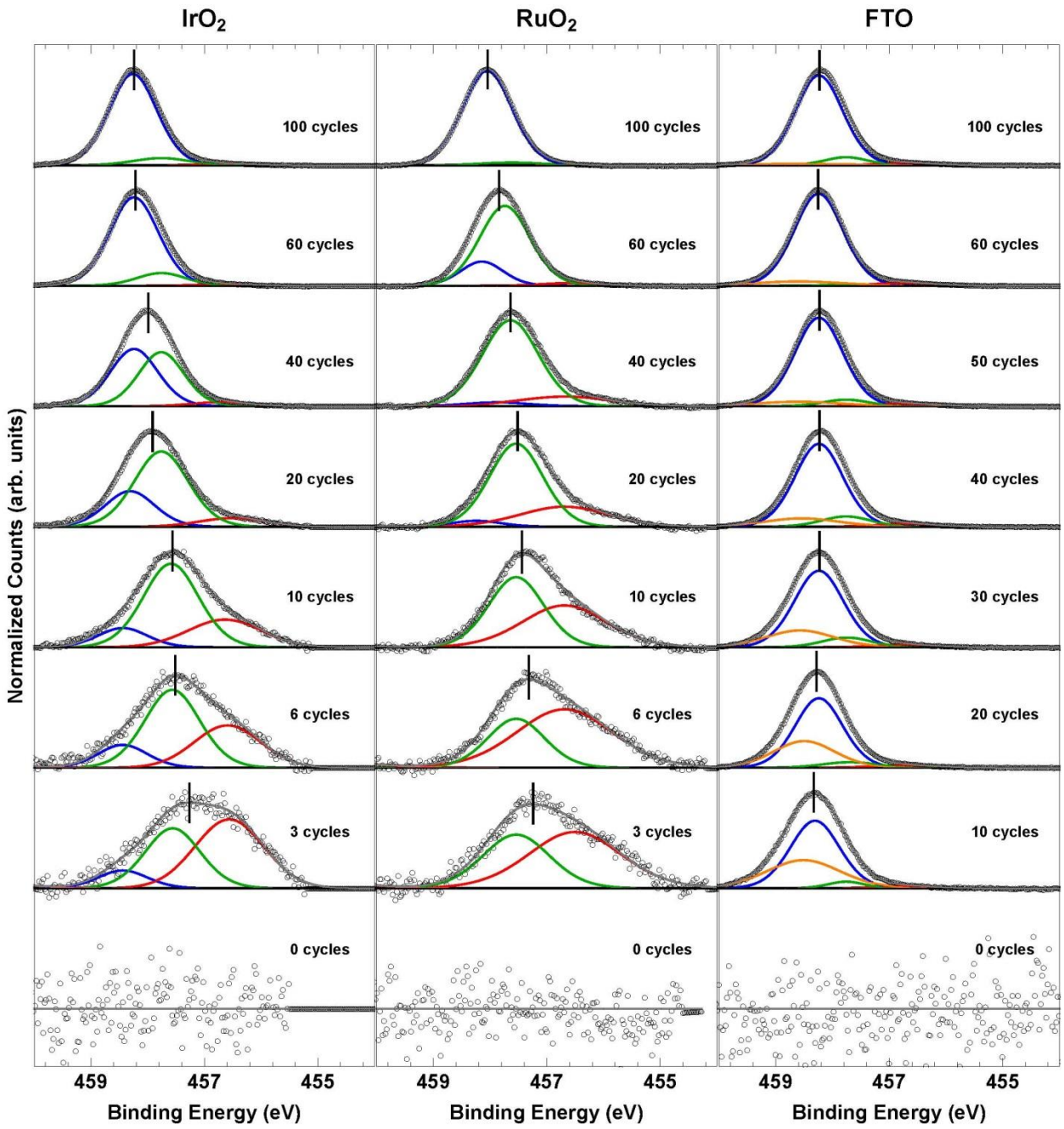

Fig. 4. X-ray photoelectron spectroscopy of the Ti $2p_{3/2}$ region for IrO_2, RuO_2, and FTO catalysts with varying TiO_2 thicknesses. Bulk TiO_2 is shown as the blue peak in each spectrum. The slightly and highly reduced Ti peaks are shown in green and red, respectively, and the most highly oxidized Ti peak is shown in orange. 0 cycles shows the noise of the instrument, no information is encoded in the height of the signal.

Economic Analysis:

To understand how improvements in catalyst activity could lead to reductions in the price of clean, electrochemical hydrogen, an economic analysis was performed. As discussed in chapter 1, in order to fully understand the cost of a catalyst, a model must incorporate the faradaic efficiency, material costs, voltage, and current density of a catalyst and the ways that these parameters change over time. To ensure a fair comparison, it is also important to measure all of these values in the same reaction conditions for the catalysts. Because these data are not fully available for the catalysts investigated herein, it is impossible to fully use equation 2 from chapter 1 to calculate the relative catalyst costs of these electrodes vs. the cost of a conventional electrode. However, the US Department of Energy publishes an open-access techno-economic model (H2A) to evaluate the cost of hydrogen from water electrolysis.[26] With some assumptions, it is possible to use the H2A model to estimate how activity enhancement may affect the price of clean, electrochemical hydrogen.

For this analysis, it was optimistically assumed that, for the catalysts investigated herein, all catalyst parameters remained the same as state of the art, except activity which was enhanced. The tafel slopes of the catalysts investigated herein were the same as conventional OER and CER catalysts, therefore we assumed that the shifts in overpotential observed in fig. 1 at low current densities would also occur at industrially relevant high current densities. Because RuO_2, when coated with 10 cycles of TiO_2, preformed the OER at 400 mV lower than the conventional OER, we assumed that our catalysts could operate at 400 mV lower cell voltage than the conventional water splitting catalyst. We also assumed that the catalysts described herein can achieve the same faradaic efficiency and stability metrics as conventional catalysts, although preliminary data indicates that this is not possible. According to the H2A model, this would reduce the voltage from 2 V to 1.6 V or from 54 kWhr/kg H_2 to 43 kWhr/kg H_2. This results in a drop in price from \$5.18/kg H_2 to \$4.12/kg H_2. According to the H2A model, the price of H_2 from steam methane reforming (SMR; the conventional H_2 production method) is \$1.25/kg H_2, far lower than what can be achieved with any of the catalysts investigated herein. Furthermore, even at 1.23 V, the thermodynamic limit, the price is \$3.18/kg H_2, still far too high to compete with SMR. These data indicate that, even with state-of-the-art stability, faradaic efficiency and current density (none of which the catalysts investigated herein have) any reduction in voltage is insufficient to make electrochemical H_2 cost competitive with H_2 from SMR. A more detailed analysis on catalysts for water electrolysis may be found in chapter 4.

Conclusion:

In summation, surface characterization suggests that atomic layer deposition of low cycle numbers of TiO_2 can tune surface electron densities of the catalyst in a direction consistent with predictions from group electronegativity concepts (Fig. S5). Given that concomitant changes in electrochemical activity were observed with deposition of TiO_2, these data indicate that ALD may be useful to tune the activity of other catalysts for diverse reactions, including those critical for renewable energy storage and wastewater treatment. However, unless other factors change like a carbon tax or a drop in electricity price, enhancement in activity could make electrochemical hydrogen production cost competitive with SMR.

Acknowledgements: Supporting data referenced above may be found in the supplementary materials. Supporting data referenced above may be found in the supplementary materials. This work was supported by the Bill and Melinda Gates Foundation (BMGF RTTC Grants OPP1111246 and OPP1149755). Research was in part carried out at the Molecular Materials Resource Center of the Beckman Institute of the California Institute of Technology. Funding was provided to C.E.F., J.T.J., and C.G.R. by the Resnick Institute for Sustainability at Caltech. In part, this material is based upon work performed by the Joint Center for Artificial Photosynthesis, a DOE Energy Innovation Hub, supported through the Office of Science of the U.S. Department of Energy under Award Number DE-SC0004993. C.E.F. was the primary concept generator for this work, led electrocatalyst activity, E_{zc}, and AFM data collection and analysis, and helped fabricate and characterize the electrocatalysts. S.T.O. helped to generate the concept for this work, fabricated and characterized the electrocatalysts, and helped with data analysis and experimental design. J.T.J. helped generate the concept of this work, helped design the electrochemical methodology, and helped collect electrochemical data. M.F.L. collected the XPS data and assisted in the fitting and analysis of XPS and impedance spectroscopy data. C.G.R. lead TEM characterization of the electro catalysts. C.E.F., S.T.O., and J.T.J. prepared the manuscript and N.S.L., M.R.H., M.F.L., and C.G.R. helped with its editing. All authors reviewed and contributed to the final manuscript. We would like to acknowledge Dr. Katharina Urmann and Sisir Yalamanchili for help dicing Si wafers, Jingjing Jiang for help analyzing AFM data, and Azhar Carim for help with SEM, and Laleh Majari Kasmaee for help with E_{zc} analysis. We would also like to acknowledge Prof. Stefan Zweifel and his group for foundational mentoring as well as Prof. Gretchen Hofmeister and Prof. Matt Whited for foundational chemical insight.

Conflicts of interest: The authors' institution (California Institute of Technology) has filed a U.S. patent application directly relating to the work described in the paper (patent application no. US20180087164A1, filed on Sept 28, 2017).

Notes and references:

1. M. R. Shaner, H. A. Atwater, N. S. Lewis and E. W. McFarland, *Energy & Environmental Science*, 2016, **9**, 2354-2371.
2. Z. W. Seh, J. Kibsgaard, C. F. Dickens, I. Chorkendorff, J. K. Nørskov and T. F. Jaramillo, *Science*, 2017, **355**, eaad4998.
3. Y. Yang, J. Shin, J. T. Jasper and M. R. Hoffmann, *Environmental Science & Technology*, 2016, **50**, 8780-8787.
4. K. Gong, F. Du, Z. Xia, M. Durstock and L. Dai, *Science*, 2009, **323**, 760-764.
5. L.-Å. Näslund, C. M. Sánchez-Sánchez, Á. S. Ingason, J. Bäckström, E. Herrero, J. Rosen and S. Holmin, *The Journal of Physical Chemistry C*, 2013, **117**, 6126-6135.
6. A. R. Zeradjanin, N. Menzel, W. Schuhmann and P. Strasser, *Physical Chemistry Chemical Physics*, 2014, **16**, 13741-13747.
7. H. Li, C. Tsai, A. L. Koh, L. L. Cai, A. W. Contryman, A. H. Fragapane, J. H. Zhao, H. S. Han, H. C. Manoharan, F. Abild-Pedersen, J. K. Norskov and X. L. Zheng, *Nature Materials*, 2016, **15**, 48-+.
8. L. Giordano, F. Cinquini and G. Pacchioni, *Physical Review B*, 2006, **73**, 045414.
9. K. S. Exner, J. Anton, T. Jacob and H. Over, *Angewandte Chemie-International Edition*, 2014, **53**, 11032-11035.
10. R. T. Sanderson, *Journal of Chemical Education*, 1954, **31**, 2.
11. R. T. Sanderson, *Science*, 1951, **114**, 670-672.
12. R. T. Sanderson, *Chemical bonds and bond energy*, Academic Press, New York, 2d edn., 1976.
13. R. T. Sanderson, *Chemical periodicity*, Reinhold Pub. Corp., New York,, 1960.
14. Z. Zhuang, W. Sheng and Y. Yan, *Advanced Materials*, 2014, **26**, 3950-3955.
15. L. Bu, N. Zhang, S. Guo, X. Zhang, J. Li, J. Yao, T. Wu, G. Lu, J.-Y. Ma, D. Su and X. Huang, *Science*, 2016, **354**, 1410-1414.
16. W. Kim, T. Tachikawa, D. Monllor-Satoca, H.-i. Kim, T. Majima and W. Choi, *Energy & Environmental Science*, 2013, **6**, 3732-3739.
17. K. Cho, D. Kwon and M. R. Hoffmann, *Rsc Advances*, 2014, **4**, 4596-4608.

18. Y. P. Khalil, *Engineering 360*, 2015.
19. M. A. Pellow, C. J. M. Emmott, C. J. Barnhart and S. M. Benson, *Energy & Environmental Science*, 2015, **8**, 1938-1952.
20. C. C. L. McCrory, S. Jung, I. M. Ferrer, S. M. Chatman, J. C. Peters and T. F. Jaramillo, *Journal of the American Chemical Society*, 2015, **137**, 4347-4357.
21. S. Trasatti, *Electrochimica Acta*, 2000, **45**, 2377-2385.
22. K. A. Stoerzinger, L. Qiao, M. D. Biegalski and Y. Shao-Horn, *The Journal of Physical Chemistry Letters*, 2014, **5**, 1636-1641.
23. A. J. Medford, A. Vojvodic, J. S. Hummelshøj, J. Voss, F. Abild-Pedersen, F. Studt, T. Bligaard, A. Nilsson and J. K. Nørskov, *Journal of Catalysis*, 2015, **328**, 36-42.
24. J.-M. Hu, J.-Q. Zhang and C.-N. Cao, *International Journal of Hydrogen Energy*, 2004, **29**, 791-797.
25. L. C. Seitz, C. F. Dickens, K. Nishio, Y. Hikita, J. Montoya, A. Doyle, C. Kirk, A. Vojvodic, H. Y. Hwang, J. K. Norskov and T. F. Jaramillo, *Science*, 2016, **353**, 1011-1014.
26. C. C. L. McCrory, S. Jung, J. C. Peters and T. F. Jaramillo, *Journal of the American Chemical Society*, 2013, **135**, 16977-16987.
27. S. Trasatti, *Journal of Electroanalytical Chemistry and Interfacial Electrochemistry*, 1971, **33**, 351-378.
28. S. Trasatti, *Journal of Electroanalytical Chemistry and Interfacial Electrochemistry*, 1972, **39**, 163-184.
29. A. N. Frumkin and O. A. Petrii, *Electrochimica Acta*, 1975, **20**, 347-359.
30. F. Werfel and O. Brummer, *Phys Scripta*, 1983, **28**, 92-96.
31. D. Gonbeau, C. Guimon, G. Pfisterguillouzo, A. Levasseur, G. Meunier and R. Dormoy, *Surf Sci*, 1991, **254**, 81-89.

Supplementary Materials

Enhancing the activity of oxygen-evolution and chlorine-evolution electrocatalysts by atomic layer deposition of TiO_2

Authors: Cody E. Finke[1,2,3]*, Stefan T. Omelchenko[3], Justin T. Jasper[1,2], Michael F. Lichterman[4], Carlos G. Read[2,4], Nathan S. Lewis[4], Michael R. Hoffmann[1,2,3,]*

Affiliations:

[1]The Linde Center for Global Environmental Science, Caltech, Pasadena, CA 91125, USA.

[2]The Resnick Sustainability Institute, Caltech, Pasadena, CA 91125, USA.

[3]Division of Engineering and Applied Science, Caltech, Pasadena, CA 91125, USA.

[4]Division of Chemistry and Chemical Engineering, Caltech, Pasadena, CA 91125, USA.

*Corresponding Authors: finkec@caltech.edu, mrh@caltech.edu

Table of Contents

Surface Topography Determinatiion and Surface Homogeneity

Transmission Electron miscroscopy

To better understand the surface morphology, TEM images were aquired of 10 and 40 ALD cycles of TiO_2 on IrO_2. Transmission-electron microscopy (TEM) samples of films were prepared using a focused Ga-ion beam (FIB) on a FEI Nova-600 Nanolab FIB/FESEM, with Pt and C protection layers being applied before being exposed to the FIB. High-resolution TEM (HRTEM) images and high-angle annular dark-field scanning transmission electron microscopy (HAADF-STEM) images were collected on an FEI Titan G2 S/TEM equipped with spherical aberration correctors on the image and probe-forming lenses at an accelerating voltage of 200 kV. STEM-EDS maps were acquired in the FEI Titan using the Super-X EDX quad detector system at a current of 0.1 nA. Standard-less Cliff-Lorimer quantification was performed on the deconvoluted EDS line intensity data using the Bruker Esprit software. Fig. S1 below shows HAADF-STEM images of 10 cycles of TiO_2 exhibited a semicontinuous film where the majority of imaged areas were covered withTiO_2 with relatively small gaps of what appeared to be uncoated area. 40 ALD cycle exhibited a fully continuous film for at all areas imaged.

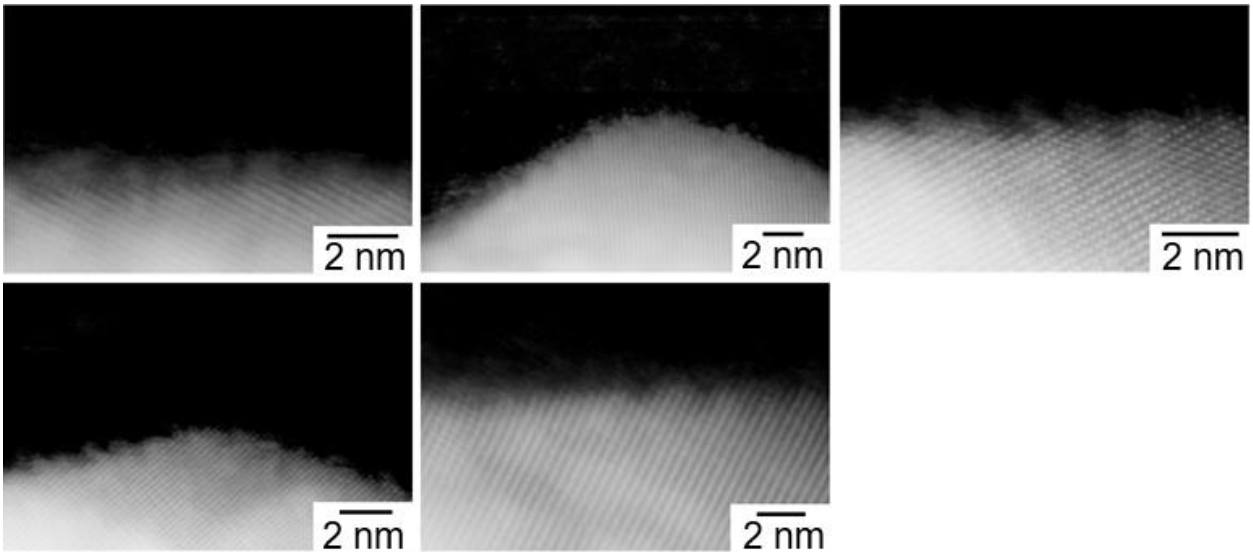

Fig. S1. High-Angle Annular Dark-Field Scanning Transmission Electron Microscopy (HAADF-STEM) images of different IrO_2 + 10 ALD cycles of TiO_2 samples. The crystalline sublayer is IrO_2 and the hairy top layer is amorphous TiO_2.

Atomic Force Microscopy

Atomic Force Microscopy (AFM) was used to investigate the surface morphology. A Bruker Dimension Icon was used in Peak Force Tunneling AFM Mode (PF-TUNA) for all topography and conductive AFM measurements. Representative surface topology (Fig. S2) and conductive AFM (TUNA current) (Fig. S3) for 0, 3, 10, and 1000 ALD TiO_2 cycles are shown for IrO_2, RuO_2, and FTO substrates. AFM images of RuO_2, IrO_2, FTO, and substrates coated with 1000 cycles of TiO_2 were consistent with previously reported images of materials grown under similar conditions [1-4].

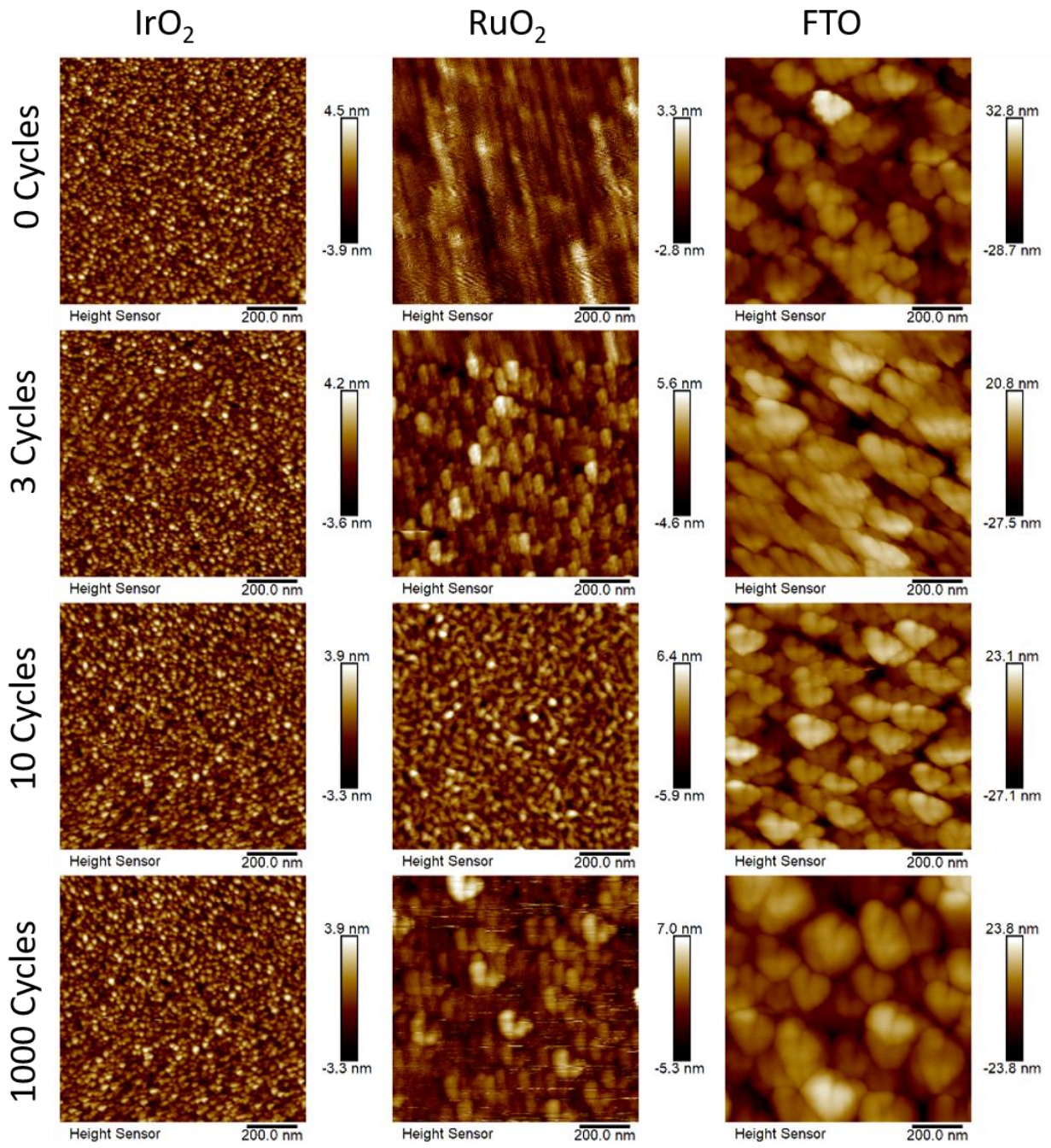

Fig. S2. Representative topographic atomic force microscopy images of IrO_2, RuO_2, and FTO each with 0, 3, 10, and 1000 ALD cycles of TiO_2.

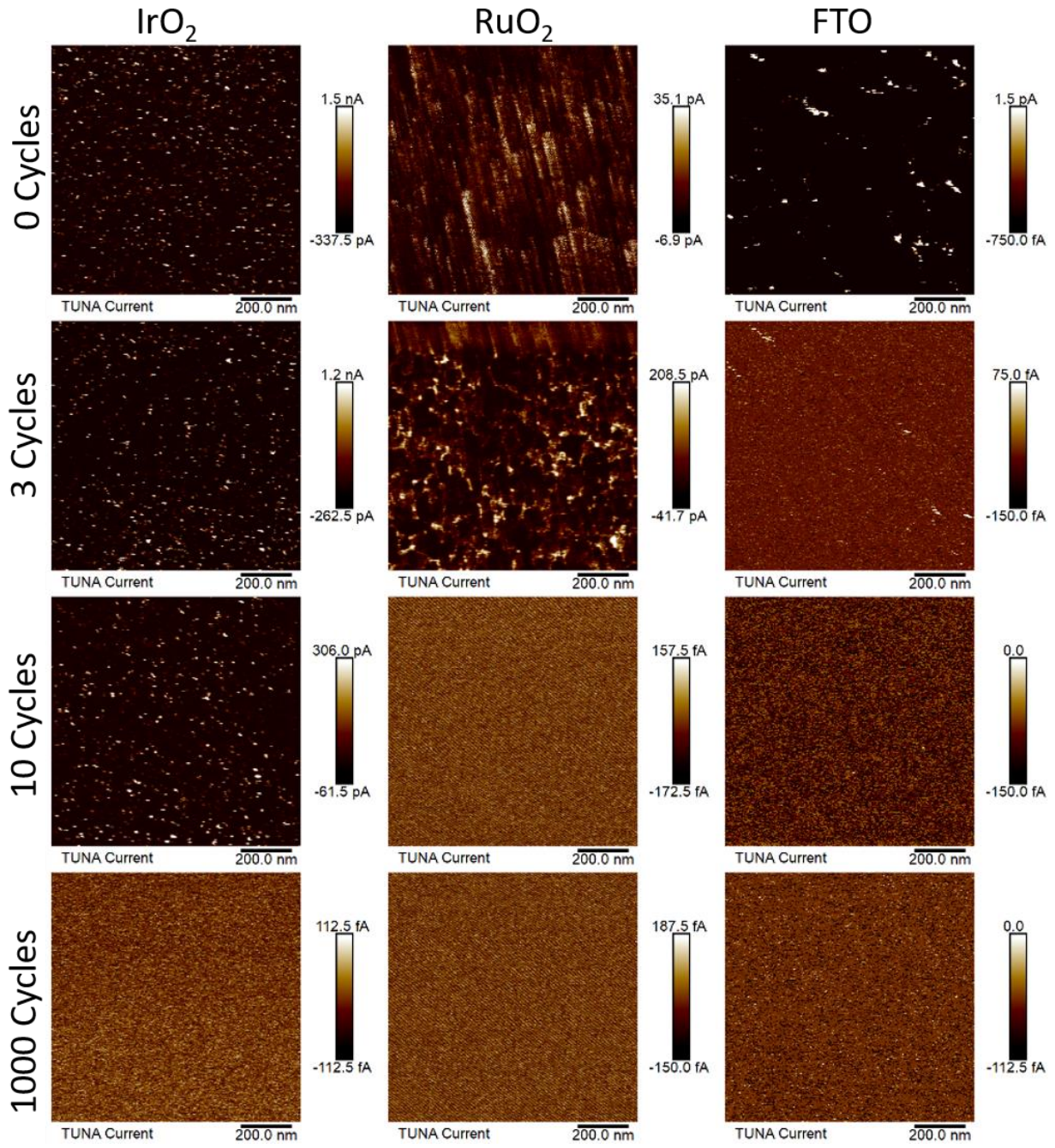

Fig. S3. Representative conductive atomic force microscopy tunneling current images of IrO_2, RuO_2, and FTO each with 0, 3, 10, and 1000 ALD cycles of TiO_2.

Table S1. Surface area (measured by AFM) as a percent of geometric surface area. Dividing these values by 100 yields topographic roughness factors.

	AFM Measured Surface Area as a Percentage of Geometric Surface Area		
TiO_2 Cycle Number	**IrO_2**	**RuO_2**	**FTO**
0	104.52%	107.75%	108.35%
3	103.87%	102.45%	107.98%
6	103.12%	103.93%	110.24%
10	102.94%	104.08%	108.05%
20	103.32%	104.61%	110.60%
30			108.92%
40	102.70%	102.61%	108.27%
50			108.18%
60	103.60%	101.65%	108.10%
500	102.00%		
1000	102.01%	111.02%	104.15%

The surface area as measured by AFM was at most 112% of the geometric surface area (Table S1). For IrO_2 and FTO, the surface topography was similar for all cycle numbers of TiO_2. The only observable change as the number of ALD cycles increased was that the conductivtiy and surface area decreased uniformly as TiO_2 was deposited, suggesting that TiO_2 coated the catalysts' surface reasonably evenly, see Fig. S1 for TEM images for higher resolution coverage analysis. Based on AFM data, No holes were visible in the TiO_2 coating at any cycle number for FTO and IrO_2. The surface topography of bare RuO_2 was rippled (0 cycles), and gradually morphed into a flake-like structure (3-6 cycles), a columnar structure similar to IrO_2 (10-30 cycles), and then back into flakes similar to FTO (>30 cycles). Furthermore, for RuO_2 at 3 ALD cycles some holes in the TiO_2 were clearly visible in both the topological and the conductive AFM images. No such holes were visible at > 3 cycles TiO_2. Conductive AFM showed uniformly drecreasing conductivity with cycle number once no holes were visible (>3 cycles TiO_2).

Profilometry

Profilometry was performed on a Bruker DektakXT Stylus profilometer. TiO_2 ALD growth rates on FTO were determined by masking a portion of the FTO sample with Dupont Kapton Tape (Dupont, WA) and then using the profilometer to scan across the TiO_2 boundary after deposition. A 1000 cycle sample was scanned 3 times and the TiO_2 thickness was determined to be 50.8 ± 2.1 nm. The growth rate was therefore ~0.5 Å/ALD cycle, assuming that growth was linear, which corroborates previously reported gowth rates measured using the same ALD recipe on the same instrument [5].

Scanning Electron Miscroscopy

Scanning electron micrographs (SEMs) were obtained with a FEI Nova NanoSEM 450 at an accelerating voltage of 5.00 kV with a working distance of 5 mm and an in-lens secondary electron detector**.** Based on cross-sectional SEM images of films subjected to 1000 cycles of ALD, linear growth rates were estimated to be ~0.65 Å/ALD cycle (Fig. S4), in reasonable agreement with profilometry results as well as with previously measured growth rates [5].

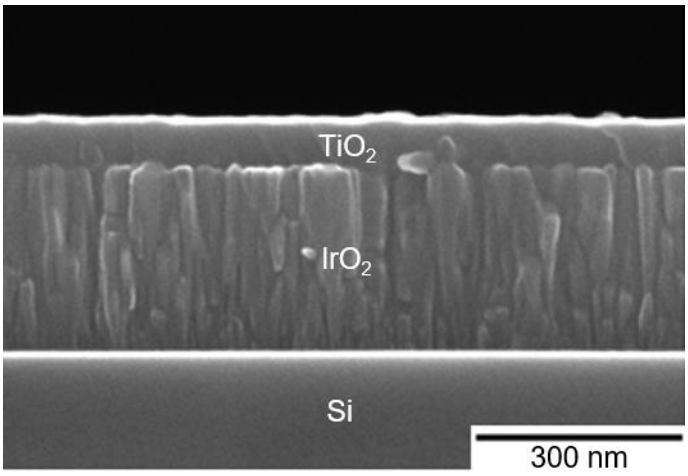

Fig. S4. A cross-sectional SEM image of a sample consisting of a silicon wafer substrate sputter coated with IrO_2 and then overcoated with 1000 cycles of ALD TiO_2.

Estimation of Electronegativity:

Electronegativities were estimated for heterogeneous electrocatalysts by taking the geometric mean of the electronegativities of the constituent atoms [6, 7]. Allen scale electronegativities were used because this scale is better than other electronegativity scales (e.g. Pauling, Mulliken, Allred-Rochow) at differentiating between the electronegativities of the transition metals [8-10]. As an example, for TiO_2: Ti ($\chi = 1.38$) and O ($\chi = 3.61$), therefore TiO_2 ($\chi \approx (1.38 \times 3.61^2)^{1/3} = 2.62$). In the case of FTO, the electronegativity of SnO_2 was estimated because it is not known how small quantities of F would change the electronegativity of SnO_2. Electronegativity is a useful theoretical concept for estimating the directions in which surface charge availability and the corresponding catalyst-reacting-species bond strength may move, but not to estimate the magnitude of change or any complex details of any physical parameter.

To better understand how group electronegativities may be correlated with catalytic activity for heterogeneous electrocatalysts, group electronegativities were calculated for oxygen evolution catalysts from this work and for the catalysts compared in Seh *et al.* and plotted against overpotentials at 1 mA/cm^2_{AFMSA} for each catalyst. Like in Seh *et al*., for catalysts with no AFM data, if they were prepared on flat substrates (e.g. (100) silicon), a roughness factor of 1 was assumed. (Fig. S5) [11]. In the case of catalysts with undefined elemental ratios, XPS data on the oxidation state was used to estimate elemental composition, and then fractional compositions were rounded to the nearest half. If there was no XPS data, Pourbaix diagrams were consulted and the predominant species at the relevant potentials were used for group electronegativity calculations. In most cases, assumptions were the same as the assumptions made for active site composition in Seh *et al*. For layered catalysts (e.g. $IrO_x/SrIrO_3$) the geometric mean of all the atoms in the overlayer and underlayer was used as the group electronegativity of the material. Overpotentials at 1 mA/cm^2_{AFMSA} was either taken from Seh *et al.* or from this work. Most overpotential data presented in Fig. S5 was collected in a basic electrolyte (blue circles), for catalysts tested in acidic electrolytes, red circles

indicate values from this work measured in 1 M H_2SO_4 and the orange circle indicates the catalyst tested in 0.5 M H_2SO_4 from Seitz *et al.* [12]. Electronegativity, like other theoretical constructs that are related to bond strength, demonstrates a nice volcano type correlation with activity for the oxygen evolution reaction [12]. These data presented in Fig. S5 below and the data presented in Fig. 2 of the main text, indicate that group electronegativity may be a simple and useful tool to choose candidates for heterogeneous electrocatalysts. No Allen Scale electronegativity exists for Lanthanum so the geometric mean of Barium and Lutetium (the most adjacent atoms to Lanthanum with known Allen Scale electronegativities) was used instead resulting in an $\chi_{La} = 0.98$.

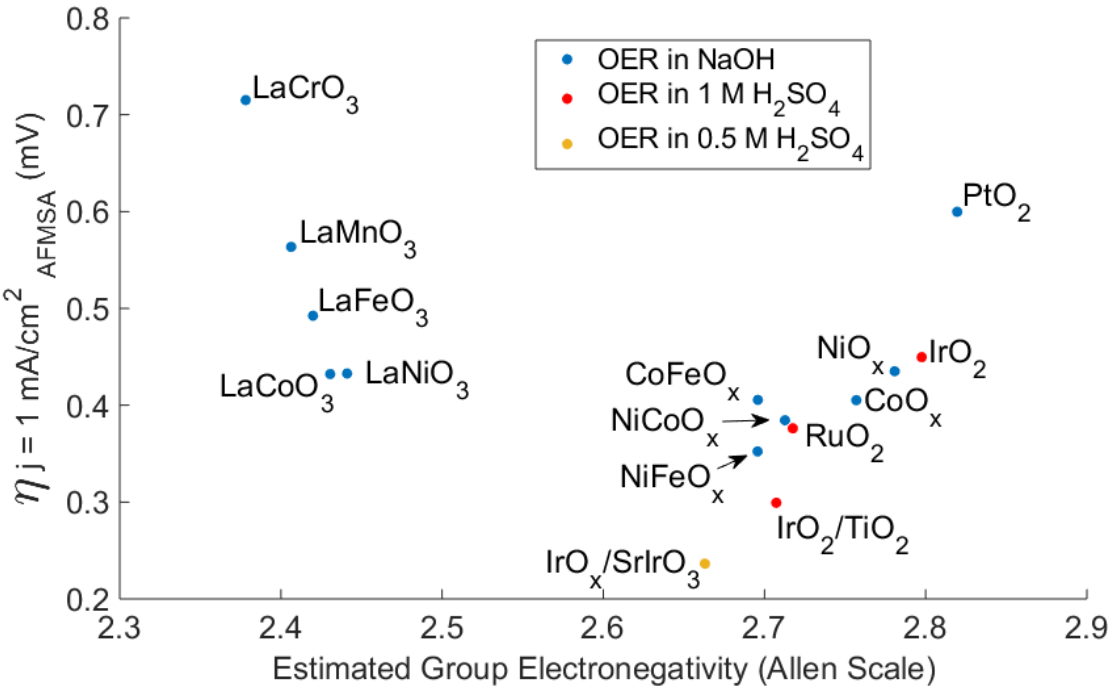

Fig. S5. Group electronegativity vs overpotential at 1 mA/cm^2_{AFMSA}. Overpotential data was taken from Seh *et al.* (blue and orange circles) and from this work (red circles). For $LaCrO_3$, $LaMnO_3$, $LaFeO_3$, $LaCoO_3$, $LaNiO_3$, RuO_2, IrO_2, and PtO_2 group electronegativites were estimated by taking the geometric mean of the Allen Scale electronegativities of the constituent atoms. For $IrO_x/SrIrO_3$, Ir_2SrO_7 was assumed for group electronegativity calculations [12]. For IrO_2/TiO_2, $IrTiO_4$ was assumed for group electronegativity calculations For $NiFeO_x$, $NiFe_2O_4$ was was assumed for group electronegativity calculations [13]. For $NiCoO_x$ $NiCo_2O_4$ was assumed for group electronegativity calculations [13]. For $NiCoO_x$, $NiCo_2O_4$ was assumed for group electronegativity calculations [13]. For

$CoFeO_x$, $FeCo_2O_4$ was assumed for group electronegativity calculations [13]. For CoO_x, $CoO_{1.5}$ was assumed for group electronegativity calculations [13]. For NiO_x, Ni_2O_3 was assumed for group electronegativity calculations [13].

Electrode Preparation:

RuO_2 and IrO_2 Sample Preparation

(100) oriented, boron doped, < 0.01 Ω-cm, 525 ± 25 μm thick p^+-Si wafers were obtained from Addison Engineering (San Jose, CA). Wafers were cleaned for 1 min in buffered HF (Transene, Danvers, MA, used as received) and then immediately put under a vacuum of < 7 x 10^{-6} Torr. ~300 nm of RuO_2 or IrO_2 were deposited on the wafer using an AJA International Inc. (Scituate, MA) Orion sputter-deposition system equipped with Phase II-J software. Samples were heated to 300 ºC and Ir or Ru were sputtered using an RF source under an Ar/O_2 plasma with a constant flow of 20 sccm Ar and 3 sccm O_2 for 22.42 min for Ir, and 13.5 sccm Ar and 1.5 sccm O_2 for 22 min for Ru. The chamber pressure was maintained at 5 mTorr during deposition, and the base pressure of the chamber was held at < 10^{-7} Torr between depositions. The phase purity of the samples was confirmed by X-ray diffraction measurements, as detailed below (Fig. S6).

Following ALD of TiO_2 (see below), a tungsten-carbide-tipped scribe was used to contact a gallium-indium eutectic (Alfa Aesar, Ward Hill, MA, 99.99%, used as received) onto the back side of the IrO_2 and RuO_2 samples. A coiled zinc-plated copper wire (Consolidated Electrical Wire and Cable, Franklin Park, IL) was placed onto the gallium-indium and the wire was covered with one-sided copper foil tape (3M, Maplewood, MN, used as received).

XRD crystal structures of the IrO_2 and RuO_2 substrate are shown in Fig. S6 below.

FTO Sample Preparation

Tec 15 FTO glass slides (Hartford Glass Co., Hartford City, IN) were broken into ~1 cm^2 pieces. The FTO pieces were then washed in a sonication bath in acetone, isopropyl alcohol, and deionized water, sequentially, for 15 min at each step. ALD of TiO_2 was performed as described below. A coiled zinc-plated copper wire (Consolidated Electrical Wire and Cable) was placed onto the conductive side of the FTO electrode and secured with one-sided copper foil tape.

To protect the contact and define the geometric surface area, circular holes were punched in a strip of 1-inch width 3M vinyl electroplating tape using a 2 or 3 mm diameter circular punch. The entire electrode was then covered with this tape, only exposing the 3 mm diameter circle of the electrode. The wire covered the tape for at least 4 cm, such that neither the wire housing nor the metallic wire was exposed to the electrolyte. After testing, electrodes were inspected for leaks and then disassembled and the copper contacts were checked for corrosion to ensure no leaking. Baseline and peak overpotentials were confirmed during stability testing using epoxy sealed electrodes (Table S4).

Atomic Layer Deposition

TiO_2 films were deposited on IrO_2, RuO_2 and FTO at 150 °C using an Ultratech Fiji 200 Plasma ALD System (Veeco, Waltham, MA). The IrO_2, RuO_2, and FTO were prepared as described above. Prior to ALD, one 0.060 sec pulse of H_2O was applied to the sample. Each ALD cycle consisted of a 0.250 sec pulse of tetrakis(dimethylamido)titanium (TDMAT, Sigma-Aldrich, St. Louis, MO, 99.999%, used as received), followed by a 0.060 sec pulse of H_2O (18 MΩ cm, Millipore). A 15 sec purge under a constant 0.13 L/min flow of research-grade N_2 was performed between each precursor pulse. While idle, the ALD system was maintained under a continuous N_2 purge with a background pressure of 0.50 Torr.

X-Ray Diffraction

X-ray diffraction (XRD) measurements were performed with a Bruker D8 Discover equipped with a 2-dimensional Vantec-500 detector. Copper K_α radiation (1.54 Å) was generated with a tube voltage of 50 kV and a tube current of 1000 μA. The incident beam was focused with a 0.5 mm diameter mono-capillary collimator. An aligned laser beam was used to ensure that the sample was placed at the correct depth for diffraction measurements. Coupled theta/two-theta mode was used. The scattered X-ray radiation was collected by the Vantec-500 detector with an angular resolution < 0.04°, which enabled the collection of diffraction from a 2θ range of 20°. To obtain the XRD profile, four scans were performed in the range of 10° to 90° 2θ, and radiation was counted for a total duration of 1 h. The collected data were analyzed using Bruker EVA software. All observed peaks were indexed to standard diffraction patterns for IrO_2 and RuO_2, respectively, from the Inorganic Crystal Structure Database [14, 15].

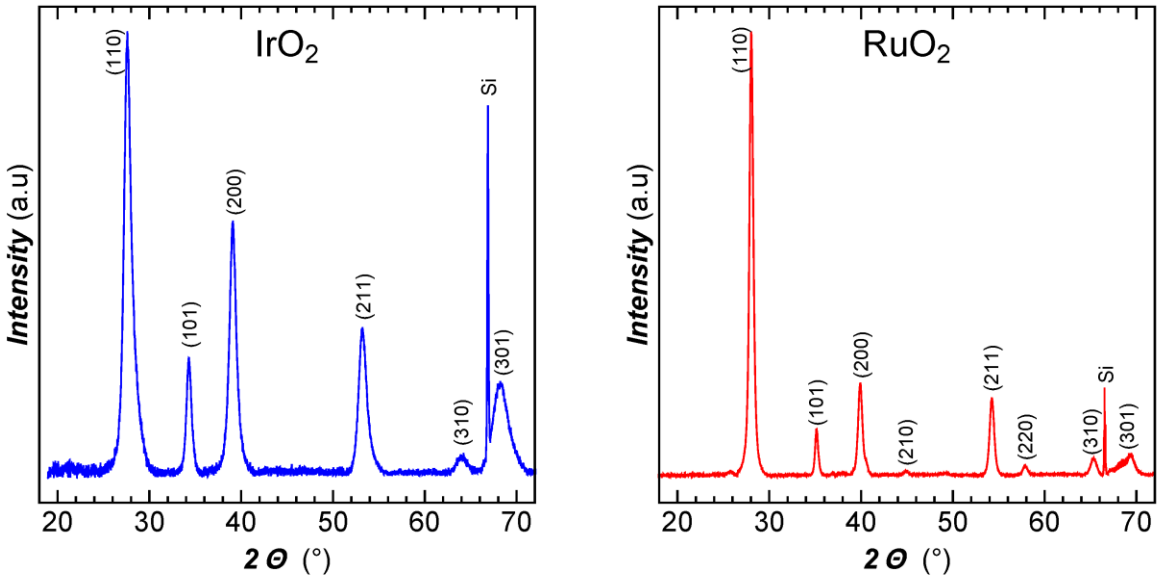

Fig. S6. X-ray diffraction patterns for typical IrO_2 and RuO_2. All observed peaks were indexed to standard diffraction patterns for IrO_2 and RuO_2, respectively.

Electrochemical measurements

With assistance from a large-gauge needle guide, the lead of each electrode was inserted through a rubber septum, and the electrode was placed in a 25 mL, 14/20, 4-necked, round bottom flask (Chemglass, Vineland, NJ). The flask was filled with 15 mL of 1.0 M H_2SO_4 or 5.0 M NaCl at pH

2.0 (adjusted using HCl and measured using a calibrated Thermo Scientific Orion 3 Star pH probe). A saturated calomel electrode (SCE; CH Instruments, Austin, TX) reference electrode was washed and placed in the solution.

For OER and CER experiments, O_2(g) or Cl_2(g) was flowed through a bubbler that contained either 1.0 M H_2SO_4 or 5.0 M NaCl at pH 2.0, respectively, and then into the reactor using a Teflon tube that extended ~1 cm below the surface of the electrolyte. To ensure that the reactor was pressurized to 1 atm, gas could freely escape through an identical Teflon tube that went from the reactor flask to the back of the fume hood. Prior to data collection, the gas was bubbled through the solution for > 1 min. The counter electrode was a 0.5 mm diameter coiled platinum wire (Sigma Aldrich, 99.9%). All purging and experiments were performed under continuous stirring. The distance between the working electrode and reference electrode was 1.0 cm.

To measure overpotential, the following experiments were run on a Bio-Logic (Seyssinet-Pariset, France) potentiostat/galvanostat model VSP-300 with EIS capability:
1) Open circuit voltage for 30 sec.
2) Two cyclic voltammograms (CVs) to clean the electrode, scanning from 1.0 to 1.45 vs SCE for RuO_2 and IrO_2 in 1.0 M H_2SO_4 (prior to OER); from 1.2 to 1.8 vs SCE for FTO in 1.0 M H_2SO_4 (prior to OER); from 1.1 to 1.2 V vs SCE for RuO_2 and IrO_2 in 5.0 M NaCl at pH 2.0 (prior to CER); and from 1.1 to 2.0 V for FTO in 5.0 M NaCl at pH 2.0 (prior to CER).
3) Hold the potential at open circuit for 30 sec.
4) Two CVs to measure the overpotential, scanning from 1.0 to 2.5 vs SCE for RuO_2 and IrO_2 in 1.0 M H_2SO_4 (OER), 1.5 to 3.5 for FTO in 1.0 M H_2SO_4 (OER), 1.1 to 1.35 V vs SCE for RuO_2 and IrO_2 in 5.0M NaCl at pH 2.0 (CER), and for 1.1 to 3.0 V FTO in 5.0 M NaCl at pH 2.0 (CER).

All CVs were conducted at a 5 mV/sec scan rate and were corrected for solution resistance as described below, unless otherwise stated. The system resistance was also measured for each sample prior to each experiment. For each electrode, at least 4 replicates were tested.

Overpotential Calculations

For the OER, standard conditions were assumed, and the thermodynamic potential of 1230 mV vs RHE was used to determine the OER overpotential at 10 mA/cm^2.

For the CER, the activity for Cl^- was estimated to be 4.36 using the Pitzer model [16] and the fugacity of 1 atm Cl_2 was taken to be 0.07267 [17]. Using these values, a thermodynamic potential of 1288 mV vs NHE was calculated from the Nernst equation.

Faradaic Efficiency Determination

For the OER, the faradaic efficiency of the electrodes was measured as previously described using a pneumatic trough [18]. A graduated cylinder was filled with electrolyte and placed upside down in a bath of electrolyte. The working electrode was inserted to a height > 1 cm into the cylinder. The reference electrode was placed near the cylinder and the counter electrode was placed > 5 cm away from the cylinder. The cylinder was closed to the bulk solution except for the pour spout of the cylinder, hence ions were allowed to pass freely. The electrode was biased to pass 10 mA of current at 10 mA/cm^2_{geo}, and the resulting oxygen bubbles were collected in the cylinder for 1 h. The resulting head-space volume was measured and compared using the ideal gas law to the expected total charge passed. Similar to other studies, 105-115% faradaic efficiencies were measured (Table S2). The excess is attributed to electrolyte sticking to the cylinder walls, narrowing the diameter of the cylinder.

For the CER, electrodes were operated at a constant current of $1mA/cm^2_{geo}$ for 10 min in 15 mL of 5.0 M NaCl at pH 2.0, which, given 100% faradaic efficiency, should yield 22.08 ppm $Cl_2(g)$ in our experimental configuration. Immediately after the reaction, one milliliter of electrolyte was transferred to a 25 mL beaker and chlorine was measured by titrating excess potassium iodide with a starch indicator using 0.50 mN $Na_2S_2O_3$ [19]. Greater than 90% faradaic efficiency was measured for samples with 40-60 ALD cycles of TiO_2 and greater than 95% faradaic efficiency was measured for samples with fewer than 40 ALD cycles of TiO_2 (Table S2).

Table S2. Faradaic efficiencies for the OER and CER.

	OER			CER		
TiO_2 Cycle Number	**IrO_2**	**RuO_2**	**FTO**	**IrO_2**	**RuO_2**	**FTO**
0	108%	122%	114%	101%	95%	97%
1			86%	96%	99%	102%
3	120%	122%	97%	99%	96%	96%
6	120%	107%	103%	101%	96%	98%
10	114%	122%	114%	96%	99%	96%
15		114%				
20	117%	122%	114%	104%	95%	98%
25			114%			
30	120%	114%	114%			
40	108%	114%	114%	95%	91%	91%
50	103%	114%				
60	120%	114%	103%	91%	95%	113%
100	114%	107%	114%	92%	91%	15%

24-h Stability Testing

For each catalyst, the uncoated and the most active, coated catalysts were tested for 24 h stability. For the OER, IrO_2 with 40 ALD cycles of TiO_2 was also tested. 10 mA/cm^2 in 1 M H_2SO_4 Electrodes were as prepared as described above except, instead of vinyl tape, electrode surface area was defined by Hysol 9460 epoxy (Henkel, Dusseldorf, Germany) [12]. Geometric surface areas were measured as previously described by scanning the electrode surface using a Ricoh MP 301 scanner (Tokyo, Japan) and estimating the surface area using ImageJ software [12]. The catalyst stability was assessed by maintaining the electrodes galvanostatically at either 10 mA/cm^2 or 1 mA/cm^2 for the OER and

CER, respectively, for 24 hrs. At 0 min, 10 min, 2 h, and 24 h, the electrolyte was replaced with fresh electrolyte, and either O_2(g) or Cl_2(g) was bubbled through the solution as described above. After > 1 min of gas bubbling, electrochemical impedance spectroscopy was preformed to determine the system resistance followed by 5 CVs which were run from the OCV to a potential that yielded 10 mA/cm^2 or 1 mA/cm^2 for the OER and CER, respectively. The voltage required to reach 10 mA/cm^2 for the OER and 1 mA/cm^2 for the CER, respectively, is tabulated in Table S4 below. Initial overpotential measurements agree well with overpotential measurements using vinyl tape on electrodes reported in Fig. 1 (Table S3). In general, for the OER small cycle numbers of TiO_2 ($\leq$ 10) extended the lifetime of the catalysts from <1 h to <4 h and thicker coatings ($\geq$ 30) extended the catalyst lifetime to > 7 h. As previously reported for thin IrO_x catalysts for the OER, the overpotential to reach 10 mA/cm^2 rapidly increased after < 1 h of testing. For the CER, all catalysts were reasonably stable over the 24 h testing period except for the less stable FTO catalysts which followed a similar pattern as OER catalysts. A sample 24 h stability test of 0, 10, and 40 ALD cycles of TiO_2 on IrO_2 under OER conditions is presented in Fig. S7 below.

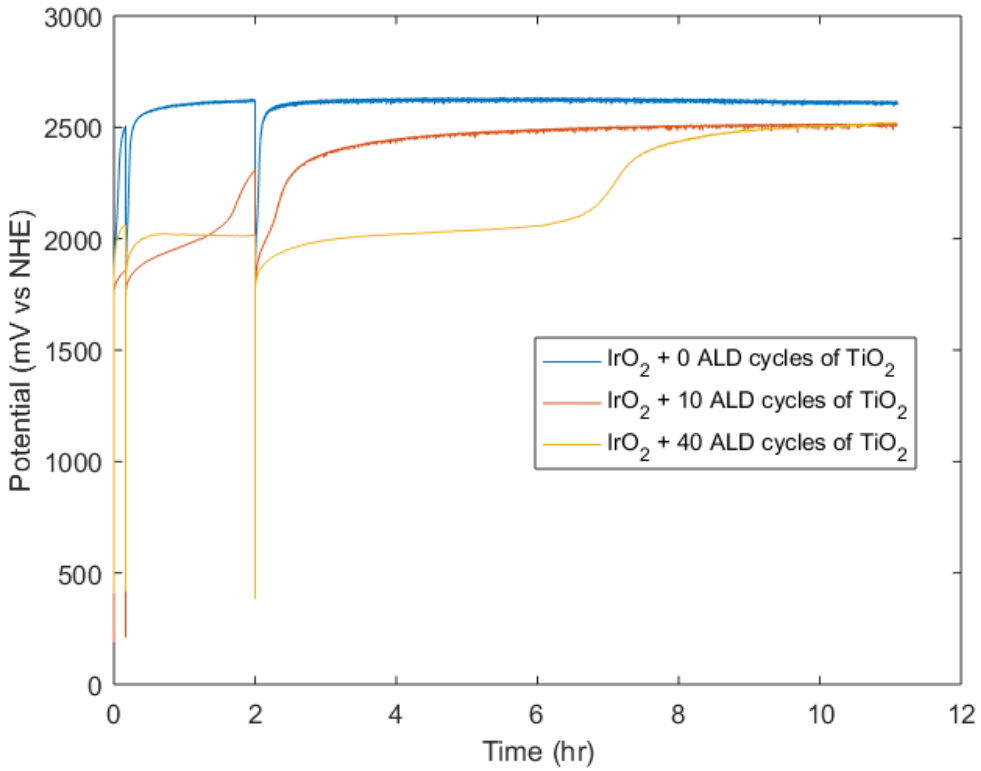

Fig. S7. Example stability testing data of IrO_2 + 0 (blue), 10 (orange), and 40 (yellow) ALD cycles in 1 M H_2SO_4 at 10 mA/cm^2_{geo}.

Table S3. Summary of overpotential data as measured from CVs to reach 10 mA/cm^2_{geo} in 1 M H_2SO_4 for the OER and 1 mA/cm^2_{geo} in 5 M NaCl pH 2.0 for CER at 0 min, 10 min, 2 h, and 24 h of testing in constant current mode. The right-most column displays the overpotential that was reported in the main text. N/A indicates that a rapid loss in activity was noticed before the time of measurement.

OER overpotential to reach 10 mA/cm^2_{geo}

MO_x + X ALD Cycles of TiO_2	initial	10 min	2 h	24 h	Reported initial value (Fig. 1.)
IrO_2 + 0 cyc	720	670	N/A	N/A	710 ± 30

IrO_2 + 10 cyc	540	510			520 ± 20
			N/A	N/A	
IrO_2 + 40 cyc	800	610	560		810 ± 50
				N/A	
RuO_2 + 0 cyc	770	880	N/A		740 ± 70
				N/A	
RuO2 + 10 cyc	430	470	440	N/A	430 ± 10
FTO + 0 cyc	1870	1820			1870 ± 50
			N/A	N/A	
FTO + 30 cyc	1740	1620			1720 ± 70
			N/A	N/A	

CER overpotential to reach 1 mA/cm$^2_{geo}$

IrO2 + 0 cyc	160	220	230		148 ± 6
				N/A	
IrO2 + 3 cyc	120	200	200	190	122 ± 5
RuO2 + 0 cyc	140	220	140	210	116 ± 6
RuO2 + 60 cyc	160	160	100	100	160 ± 10
FTO + 0 cyc	870	980	990	970	890 ± 30
FTO + 10 cyc	760	1150	1000	740	760 ± 40

Determination of Solution and System Resistance

The solution resistance was estimated using electrochemical impedance spectroscopy on a coiled Pt wire working electrode and Pt wire counter electrode system. The wire coil was 3 mm in diameter to simulate the working electrode and was placed 1 cm from the SCE reference electrode to simulate the distance between working and reference electrode. Measurements were taken in 5.0 M NaCl at

pH 2.0 under 1 atm Cl_2 (CER) or in 1.0 M H_2SO_4 under 1 atm O_2 (OER). No correction was performed for the resistance of the Pt electrodes, due to the low resistivity (< 0.0001 Ω/cm) of Pt. For 5.0 M NaCl at pH 2.0, a solution resistance of 3.45 ± 0.02 Ω was measured. For 1.0 M H_2SO_4, a solution resistance of 1.91 ± 0.02 Ω was measured. These values were used to correct the electrodes for the IR drop. No correction was made for the electrode resistivity, as it is an intrinsic electrode property. Typical corrections from solution resistance were ~1.4 mV and ~0.3 mV for the OER at 10 mA/cm^2_{geo} and the CER at 1 mA/cm^2_{geo} respectively.

The system resistance was also measured as described above, but instead of Pt wire TiO_2 coated IrO_2, RuO_2, and FTO electrodes were used as the working electrodes. The measured solution resistance was a lower bound for the system resistances (Fig. S8). Data was not corrected for system resistance because this is an intrinsic property of the electrode. Neither the magnitude nor the shape of the change in overpotential or specific activity shown in Fig. 1 were explained by the magnitude or the pattern of the system resistivity which would have resulted in corrections of < 10 mV for the OER and < 3 mV for the CER.

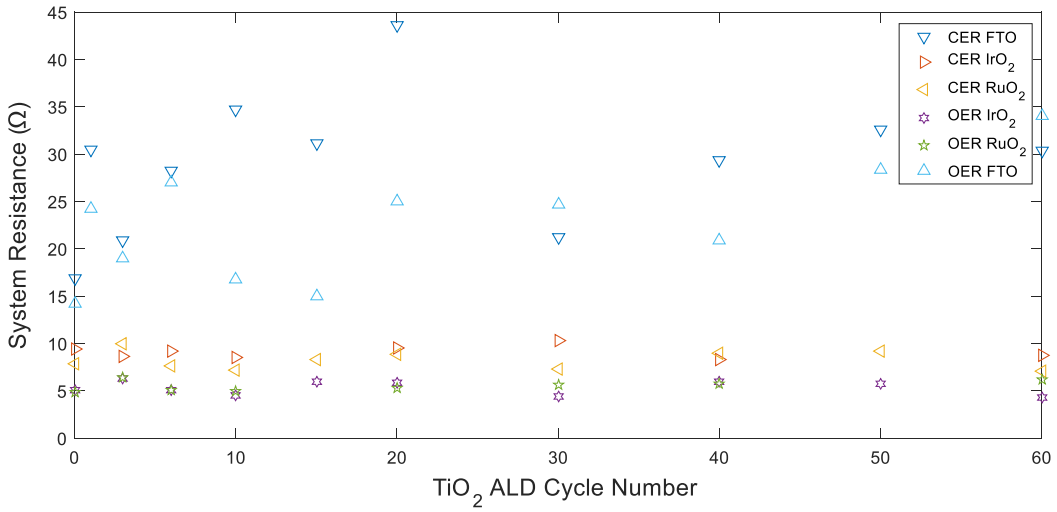

Fig. S8. System resistance as measured by electrochemical impedance spectroscopy in 5.0 M NaCl at pH 2.0 (CER) and 1.0 M H_2SO_4 (OER). The resistivity of the system did not appreciably change between 0 and 60 ALD cycles of TiO_2. For IrO_2 based electrodes, the average system resistance was 9.1 ± 0.6 Ω for CER condtions and 5.4 ± 0.6 Ω for OER conditions. For RuO_2 based electrodes, the average system resistance

was 8.0 ± 1.0 Ω for CER condtions and as 5.3 ± 0.7 Ω for OER conditions. For FTO-based electrodes, the average system resistance was 30 ± 7 Ω for CER condtions and 23 ± 6 Ω for OER conditions.

Determination of Specific Activities

Determination of the Double-Layer Capacitance and Electrochemically Active Surface Area

In order to make a fair comparison between values herein and in the benchmarking study, the double-layer capacitance (C_d) was measured and linearly related to the electrochemically active surface area (ECSA) by Eq. S1 in the same manner as described in the benchmarking literature [13]. For the OER, briefly, C_d was measured by plotting the non-Faradaic current vs scan rate and extracting the slope of the linear best-fit line. An initial CV was conducted to identify the non-faradaic region, which in general was a 50 mV window around the open-circuit potential (E_{oc}). Scans were then conducted at scan rates of 0.005, 0.01, 0.025, 0.05, 0.1, 0.2, 0.4, and 0.8 V/s and 100% of the current was collected for each step (Fig. S9). Between potential sweeps, the working electrode was held at E_{oc} for 30 sec. The non-faradaic current at E_{oc} for each scan rate was plotted versus scan rate (Fig. S9). The average of the absolute value of the positive and negative slopes of the linear fits of the data was taken to be C_d. Because of the narrow potential window between oxidation of Cl^- and reduction of Cl_2, C_d was determined from electrochemical impedience spectroscpy at E_{oc}. Nyquist plots were fit to a resistor in series with a parallel combination of a capacitor and a shunt resistor (Fig. S10). The resulting capacitance was taken as the C_d. In both cases C_d values were used as described previously to calculate the ECSA [13]. Briefly, C_d was divided by the specific capacitance (C_s) of an average metal substrate in an acidic electrolyte (Fig. S11, Eq. S1). Few literature values exist for C_s in concentrated acidic brine, and C_s does not change appreciably with ionic strength for H_2SO_4. Both the CER and OER electrolytes were acidic, so the same value of C_s was used to calculate the ECSA for both the CER and OER:

$$\text{ECSA} = C_d / C_s \qquad \text{Eq. S1}$$

where C_S is specific capacitance (i.e., 0.035 mF/cm^2 for 1.0 M H_2SO_4 and 5.0 M NaCl, pH 2.0). To ensure mutual comparability, we chose the same C_s value that was used in the benchmarking literature for the OER [13].

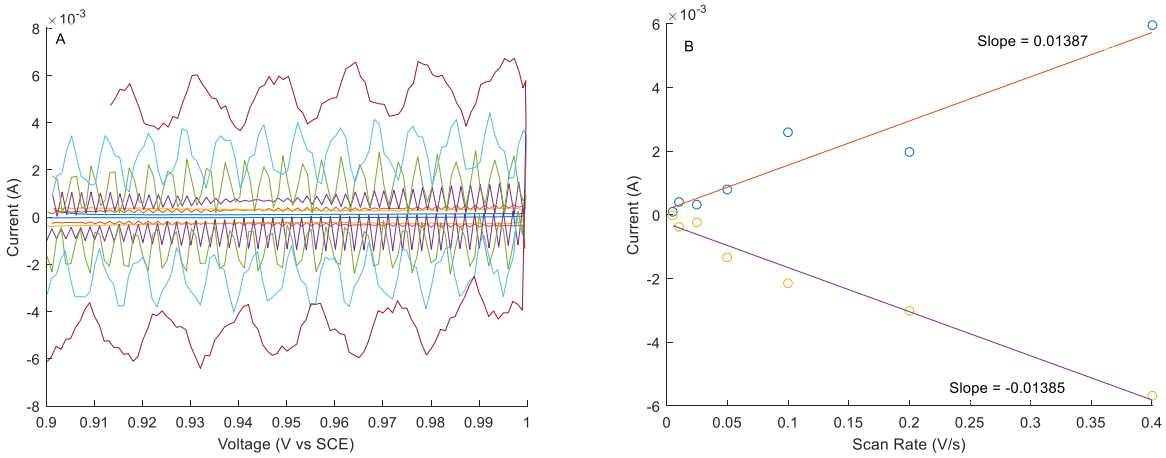

Fig. S9. Example double-layer capicitance measurements for determining ECSA for IrO_2 with 10 cycles of ALD TiO_2 in 1.0 M H_2SO_4. (Left) Cyclic voltamogramms in the non-Faradaic region at 0.005, 0.01, 0.025, 0.05, 0.1, 0.2, 04, and 0.8 V/s. (Right) Cathodic (yellow disks) and anodic (blue disks) charging currents measured at 0.95 V vs SCE plotted as a function of scan rate.

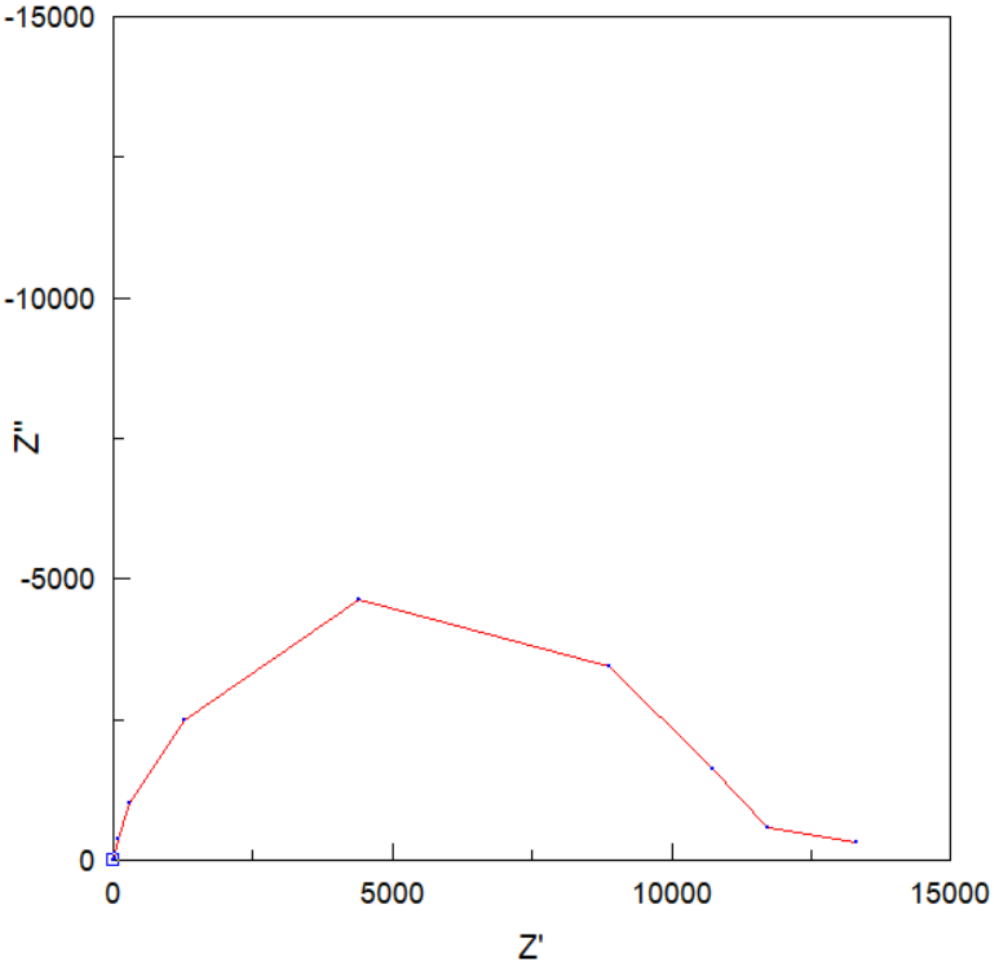

Fig. S10. Example impedence spectroscopy for IrO_2 with 0 cycles of ALD TiO_2 in 5.0 M NaCl pH 2.0 at E_{oc}. These data were fit to a resistor in series with a parallel combination of a capacitor and a shunt resistor. The resulting capacitance was taken as the C_d which in this case was was 3.24×10^{-6} F.

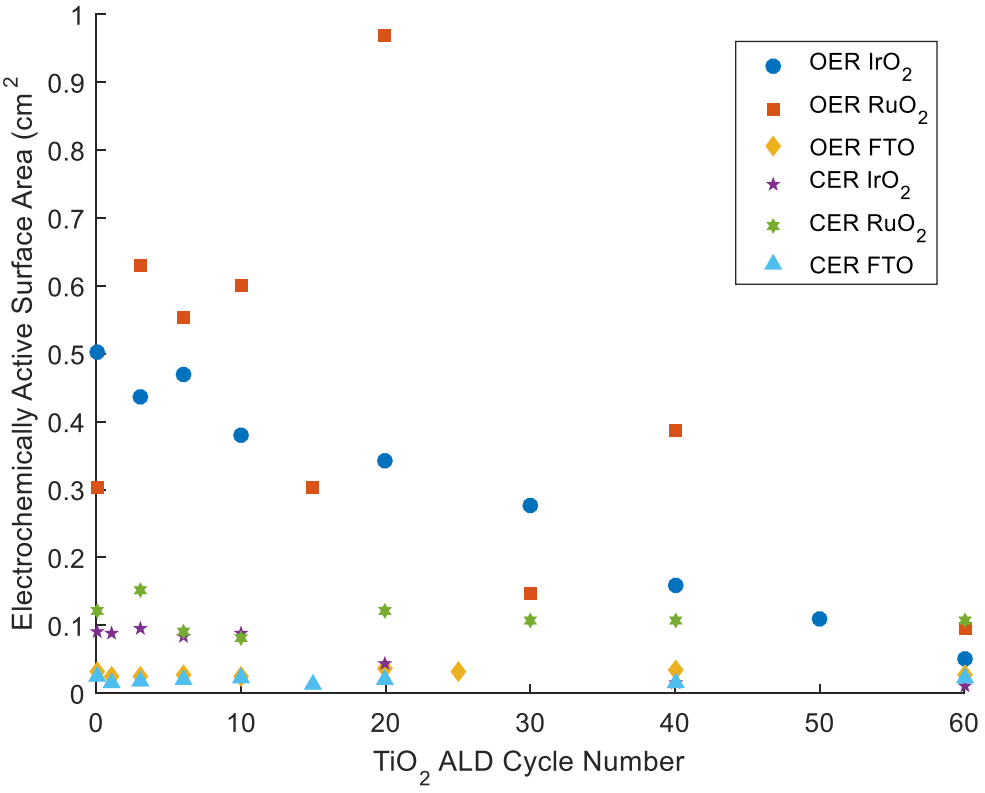

Fig. S11. ECSA for IrO_2, RuO_2, and FTO based catalysts in 1.0 M H_2SO_4 and 5.0 M NaCl, pH 2.0. All catalysts presented here had a geometric surface area of 0.13 cm^2, yielding electrochemical roughness factors between 0.1 and 6.0.

Calculating Specific Activities Using ECSA and AFM

As discussed in detail in prevous reports, reporting overpotential data relative to geometric current density can be misleading because geometric overpotentials can be influenced both by the roughness and the intrinsic activty of the catalyst [11, 12]. Specific activities (Fig. 1 of main text) were calculated as previously described, by normalizing the current from cyclic voltamagrams to the electrochemically active surface area [13]. For RuO_2 and IrO_2 based catalysts, specific activities were calculated at 350 mV overpotential for the OER, and at 150 mV overpotential for the CER. For FTO, specific activities were calculated at 900 mV overpotential for the OER, and at 700 mV vs NHE for the CER.

Alteratively, specific activities were calculated by normalizing the measured current density to the topographic surface area measured by atomic force microscopy (AFM; see AFM section) for direct comparison with catalysts reported by Seitz et al [12]. Roughness factors for these calculations are reported in Table S1.

Tafel Analysis

Tafel data is shown in Fig. S12 below. IrO_2 + ALD TiO_2 catalysts is from this work and tafel data for $SrIrO_3$ catalyts is from previous work. Current density is shown for surface area as measured by AFM.

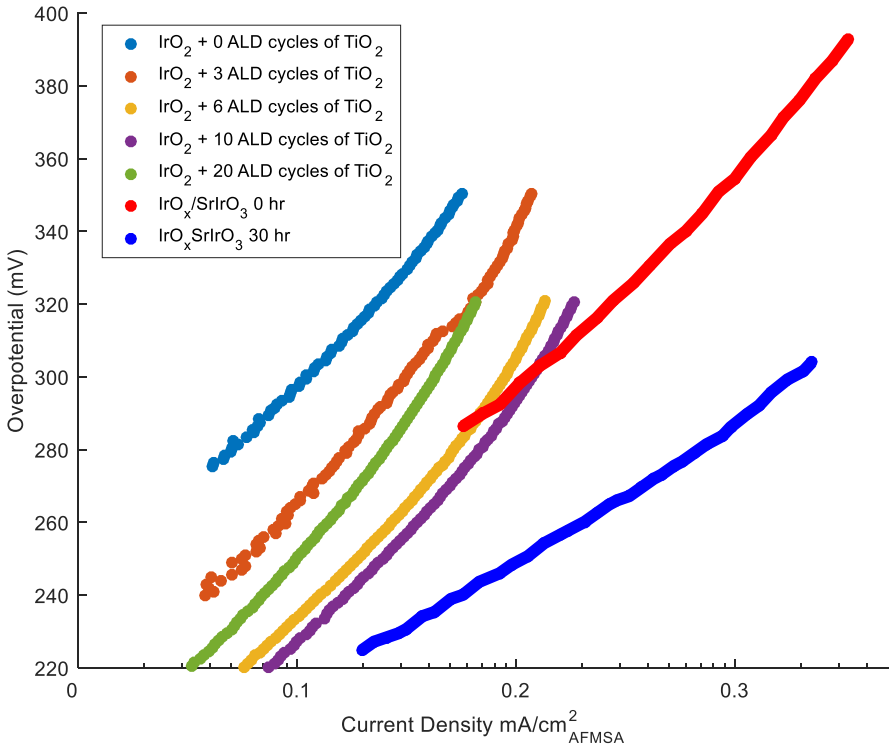

Fig. S12. Tafel plots from IrO_2 coated with 0 (dark blue), 3 (orange), 6 (yellow), 10 (purple), and 20 (green) ALD cycles of TiO_2 all from this work are shown next to those of $IrO_x/SrIrO_3$ at 0 (red) and 30 (light blue) hrs of activation as taken from literature [12]. To calculate the current density, the surfcae area was measured by AFM (table S1).

Table S4. A summary of the Tafel slopes and exchange current densities from this work (IrO_2 + TiO_2 catalyts) and previous work ($SrIrO_3$ catalysts) [12]. All current density data reported here is based on surfcae area that is measured by AFM (Table S1).

Catalyst	i_0 (mA/cm^2_{AFMSA})	slope ($mV/mA/cm^2_{AFMSA}$ decade)
IrO_2 + 0 ALD cycles of TiO_2	1.0×10^{-7}	59
IrO_2 + 3 ALD cycles of TiO_2	8.0×10^{-6}	65
IrO_2 + 6 ALD cycles of TiO_2	2.0×10^{-5}	64
IrO_2 + 10 ALD cycles of TiO_2	2.0×10^{-5}	61
IrO_2 + 20 ALD cycles of TiO_2	8.0×10^{-6}	61
$IrO_x/SrIrO_3$ 0 h	7.0×10^{-6}	57
$IrO_x/SrIrO_3$ 30 h	3.0×10^{-7}	38

Determination of E_{ZC} by Electrochemical Impedance Spectroscopy

To ensure high capacitance values, 5.0 M $NaNO_3$ at pH 2.0 was prepared by dissolving $NaNO_3$ (J.T. Baker, Center Valley, PA, 99.6%, used as received) in 900 mL of water (18 MΩ cm, Millipore, Billerica, MA), adjusting the pH using HNO_3 (Sigma Aldrich, ≥ 60%, used as received), and diluting with water to 1 L. Working electrodes were prepared as described above. A working electrode, an SCE reference electrode (CH instruments), a coiled platinum wire counter electrode (Sigma Aldrich), and 20 mL of $NaNO_3$ solution were added to a 25 mL 4 neck 14/20 round bottom flask reactor. The reactor was gently bubbled with N_2 for at least 15 min before experiments, as well as during experiments. The impedance was measured using a Bio-Logic potentiostat/galvanostat model VSP-300 with EIS capability. All studies were performed at 25 ± 2 °C. Impedance spectra were recorded in the frequency range of 1 MHz to 10 mHz, with a modulation amplitude of 5 mV. An initial potential range of 1.1 to 0 V vs SCE, with a step size of 25 mV, was performed to identify the E_{ZC} region. A narrower potential range (typically ± 200 mV around the apparent E_{ZC}) was then used to measure the E_{ZC} value.

EIS data were fit as described previously, using *ZView* software, to an R_s-(R_p-C) circuit, where R_s is solution resistance at high frequencies, *C* is capacitor that represents double-layer capacitance in mid-range frequencies, and R_p is charge transfer resistance at low frequencies (Figs. S13 and S14) [20].

As previously reported, for FTO, IrO_2, and RuO_2 the capacitance values extracted from impedance spectroscopy are expected to approximate a traditional double layer capacitance (C_{DL}) to first order [21, 22]. For samples with partial, semi-continuous and continuous TiO_2 coatings (Fig. S1-3), the TiO_2 layers are so thin for reasonably active catalysts (< 1.95 nm or 30 ALD cycles of TiO_2), the TiO_2 is assumed to be fully carrier-depleted within the potentials in question, so the changes in C_{DL} measured by impedance may be used to approximate a traditional E_{ZC}.

To confirm this assumption, Mott-Schottky analysis of the capacitance data was performed for the various samples. For an equivalent circuit comprising a series resistor combined with a parallel combination of a capacitor (*C*) and a shunt resistance, the inverse of the square of the capacitance (Farads) taken from the fit of the full frequency range on the nyquist plots was plotted against the potential with respect to NHE, E_{NHE}. For the low-cycle numbers of ALD TiO_2 on the substrates, a local maximum was observed, corresponding to the local minimum of *Q* vs $E_{NHE,}$ and thus the E_{ZC}. However, for samples in which 100 or 1000 cycles of ALD TiO_2 were deposited, corresponding to ~6.5 and ~65 nm respectively, a linear plot from Q^{-2} vs E_{NHE} was obtained. These plots were analyzed through application of the Mott-Schottky equation (Eq. S2), where ε_0 is the permittivity of free space, ε is the specific permittivity of TiO_2, *A* is the area of the electrode, *q* is the (unsigned) charge on an electron, N_d is the dopant density, V_{fb} is the flat band potential, k_b is the Boltzmann constant, *T* is temperature, and *V* is the applied potential, and *C* is the capacitance.

$$\frac{1}{C^2} = \frac{2}{\varepsilon\varepsilon_0 A^2 q N_d}\left(V - V_{fb} - \frac{k_b T}{q}\right) \qquad \text{Eq. S2}$$

From the 500 and 1000 TiO_2 ALD cycle samples, a value of N_d = (8.1 ± 4.2) X 10^{19} cm^{-3} was found, and the flat-band potential for the TiO_2, V_{fb}, was calculated to be 282 ± 15 mV positive of NHE. From these parameters, in conjunction with Eq. S3 and at an applied potential of 0.25 V vs NHE (the lowest E_{ZC} value), the TiO_2 in question would have a depletion width of 7.3 ± 1.4 nm, which is substantially higher than the actual thickness of TiO_2 present in any of the catalytically relevant samples analyzed here (< 60 TiO_2 ALD cycles, or less than 3.9 nm).

$$W = \sqrt{\frac{2\varepsilon\varepsilon_0 V_{bi}}{qN_d}}$$

Eq. S3

Within the framework of this analysis, the TiO_2 film deposited on the substrates is under full depletion throughout the course of these experiments, and the capacitive effects from this film may therefore be ignored when the potential of zero charge is calculated by impedance spectroscopy.

Because E_{ZC} is believed to be a fundamental property of a material, changing the electrolyte may change the absolute value of the E_{ZC}, but should not change the trend in the values of materials measured in the same electrolyte [23].

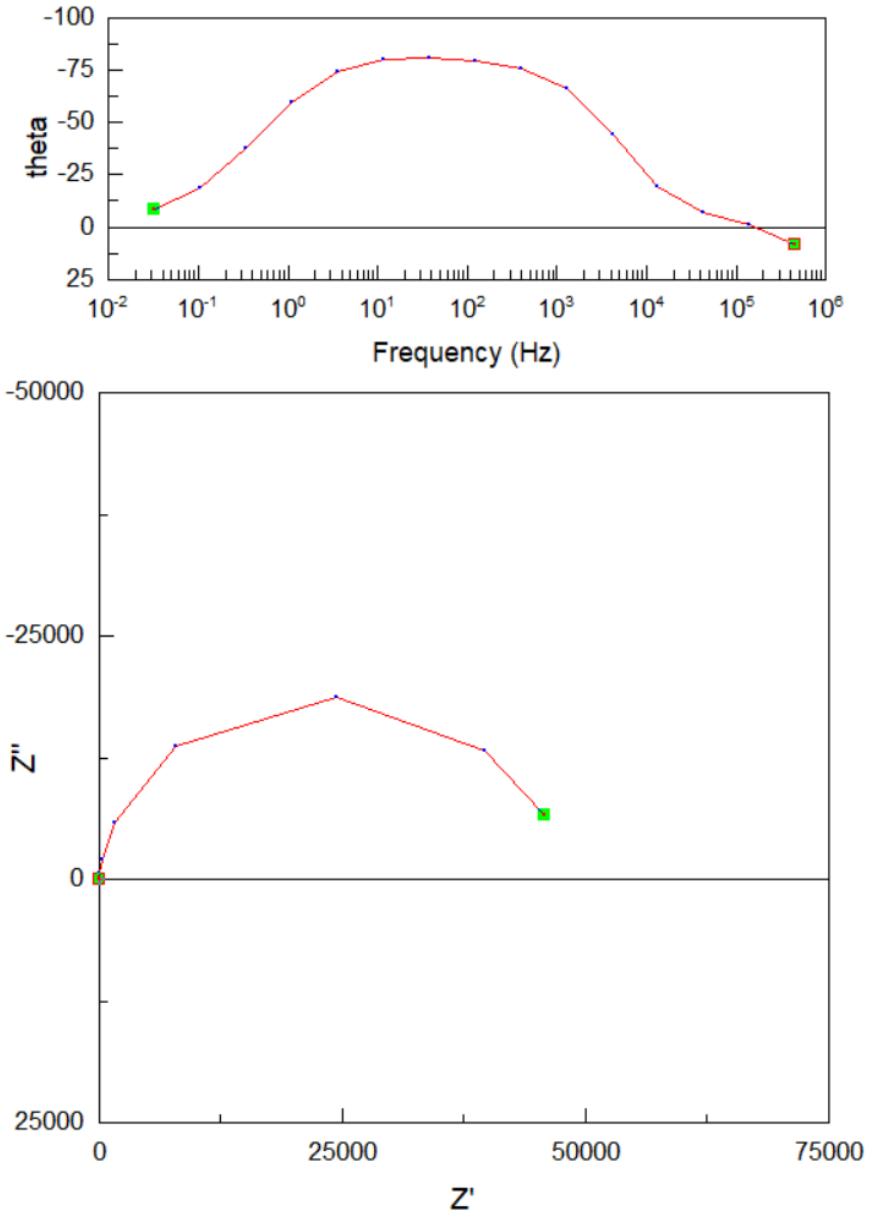

Fig. S13. Sample Bode (above) and Nyquist (below) plots of electrochemical impedence spectroscopy data of IrO_2 coated with 10 ALD cycles of TiO_2. The Bode plot shows the frequency of the alternating current signal (Hz) versus the phase shift of the impedance response (degrees). The Nyquist plot shows the real (*Z*') and imaginary (*Z*") components of the impedance response to the alternating current signal. Data presented in the figure were collected at 105 mV vs SCE in 5.0 M $NaNO_3$ at pH 2.0. The resulting equivelent circuit [R_s-(R_p-*C*)] fit of these data yielded a capacitance of 5.8×10^{-6} F.

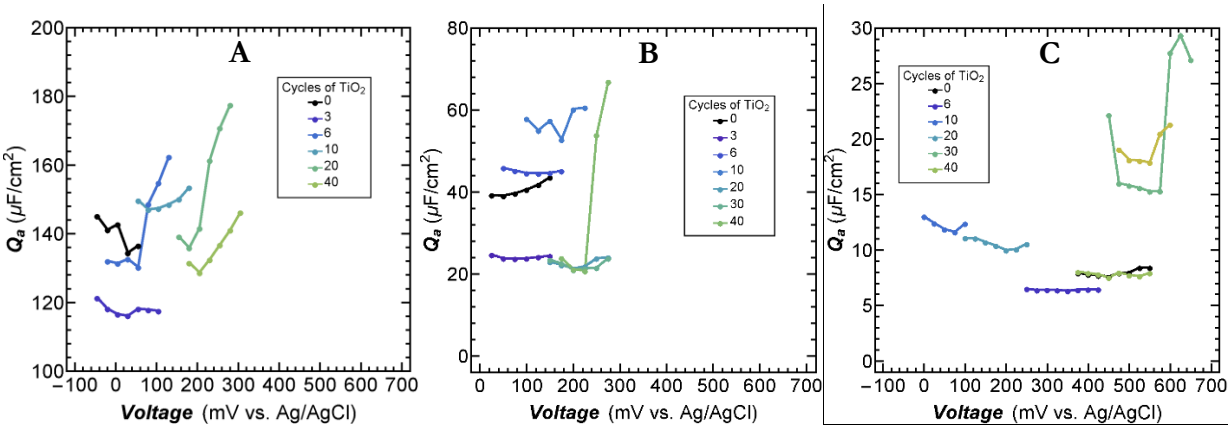

Fig. S14. Electrochemical impedance spectroscopy of (A) IrO_2, (B) RuO_2, (C) and FTO coated with various ALD cycles of TiO_2 at 25 mV intervals in 5.0 M $NaNO_3$ at pH 2.0. The resulting Nyquist plots were modeled as R_s-(C-R_p) circuits. The calculated capacitance values (dots) for each sample (set of dots) are shown here. The minimum value of each curve represents the E_{ZC}. The magnitude of the capacitance represents the surface area of the sample.

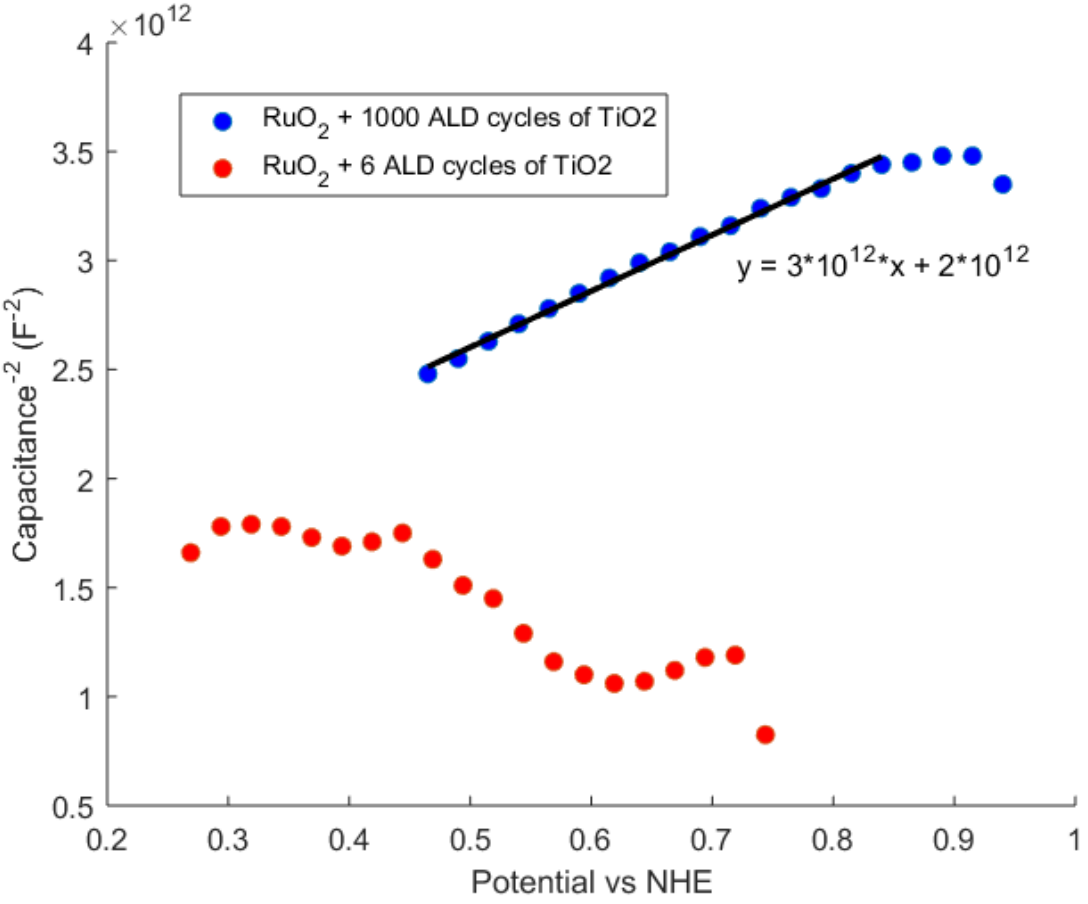

Fig. S15. Sample Mott-Schottky (E vs $1/C^2$) plots of RuO_2 with 0 (red), 1000 (blue) ALD TiO_2 cycles. The fit, using a geometric surface area of 7.1 X 10^{-6} m^2, yielded N_d = of 5.4 X 10^{19} cm^{-3}.

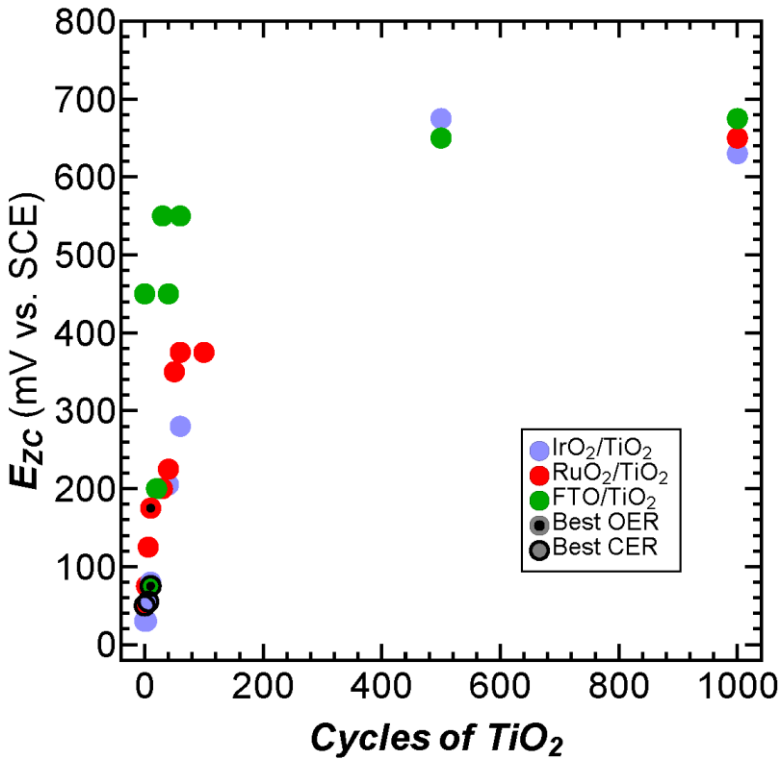

Fig. S16. Potential of zero charge as a function of TiO_2 cycle number for IrO_2, RuO_2, and FTO electrocatalysts. Black dots and disks with black borders indicate the catalysts with the highest specific activity for each substrate for the OER and CER, respectively.

For thick (>100 cycles) ALD TiO_2 films, the E_{ZC} values converged, indicating that all surfaces were electronically similar, bulk TiO_2. For The CER, the most active catalysts had E_{ZC} values of ~55, ~50, and ~75 mV vs SCE (IrO_2 + 3 ALD TiO_2 cycles, RuO_2 + 0 ALD TiO_2 cycles, and FTO + 10 ALD TiO_2 cycles respectively) and for the OER the optimal E_{ZC} was ~80, ~175, and ~75 mV vs SCE (IrO_2 + 10 ALD TiO_2 cycles, RuO_2 + 10 ALD TiO_2 cycles, and FTO + 10 ALD TiO_2 cycles respectively) (Figs. 3 and S16).

X-ray Photoelectron Spectroscopy

Data Collection and Peak Fitting

X-ray photoelectron spectroscopy (XPS) data were collected using a Kratos AXIS Ultra spectrometer (Kratos Analytical, Manchester, UK) equipped with a hybrid magnetic and electrostatic electron lens system, a delay-line detector (DLD), and a monochromatic Al K□ ± X-ray source (1486.7 eV). Data were collected at pressures of ~2 x 10^{-9} Torr with photoelectrons collected along the sample surface normal. The analyzer pass energy was 80 eV for survey spectra and 10 eV for high-resolution spectra, which were collected at a resolution of 50 meV. The instrument energy scale and work function were calibrated using clean Au, Ag, and Cu standards. The instrument was operated by Vision Manager software v. 2.2.10 revision 5.

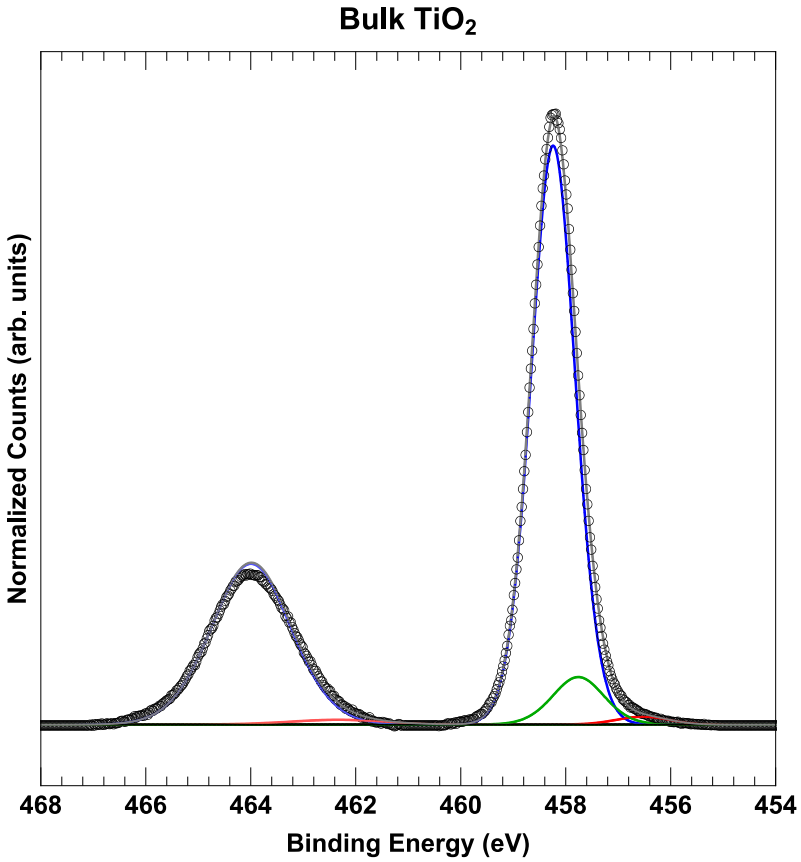

Fig. S17. X-ray photoelectron spectroscopy of the Ti 2p region for a bulk TiO_2 film. The peak associated with Ti^{4+} is shown in blue. The slightly and highly reduced Ti peaks are shown in green and red, respectively, and the most highly oxidized Ti peak is shown in orange.

XPS data were analyzed using CasaXPS software (CASA Software Ltd). The Ti 2p core-level photoemission spectra were fit constraining the peak separation and the peak area ratio between Ti $2p^{3/2}$ and Ti $2p^{1/2}$ peaks to 5.75 eV and 2:1, respectively. The peak area ratios were allowed to deviate 5% from the 2:1 ratio to account for inaccuracies in the background. All peaks were fit using a Gaussian-Lorentzian with 30% Lorentzian character. A bulk TiO_2 sample (1000 cycles) was used as a standard to determine the peak positions for the Ti $2p_{3/2}$ core-level photoemission (Fig. S17). The bulk TiO_2 sample fit exhibited a main peak at 458.24 eV , which is consistent with reports of the peak position for TiO_2 and therefore was ascribed to the Ti^{4+} oxidation state, and two additional peaks at lower binding energies, 457.6 eV and 456.6 eV, respectively, associated with a more reduced Ti state, likely Ti^{3+}[24-27]. These peaks were propagated through for IrO_2 for all thicknesses of TiO_2. In addition to these peaks, a fourth peak at slightly higher binding energy (458.5 eV) was needed to fit the FTO spectra.

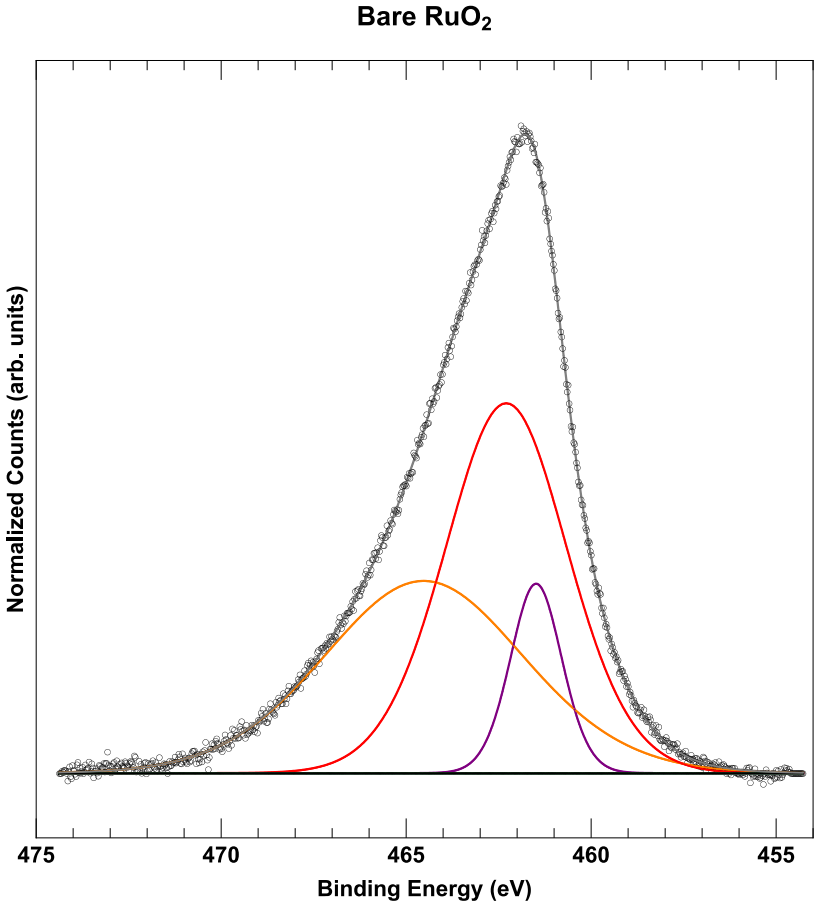

Fig. S18. X-ray photoelectron spectroscopy of the Ti 2p region for a bare RuO_2 film. The 3 orange, red, and purple peaks define the Ru 3p core level photoemission associated with RuO_2.

In the case of RuO_2, the Ru 3p core level exhibited a broad peak in the Ti 2p region (Fig. S18), which was well-fit by 3 Gaussian-Lorentzian peaks at 461.5 eV, 462.3 eV, and 464.5 eV, respectively. These Ru 3p core level photoemission peaks were propagated through for the fits of the spectra with ALD TiO_2. In addition to the 3 peaks associated with the Ru 3p core level, the spectra were also fit with the 3 peaks associated with bulk TiO_2, as described above. To deconvolute the effect of Ru 3p core level photoemission from the TiO_2 signal, the Ru 3p core level peaks were subtracted from the spectra resulting in spectra corresponding purely to the Ti 2p core level photoemission.

The photoemission from the underlying metal oxide substrates was also measured. Peak fitting was performed on the bare metal oxide substrate and then propagated through to the spectra with ALD TiO_2. The Ir 4f and Ru 3d photoemission core-level spectra were fit according to previous reports in the literature [28, 29]

Ti 2p Core-level Photoemission

The full Ti 2p core-level photoemission region is shown in Fig. S19, stacked from bottom to top for increasing TiO_2 cycle number. Depositing low cycle numbers of ALD TiO_2 on IrO_2 and RuO_2 produced Ti core-level spectra containing lower binding-energy signatures than the bulk TiO_2 film, which we ascribe to mixed oxides in which the Ti is in a more reduced form, likely a Ti^{+3} oxidation state. The Ti oxidation state for these samples gradually increased to its bulk oxidation state (~+4) as cycle number increased and bulk TiO_2 was observed (Fig. 4). In the case of ALD TiO_2 on FTO, a different trend was observed in which the lower cycle number thicknesses produced spectroscopic signatures with binding energies primarily at the bulk position as well as a higher binding-energy peak. We ascribe this added peak to a mixed phase between the substrate (FTO) and the thin TiO_2 film, but one in which the chemical nature of the phase produces a seemingly more electron-poor film, and where the mixed phase is likely Ti^{4+}. The variation in oxidation state of the Ti species with

TiO_2 thickness is accompanied by a shift in the overall Ti $2p_{3/2}$ peak position relative to a bulk (1000 cycles) TiO_2 film for IrO_2 and RuO_2 while the shift in the FTO peak position is less substantial and opposite in sign (Fig. S20).

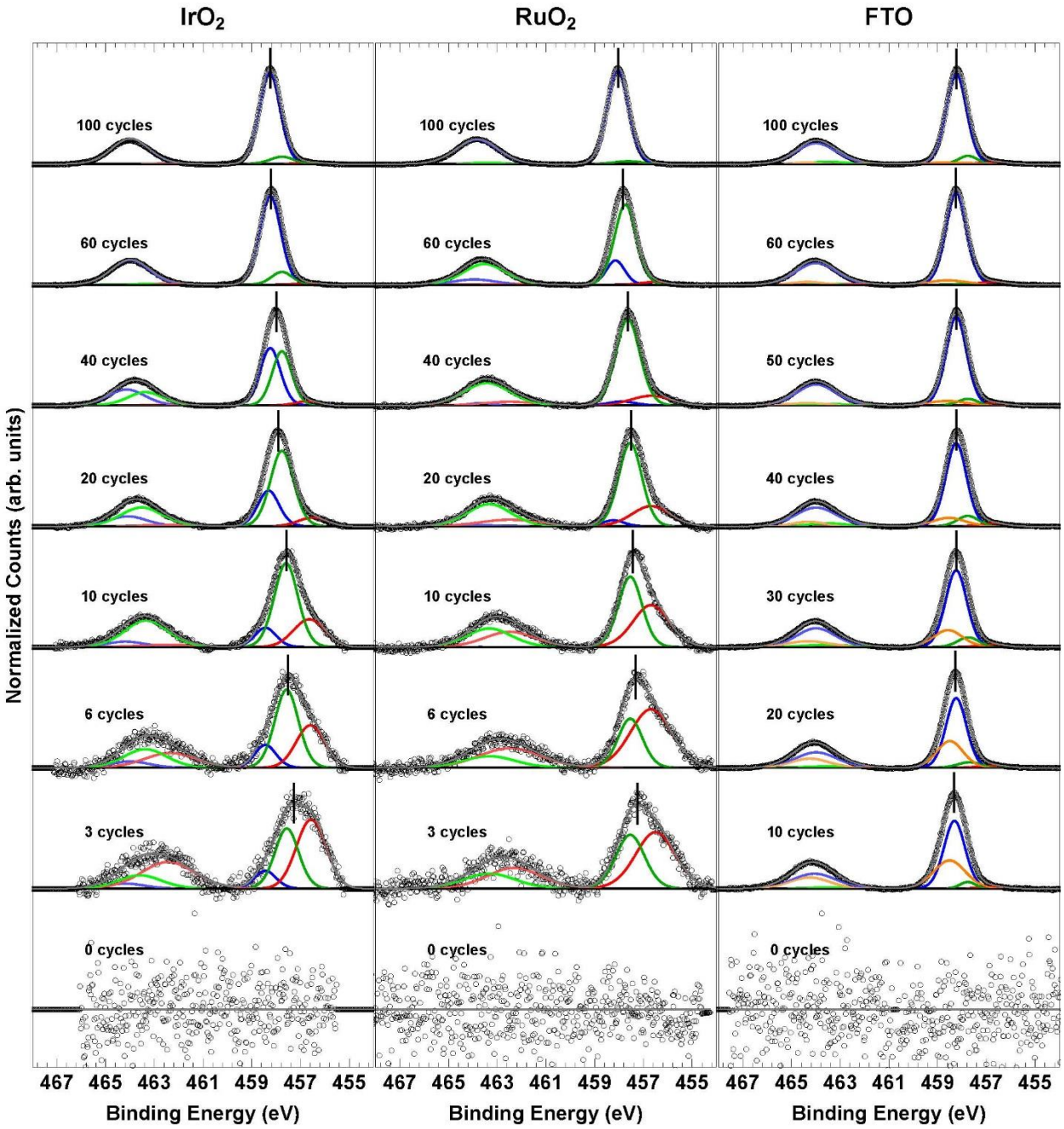

Fig. S19. X-ray photoelectron spectroscopy of the Ti 2p region for IrO_2, RuO_2, and FTO catalysts. Bulk TiO_2 is shown as the blue peak in each spectrum. The slightly and highly reduced Ti peaks are shown in green and red, respectively, and the most highly oxidized Ti peak is shown in orange.

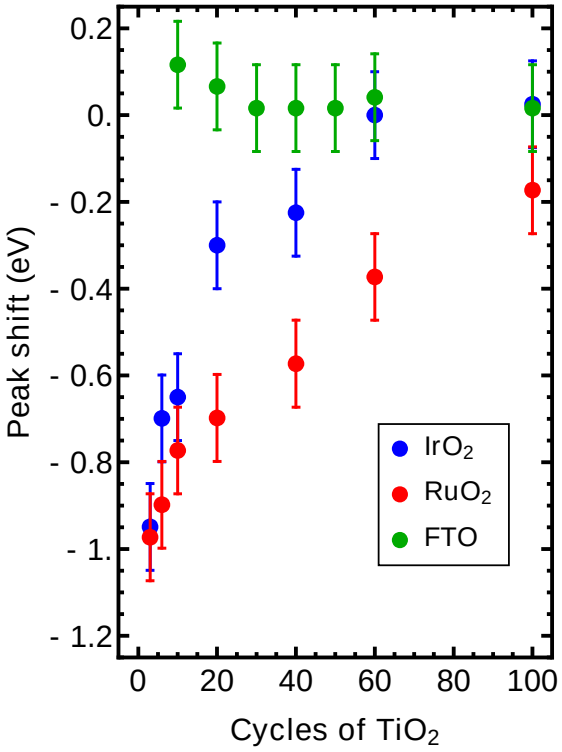

Fig. S20. Ti $2p_{3/2}$ overall peak shift relative to bulk TiO_2 as a function of TiO_2 cycle thickness for IrO_2, RuO_2, and FTO.

Underlying Metal Oxide Photoemission

The Ir 4f, Ru 3d, and Sn 3d core-level photoemission for the IrO_2-, RuO_2, and FTO-based catalysts is shown in Fig. S21, stacked bottom to top for increasing TiO_2 thickness. The spectra are fit according to the methods as described above with the blue and red shaded peaks representing the main peak and its satellite peak, respectively. The areal ratio of the main to satellite peak is tabulated in Table S5 for each catalyst at different TiO_2 thicknesses, with larger ratios indicating a relatively more reduced metal species. Upon initial TiO_2 deposition (3 cycles) the main to satellite areal ratio for IrO_2 and RuO_2 decreases indicating a more oxidized metal state relative to that of the bare

substrate. In the case of FTO, deposition of 10 cycles of TiO_2 leads to a lower main to satellite peak ratio, indicating a slightly more reduced state relative to that of bare FTO. However, there is no discernable trend in either main to satellite peak ratio nor in the peak shift (Fig. S22) and it is likely that changes in the oxidation state of the underlying metal oxide are beyond the detection limit of our measurements.

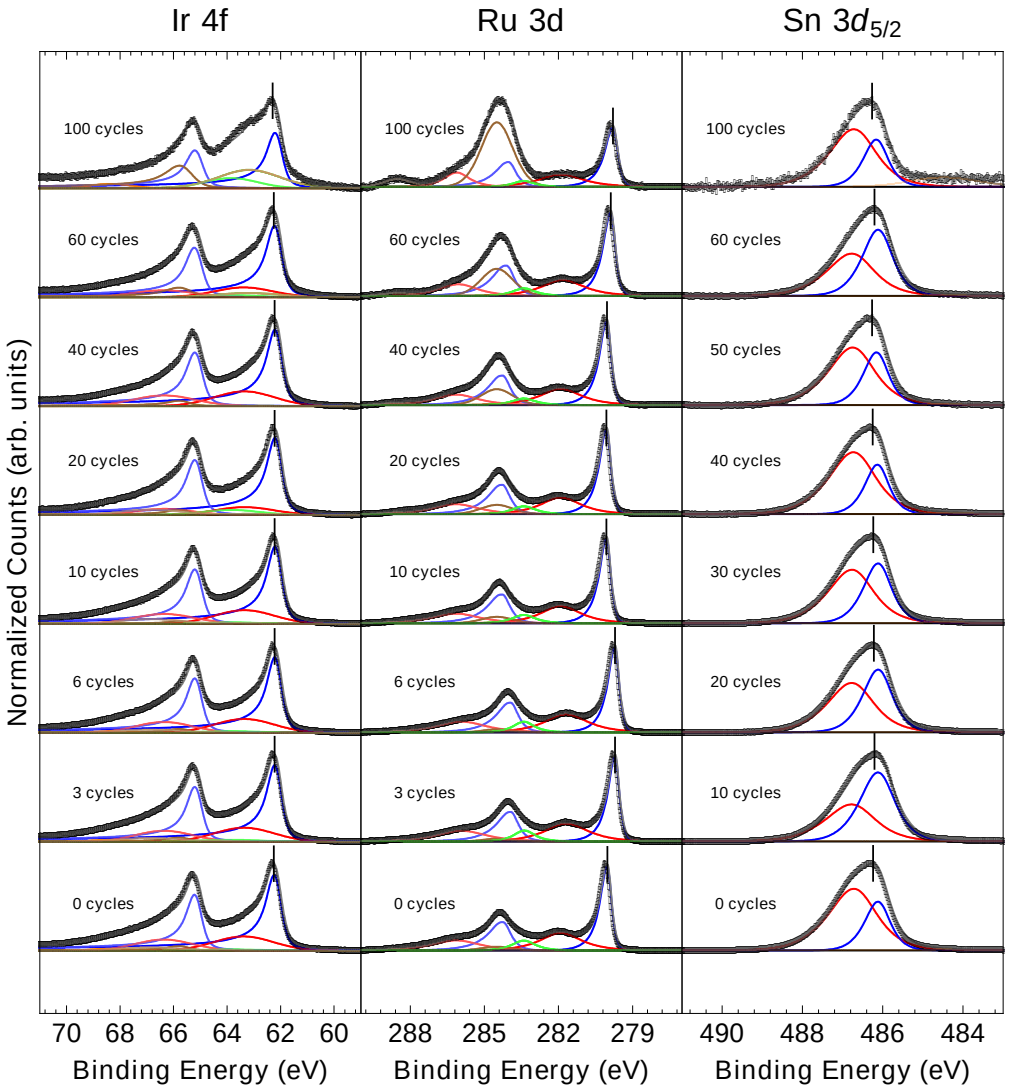

Fig. S21. X-ray photoelectron spectroscopy of the Ir 4f, Ru 3d, and Sn $3d_{5/2}$ region for IrO_2- RuO_2- and FTO-based electrocatalysts as a function of TiO_2 thickness.

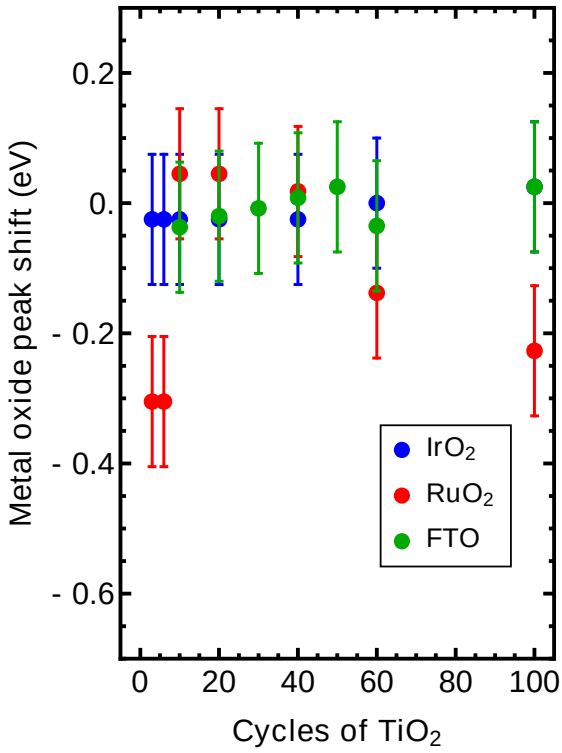

Fig. S22. Overall peak shift of the main peak of the Ir 4f, Ru 3d, and Sn $3d_{5/2}$ spectra relative to the bare metallic (0 cycle) metal-oxide substrate as a function of TiO_2 cycle thickness for IrO_2, RuO_2, and FTO, respectively.

Table S5. The areal peak ratios of the main peak to the satellite peak for the Ir 4f, Ru 3d, and Sn 3d core-level photoemission.

TiO_2 Cycles	Ir 4f	Ru 3d	Sn 3d
0	4.76	1.42	0.42
3	4.73	1.34	-
6	4.7	1.33	-
10	4.95	1.51	1.30
20	8.78	1.58	0.81
30	-	-	0.69
40	4.65	1.59	0.41

50	-	-	0.50
60	6.86	1.62	1.01
100	∞	1.52	0.435

Electrocatalyst Stability

X-ray photoelectron spectra were taken before and after 24-hour stability testing to understand the longevity of the catalytic enhancement. Figure S23 shows XPS spectra of the Ti 2p core-level before and after testing for the catalysts with the lowest overpotential for the OER for each materials system, 10 cycles, 10 cycles, and 30 cycles of TiO_2 for IrO_2, RuO_2, and FTO, respectively. After testing, no Ti species was detectable for any of the electrocatalysts tested in this study, which correlates well with the loss in catalytic performance over the duration of the stability test. The peak in the Ti 2p region for RuO_2 after testing is due to the Ru 3p core-level peaks and not to species associated with TiO_2. XPS spectra were also collected after 24-hour stability tests of the electrodes for the CER. Unlike for the OER, all electrocatalysts (except for the FTO based catalysts, which performed similarly as for the OER) showed stable performance over the duration of the stability test. XPS spectra after testing indicate that TiO_2 films are still present. A representative XPS spectra of the Ti 2p region for a RuO_2-based electrocatalyst before and after stability testing for the CER is shown in Fig. S24.

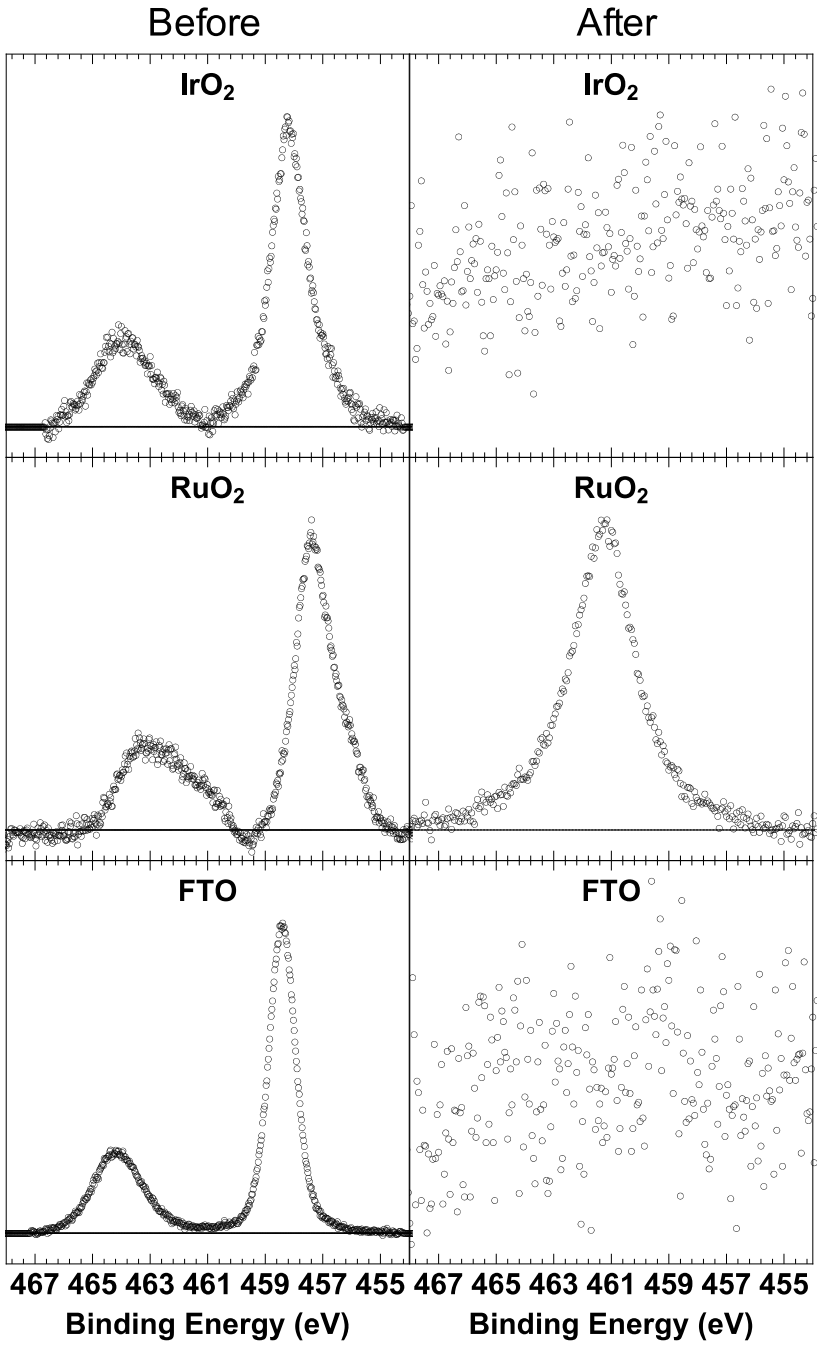

Fig. S23. X-ray photoelectron spectroscopy of the Ti 2p region for IrO_2, RuO_2, and FTO electrocatalysts with 10 cycles, 10 cycles, and 30 cycles of TiO_2, respectively, before and after stability testing for the OER. Note the peak still visible in the "after" RuO_2 spectra is associated with the Ru 3p core levels.

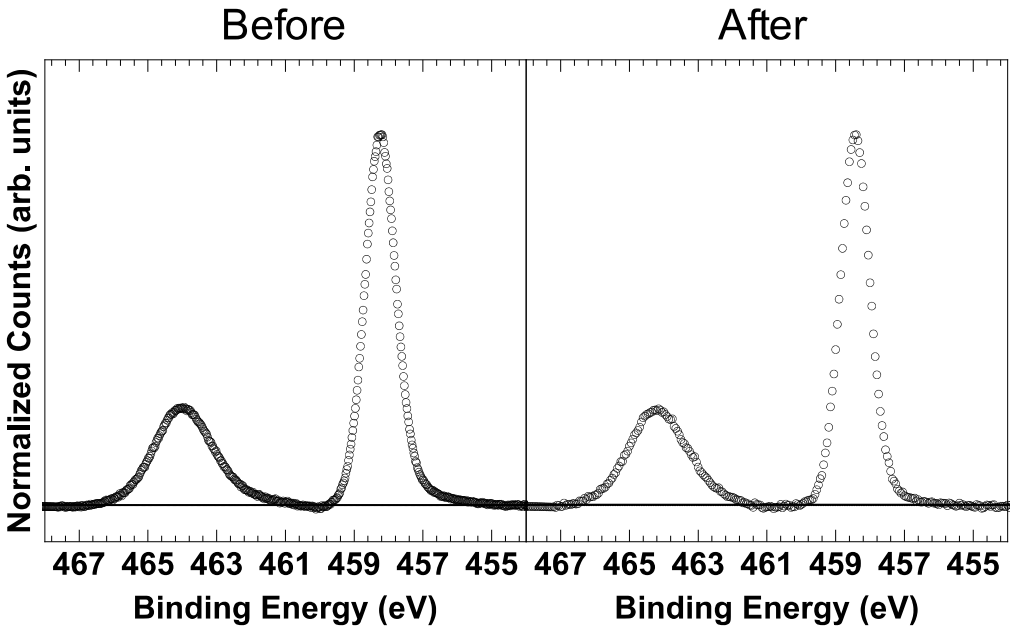

Fig. S24. X-ray photoelectron spectroscopy of the Ti 2p region for an RuO_2 electrocatalyst with 60 cycles of before and after 24-hour stability testing for the CER. The TiO_2 is still present after testing.

Notes and references:

1. B. R. Chalamala, Y. Wei, R. H. Reuss, S. Aggarwal, B. E. Gnade, R. Ramesh, J. M. Bernhard, E. D. Sosa and D. E. Golden, *Applied Physics Letters*, 1999, **74**, 1394-1396.
2. M. M. Jevtić, E. V. Jelenković, K. Y. Tong and G. K. H. Pang, *Thin Solid Films*, 2006, **496**, 214-220.
3. F. E. Akkad and S. Joseph, *Journal of Applied Physics*, 2012, **112**, 023501.
4. T. Uustare, J. Aarik, A. Aidla and V. Sammelselg, *Journal of Crystal Growth*, 1995, **148**, 268-275.
5. E. Verlage, S. Hu, R. Liu, R. J. R. Jones, K. Sun, C. Xiang, N. S. Lewis and H. A. Atwater, *Energy & Environmental Science*, 2015, **8**, 3166-3172.
6. R. T. Sanderson, *Journal of Chemical Education*, 1954, **31**, 2.
7. J. Noh, S. Back, J. Kim and Y. Jung, *Chemical Science*, 2018, **9**, 5152-5159.

8. L. R. Murphy, T. L. Meek, A. L. Allred and L. C. Allen, *The Journal of Physical Chemistry A*, 2000, **104**, 5867-5871.
9. J. B. Mann, T. L. Meek, E. T. Knight, J. F. Capitani and L. C. Allen, *Journal of the American Chemical Society*, 2000, **122**, 5132-5137.
10. L. C. Allen, *Journal of the American Chemical Society*, 1989, **111**, 9003-9014.
11. Z. W. Seh, J. Kibsgaard, C. F. Dickens, I. Chorkendorff, J. K. Nørskov and T. F. Jaramillo, *Science*, 2017, **355**, eaad4998.
12. L. C. Seitz, C. F. Dickens, K. Nishio, Y. Hikita, J. Montoya, A. Doyle, C. Kirk, A. Vojvodic, H. Y. Hwang, J. K. Norskov and T. F. Jaramillo, *Science*, 2016, **353**, 1011-1014.
13. C. C. L. McCrory, S. Jung, I. M. Ferrer, S. M. Chatman, J. C. Peters and T. F. Jaramillo, *Journal of the American Chemical Society*, 2015, **137**, 4347-4357.
14. C. E. Boman, *Acta Chem. Scand.*, 1970, **24**, 116-&.
15. A. A. Bolzan, C. Fong, B. J. Kennedy and C. J. Howard, *Acta Crystallogr. Sect. B-Struct. Commun.*, 1997, **53**, 373-380.
16. K. S. Pitzer and G. Mayorga, *The Journal of Physical Chemistry*, 1973, **77**, 2300-2308.
17. S. A. Angus, B; de Reuck, K M, *Chlorine: international thermodynamic tables of the fluid state*, Elsevier Science, Burlington, MA, 1985.
18. J. Jia, L. C. Seitz, J. D. Benck, Y. Huo, Y. Chen, J. W. D. Ng, T. Bilir, J. S. Harris and T. F. Jaramillo, *Nature Communications*, 2016, **7**, 13237.
19. American Public Health Association., American Water Works Association., Water Pollution Control Federation. and Water Environment Federation., *Journal*, 1960, volumes.
20. A. Łukomska and J. Sobkowski, *Journal of Electroanalytical Chemistry*, 2004, **567**, 95-102.
21. J. E. N. Swallow, B. A. D. Williamson, T. J. Whittles, M. Birkett, T. J. Featherstone, N. Peng, A. Abbott, M. Farnworth, K. J. Cheetham, P. Warren, D. O. Scanlon, V. R. Dhanak and T. D. Veal, *Advanced Functional Materials*, DOI: 10.1002/adfm.201701900, 1701900-n/a.
22. L. F. Mattheiss, *Physical Review B*, 1976, **13**, 2433-2450.

23. S. Trasatti, *Journal of Electroanalytical Chemistry and Interfacial Electrochemistry*, 1971, **33**, 351-378.
24. A. P. Dementjev, O. P. Ivanova, L. A. Vasilyev, A. V. Naumkin, D. M. Nemirovsky and D. Y. Shalaev, *J Vac Sci Technol A*, 1994, **12**, 423-425.
25. M. V. Kuznetsov, J. F. Zhuravlev and V. A. Gubanov, *J Electron Spectrosc*, 1992, **58**, 169-176.
26. F. Werfel and O. Brummer, *Phys Scripta*, 1983, **28**, 92-96.
27. D. Gonbeau, C. Guimon, G. Pfisterguillouzo, A. Levasseur, G. Meunier and R. Dormoy, *Surf Sci*, 1991, **254**, 81-89.
28. P. Verena, J. T. E., V. V. J. J., M. Cyriac, A. Rosa, T. Detre, G. Frank, S. Michael, G. M. T., A. Jasmin, H. Maike, W. Gisela, P. Simone, H. Michael, K. G. Axel and S. Robert, *Surface and Interface Analysis*, 2016, **48**, 261-273.
29. B. V. Crist, *Handbook of monochromatic XPS spectra*, Wiley, Chichester ; New York, 2000.

Chapter 4

An Economically Advantageous Method for Clean Hydrogen Production in the Present or Near-Term

Cody E. Finke, David Zheng, Fanfei Li, Michael R. Hoffmann, Neil A. Fromer

Abstract

Conventional hydrogen production primarily via Steam Methane Reforming is responsible for ~3% of global CO_2 emissions. Economic analyses of low-emissions hydrogen production processes (e.g. Water Electrolysis) find that they are too expensive at the industrial scale to be economically viable. This paper seeks to evaluate Sulfur Electrolysis, an electrochemical process to cogenerate clean hydrogen and sulfuric acid using realistic component pricing drawn from current market prices. We find that this process could generate up to 10% of global hydrogen demand for less cost and fewer CO_2 emissions than hydrogen produced via Steam Methane Reforming when powered by an average US grid. Solar-only Sulfur Electrolysis can be competitive with Steam Methane Reforming with relatively small improvements and has the potential to reduce annual, global CO_2 emissions by 120 Million Metric Tonnes. This, and other, cogeneration processes may be able to meet the global demand for hydrogen with reduced cost and CO_2 emissions.

Introduction

Hydrogen is the most consumed commodity chemical on the planet by mol (~25 teramoles/yr)[44]. It is used primarily for the production of ammonia and petrochemicals [44]. Currently, >95% of hydrogen is made from the thermochemical conversation of organic fuels. Hydrogen production is responsible for 1.5-3% of global CO_2 emissions annually, equal to 600 to 1,200 MMT[44]. The most common hydrogen production process, CO_2 intensive Steam Methane Reforming (SMR), may produce hydrogen for $1.15 per kg H_2[26].

There are several processes that produce carbon-free hydrogen, including Water Electrolysis (WE), the Hybrid Sulfur Cycle (HyS) and the Ferrite Cycle[45]. These processes have attracted considerable attention in academic communities as a potential source of clean hydrogen for energy storage[23]. However, with the exception of the electrochemical Chlor-Alkali Process (C-AP), most of these technologies have gained little traction as a method for industrial hydrogen production due to very

high estimated costs (generally >$4.00 per kg H_2). C-AP is able to bring down its cost by producing hydrogen as a byproduct of chlorine and caustic soda production, thus supplying around 3% of global hydrogen demand[20]. Propositions for carbon based strategies to make clean, cheap hydrogen include biomass gasification and methane pyrolysis. These methods produce hydrogen for an estimated $2.41 and $1.58 per kg H_2 respectively and may be considered more attractive options as they are closer to a competitive price point[26,46]. Methane pyrolysis (MP) cogenerates a solid carbon byproduct and could be cost competitive with SMR if the cogeneration carbon product could be sold at large scales (as is done with the C-AP)[47]. Unfortunately, the market for this carbon is currently small[47]. Ultimately, under current market conditions, both processes are more expensive than SMR and unlikely to be adopted by large-scale industries.

Cogeneration is a known method for reducing the cost of carbon-free hydrogen production (e.g. the C-AP)[20]. In the present analysis, we seek to apply this method by modeling the economics of an electrochemical process which cogenerates hydrogen and sulfuric acid (sulfur electrolysis; SE). We argue that cogeneration of hydrogen and sulfuric acid is advantageous for several reasons. The market size for sulfuric acid is >3X that of chlorine by mol (~3 teramoles sulfuric acid per year)[48] and at full scale, the SE process could supply >10% of global hydrogen demand. Additionally, cogeneration of these commodities may be especially valuable because sulfuric acid and hydrogen are most commonly co-consumed in a single fertilizer plant as raw materials necessary to make NPK fertilizer[49]. Co-consumption of the products indicates that cogeneration is a near-term feasible strategy that will not add prohibitively high transportation costs or require costly and new infrastructure.

The two primary steps involved in SE (see equations 1 and 2) have been investigated extensively because equation (1) is the first step in the Contact Process (CP; the standard thermochemical process to produce sulfuric acid)[50] and equation (2) is the electrochemical step in the HyS (a proposed combined electrochemical and thermochemical water splitting cycle)[51].

$$S_8 + 8O_2 \rightarrow 8SO_2 \quad (1)$$

$$SO_2 + 2H_2O \rightarrow H_2SO_4 + H_2 \quad (2)$$

In this techno-economic analysis, we create a model for sulfur electrolysis (SE) which uses only real prototype data and present day CapEx and OpEx estimates based on currently installed or produced plants and equipment. Additionally, our model optimizes plant design by tuning the operating

voltage and current density, size of solar installation, and the capacity factor. Our models estimate the energy consumption, CO_2 emissions, and levelized cost of hydrogen (LCH) production from SE. Cogeneration has shown to be a promising process to make clean hydrogen production cheaper than SMR. Given the projected urgency of reducing greenhouse gas emissions, we consider it imperative to create near term models to find economically efficient pathways to reduce CO_2 emissions from hydrogen production[2].

Methods

Assumptions of Levelized Cost of Hydrogen Model

The following section describes in detail the assumptions made in our SE model and comparative techno-economic analysis. Standard assumptions for our model are described in Table 1 and represent present day values of relevant parameters. In Table 1, we also present the high and low values that were assumed for the sensitivity analysis of the costs.

Table 1. **Sensitivity Analysis Parameters.**

Variable	Low Value	High Value	Standard Assumption
Inputs and Outputs			
H_2 Produced[a]	1,000	400,000	400,000
Buying Price of Sulfur[c]	-0.1	0.45	0.13
Selling Price of Sulfuric Acid[d]	0.05	0.33	0.143
Buying Price of Grid Electricity[e]	0.1	0.3	0.07
Selling Price of Grid Electricity[e]	0.005	0.18	0.01
Catalyst Parameters and Components			
SE[l] Catalyst Geometric Current Density[b]	0.33	1.5	1.21
WE[m] Catalyst Geometric Current Density[b]	0.33	1.5	1.48
Voltage Shift[g]	-1.0	1	0
Catalyst CapEx Cost Coefficient	0.1	10	1
Catalyst Lifetime[i]	1	21	7
Catalyst Faradic Efficiency Factor	0.1	10	1
PV Parameters and Components			

PV Nameplate Peak Power[f]	0.1	0.5	0.16
PV Balance of Systems Cost Coefficient	0.1	10	1
PV Module Cost Coefficient	0.1	10	1
Battery Components			
Battery Module Cost Coefficient	0.1	10	1
Battery Balance of Systems Cost Coefficient	0.01	10	1
Economic and Operating Parameters			
Capacity Factor	0.01	0.97	0.97
Rate of Return	0.05	0.20	0.12
Carbon Tax[j]	0	1	0.00
Carbon Intensity of Grid Electricity[k]	0	1	0.29
Initial Sulfuric Acid Concentration[h]	0.0	18.0	10.0
Electrolyzer Components			
Electrolyzer Balance of Systems Cost Coefficient	0.1	10	1
Electrolyzer Cost Coefficient	0.1	10	1

Note. [a] kg / dy [b] A / cm^2 [c] % / kg [d] $ / kg [e] $ / kWhr [f] kW / m^2 peak power [g] V [h] M [I]7 yrs [j] $ / kg CO_2. [k] Kg CO_2 / kg kWhr. [l] Sulfur Electrolysis. [m]Water Electrolysis.

For each system component, a sensitivity analysis was preformed where the model held all variables at the standard assumption except the sensitivity variable which was allowed to vary. The model then calculated the levelized cost of hydrogen at these values. Because it is impossible to know how easy it is to change each of these sensitivity parameters by a given amount, the magnitude of the sensitivity does not necessarily rank how important a given research objective is. Instead the sensitivity analysis indicates how much a given parameter would need to improve in order to make a meaningful improvement.

CapEx and OpEx assumptions associated with the hydrogen plant are summarized in Table 2. Assumptions for CapEx and OpEx associated with energy consumption and production are summarized in Table 3.

Model Description

We model a production plant which cogenerates hydrogen and sulfuric acid via a two-step process where sulfur is burned in air (equation 1) to produce SO_2. This is then dissolved in a mixture of water and sulfuric acid and electrochemically converted into hydrogen and sulfuric acid (equation 2). A simplified plant scheme adapted from Weidner et al is shown in Fig. 1[51].

Our model defines OpEx and CapEx and takes a set of empirical data that represents allowed operational parameters and then calculates the cost of hydrogen given these inputs. Our model defines the CapEx for all plant components including the SO_2 generator, the electrolyzer, the AC/DC rectifier, the DC/DC converter, batteries, photovoltaics, the H_2SO_4 concentrator, the compressor, and the balance of systems (e.g. land, wiring, and installation labor). A plant level box-diagram is shown in fig. 1. The model assumes a given price for the all of the OpEx including routine maintenance, major maintenance, labor, and raw materials (e.g. sulfur, water, and electricity). The model assumes that operational parameters (e.g. operating voltage, current density, and faradaic efficiency) and CapEx at various plant sizes are governed by a set of empirical rules. As in the H2A model, electrochemical components scale stepwise in 500 kg H_2/day steps.[26] Other active systems (e.g. SO_2 generator and sulfuric acid concentrator) scale non-linearly according to empirical data from these systems in the real world (see sections below). The electrolyzer's operational parameters are governed by demonstrated experimental evidence (see sections below). The model can vary any of the parameters from table 1 and calculate the levelized cost of hydrogen given the set of inputs applied to the physical data. At all times, the model can vary the capacity factor, amount of batteries, and degree to which solar energy is used to power the system but will always choose the cheapest combination of energy resources. The model can vary as many as two parameters in a given run. The full list of operational parameters are shown in table 1 with a detailed description of the physical rules that dictate these parameters in supplemental materials.

<u>SO_2 Generator</u>

In the CP, burning sulfur produces SO_2 and pressurized steam which is used to heat the downstream SO_3 generation reactor. Additional pressurized steam is produced when the SO_3 is hydrated to

produce oleaum and eventually sulfuric acid. This heat is used to export as much as 0.2 kWhr electricity per kg of sulfuric acid[52]. In SE, the heat generated from burning sulfur (equation 2) is also turned into pressurized steam used to produce electricity to power the electrochemistry. Our model assumes that 30% of the heat produced from sulfur burning could be used as electricity. Waste heat is used to warm the electrochemical reactor. In order to ensure a conservative estimate, we equated the capital expenditure (CapEx) of our sulfur furnace and turbine to the CapEx of an entire CP plant (see Figure S1 and equation S1 for details)[50]. Under standard assumptions (see Table 1), as much as 23 kWhr per kg of H_2 were provided by burning sulfur.

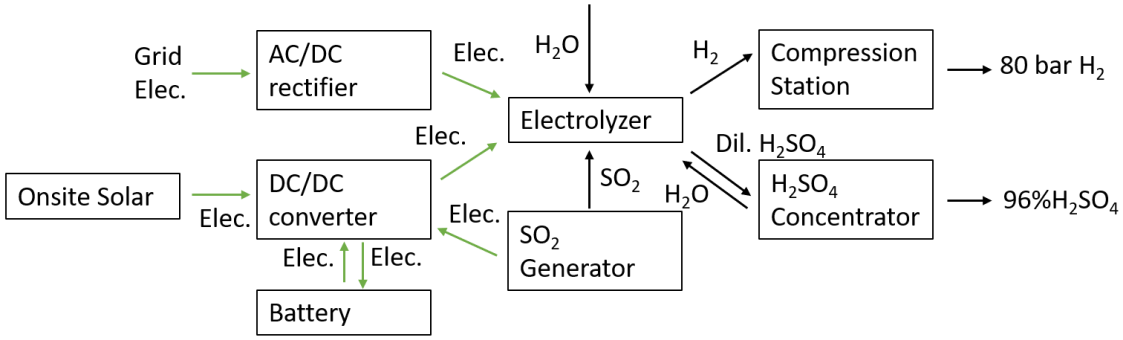

Figure 1: A simplified reactor scheme adapted from Weidner et al[51]. Sulfur is burned in air and the resulting SO_2 is dissolved in water where it is used in the anodic chamber of the electrolyte to cogenerate hydrogen and sulfuric acid. The sulfuric acid may be concentrated before use.

Sulfur Depolarization Electrolyzer

Our model assumes that sulfuric acid and hydrogen were cogenerated in a Sulfur Depolarization Electrolyzer (SDE) with currently demonstrated voltage, current, and faradaic efficiency relationships[51,53]. Most industrial applications require 70 to 98 mass percent (10.5 to 18 M) sulfuric acid. Studies have shown that modern Sulfur Depolarization Electrolyzers (SDE) can generate 70% sulfuric acid, however achieving higher concentrations requires novel engineering approaches or new membrane materials (see key technical challenges below and Figure S2-4, and equations S2-6, and Tables S1-2 for details)[53].

Our technoeconomic analysis models a plant that utilizes industrial scale SDEs. However, we are unaware of any industrial scale SDEs. As such, we modify recent overnight CapEx numbers for Proton Exchange Membrane (PEM) water electrolyzers from the National Renewable Energy Laboratory (NREL) H2A model[26]. The H2A model is an economic model of hydrogen production

costs. It takes current OpEx and CapEx data and estimates the LCH. Both PEM and SDE electrolyzers operate in acidic environments. Highly concentrated sulfuric acid is less corrosive than dilute sulfuric acid[54]. Therefore, we believe that the anti-corrosion measures for PEM electrolyzers should be sufficient for SDEs. The CapEx for electrolyzers in the H2A model assumes that each electrolyzer is capable of producing 500 kg H_2 per day and that the catalyst can reach a current density of 1.5 A/cm^2. It is likely that for a 500 kg H_2 per day electrolyzer that operates at a lower current density, the electrolyzer would need to be bigger and therefore more expensive. To estimate the cost of an SDE ($CapEx_{lyzer\_SE}$) from a PEM electrolyzer, the PEM electrolyzer CapEx ($CapEx_{lyzer\_WE}$) was multiplied by the ratio of the operating geometric current densities of the water electrolysis catalyst (j_{WE}) to the SDE catalyst (j_{SE}) (see equation 3). It is difficult for most SDEs to reach current densities higher than 1.2 A/cm^2 without significant voltage losses due to mass transport limitations [55]. Subsequently, equation (3) resulted in higher costs for SDEs than PEM electrolyzers, especially at high sulfuric acid concentrations where the dissolution of SO_2 is suppressed and the voltage increases due to concentration effects. We believe that using a linear relationship with current density represents a conservative estimate of variations in the cost of the electrolyzer, given that industrial equipment becomes non-linearly economically efficient as it scales up[56].

$$CapEx_{lyzer\_SE} = j_{WE}/j_{SE} \bullet CapEx_{lyzer\_WE} \quad (3)$$

Equation 3 also allows our model to tune the operating current density of the reaction because the relationship between voltage and current is non-linear such that energy consumption per kg H_2 decreases with decreasing voltage but the CapEx of the electrolyzer increases differently. Our model uses this relationship to determine the cheapest operating current density for the plant. Figure two shows calculated price of hydrogen for a variety of electrolyzer costs and operating current density, the lowest price of hydrogen for a given CapEx and current density represents the optimized operating condition (Fig. 2).

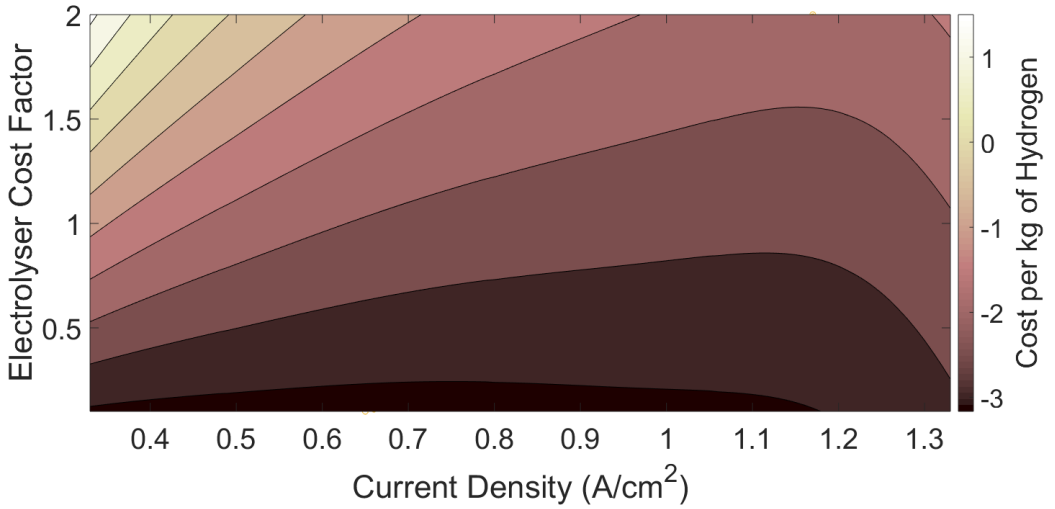

Figure 2: A heatmap of the price of hydrogen for several different operating current densities and electrolyzer CapEx costs. Electrolyzer cost factor is a unitless value which is the multiplication factor on the standard assumed price for an electrolyzer where 0.1 is 10X cheaper than a standard electrolyzer and 2 is 2X more expensive than a normal electrolyzer. Balance of system and catalyst costs per electrolyzer remained constant. Each electrolyzer cost factor corresponds to a different cheapest operating current density.

Sulfuric Acid Concentrator

Applications requiring > 70% sulfuric acid need it to be concentrated. To account for these cases, we model the costs associated with sulfuric acid concentration. We use real data from Sinopec Nanjing Chemical Industry Co. Ltd from a currently installed plant in Nanjing, China to add CapEx and operational and maintenance expenditure (OpEx) values for sulfuric acid concentration via combined vacuum concentration and spent acid regeneration processes (see supplemental information for full correspondence)[57]. Costs of raw materials, permitting, and labor are converted to US values to be consistent with the model.

Maintenance

As in the H2A model, we assume that maintenance requires replacement of 15% of installed CapEx every 7 years. Three percent of installed CapEx was added as annual OpEx to account for annual maintenance[26].

Table 2. Plant OpEx and CapEx data in 2018 USD.

CapEx	
Electrolyzer Size (in kg H_2/day)	500
Water Electrolyzer Cost[ab]	532
Sulfur Electrolyzer Cost (at 1.2 A/cm^2)[bc]	632
Electrolyzer Hard Balance of Systems[bc]	600
DCDC converter[bc]	471
Installation[bc]	136
Soft Balance of Systems[bc]	24
OpEx	
PEM Electrolyzer Electricity Consumption[d]	49
Balance of Systems Electrolyzer Energy Consumption[d]	5
Electricity from Sulfur Burning[d]	23
Sulfur Electrolyzer Energy Consumption[d]	33
Routine Maintenance (%)[e]	3
Major Maintenance (%)[f]	15

Note. [a]Reference case. [b]Amount in thousands of dollars. [c]Cost per electrolyzer. [d]Rate in kWhr/kg H_2. [e]Percent of installed capital per year. [f]Percent of installed capital per seven years.

Energy Sources

The energy consumption beyond what was provided by burning sulfur can be met with a combination of onsite solar, grid electricity, and onsite solar plus battery storage. Our model uses a slightly above US industrial average value of $0.07 per kWhr for grid electricity[58]. The model also allows for onsite solar to be installed using CapEx and OpEx data from 2014. Similar to previous electrolysis models, this model drew on three years of hourly resolved insolation data[59]. Each hour was spatially averaged across the entire contiguous United States (CONUS). While there was considerable seasonal variation, the average solar capacity factor was 20%[59]. The solar panels in this analysis were assumed to have a peak power rating of 160 W/m^2 with a 0.75% loss in efficiency per year of operation. If 100% of the electricity produced was used directly, the modeled levelized cost of energy (LCOE) from solar was found to be $0.052 per kWhr. The marginal cost of solar would increase if solar was installed so that the energy production outpaced the energy consumption at any point during the year.

In this analysis, excess solar energy could be stored in onsite lithium ion batteries. As in previous studies, batteries were rated to a constant annual discharge over a 12-year lifetime after which they would need to be replaced [60]. Costs associated with energy are presented in Table 3[60]. All battery costs assume a 0.5 kW max power output/kWhr energy storage[60]. The time of day or year that energy was needed could also be changed by increasing the number of electrolyzers and running them for less time per day or year (capacity factor). The capacity factor of the plant was allowed to vary between one and 97% of a year. The model optimized capacity factor, size of the solar installation, energy drawn from the grid, and energy stored in batteries. Under standard assumptions, 29% of energy needed was provided by solar while 71% was provided by the grid, no battery storage was used and solar panels were simply left at open circuit when they were overproducing. A solar-only case was also considered where 100% of energy was provided by solar and batteries. Under standard assumptions, it was cheaper to have a capacity factor of 97% and operate on battery based electricity than to decrease the capacity factor.

The CONUS spatial average introduces limitations because it includes places were solar panels can clearly not be utilized (e.g. National Parks). Additionally, highly sunny places like the US desert Southwest may allow for higher penetrations of solar and at a cheaper price of energy while more cloudy places like the east coast of the US may prove more expensive. To address these issues, we varied the cost and efficiency of solar in our sensitivity analysis below.

Table 3. CapEx and OpEx Associated with Energy.

Photovoltaics (PVs)[a]	
CapEx[b]	
Module[c]	0.31
Hard Balance of Systems[c]	0.22
Installation Cost[c]	0.12
Soft Balance of Systems	-
OpEx (per kWyr)[b]	17
Marginal LCOE[d] for First PV Panel[bc]	0.052
Batteries	

CapEx[b]	
Module[c]	180
Hard Balance of Systems[c]	60
Installation Cost[c]	27
Soft Balance of Systems[c]	33
OpEx (%)	69[e]
Marginal LCOE[d] *for First Battery*[bc]	0.21

Note. [a]Similar to other studies, it is assumed that PV could be placed on top of all structures and therefore no soft balance of systems would be associated with PV[21]. [b]Amount in US Dollars. [c]Amount per kW. [d]Levelized Cost of Energy. [e]Percentage of installed capital per 12 years.

Levelized Cost Calculation

Equation 4 calculates levelized costs using the following components: LC is the levelized cost (e.g. of hydrogen); product is the annual amount of product made (in kWhrs for batteries or PV and in kg for hydrogen or sulfuric acid); lifetime is the time the plant lasts before replacement in years; OpEx is annual operational expenditure; CapEx is the total capital expenditure of building a plant; r is the rate of return; and t is time in years. We assume a one year build time where no product was produced and that plant capacity reached the maximum capacity factor during the first year of operation. We also assume a rate of return of 12% as standard. This is higher than the H2A model which assumes 8% rate of return; however, unlike the H2A model, our model uses no taxes, deferred debt, or debt-based financing.

$$LC = \frac{CapEx + \sum_{t=2}^{lifetime+1} \frac{OpEx}{(1+r)^t}}{\sum_{t=2}^{lifetime+1} \frac{Product}{(1+r)^t}} \quad (4)$$

Consistent with our conservative assumptions, when we use SMR CapEx and OpEx numbers from the H2A model, our model estimates an LCH of $1.25 instead of $1.15.

CO_2 Emissions Analysis

The amount of produced CO_2 varies for electrochemical processes based on how that electricity is generated. For example, electricity generated from coal will have a larger carbon footprint than electricity from natural gas, which will have a larger footprint than solar. SMR emits around 9.28 kg

CO_2 / kg hydrogen[26]. This process is thermochemical with 59-83% of CO_2 being process CO_2 and the other 17-41% coming from the combustion of natural gas to heat the reaction chamber[24]. The full process requires around 35 kWhr/kg hydrogen and is net endergonic at the thermodynamic limit[61]. The net sulfur electrolysis process is spontaneous; heat harvested from burning sulfur can be captured and converted into electricity to run the SDE. While it is possible to run the plant only on burning sulfur, given that CapEx is high, it is cheaper to run the electrolyzer at very high current densities requiring additional energy input (figure 3).

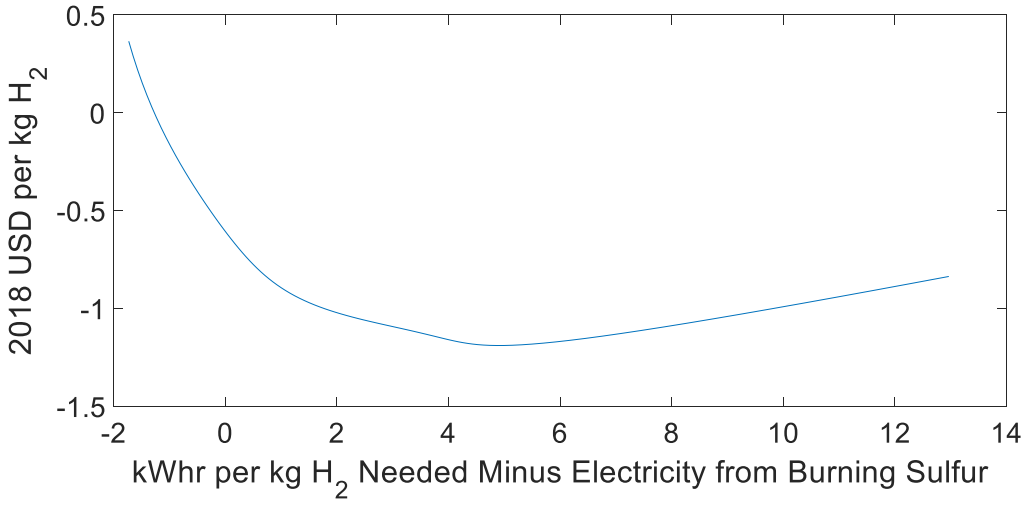

Figure 3: Relationship between excess energy required beyond what was available from burning sulfur assuming a 30% conversion efficiency vs the cost of hydrogen. The primary control on energy consumption is the operating voltage of the electrolyzer. As operating voltage and current density (e.g. kWh per kg H_2) decreases, so does energy requirement per kg H_2, but the number of electrolyzers needed to make a given amount of hydrogen increases leading to a higher cost.

We use an average emissions factor for grid electricity of 0.290 kg CO_2/kWhr (based on 2018 US data)[27]. CO_2 emissions would be further decreased if a natural gas power plant (0.459 kg CO_2 / kWhr) was used instead of an average grid[27]. Electricity harvested from sulfur burning, PV, or PV plus batteries was assumed to emit no CO_2. If sulfuric acid concentration was necessary, electricity or natural gas requirements were taken into account (see Tables S1-2 and Figs. S2-3 for details).

Sensitivity Analysis

We perform sensitivity analyses to determine how the price of hydrogen would respond to several factors: electrolyzer current density, amount of produced hydrogen, CapEx of the components, catalyst stability, catalyst activity, process faradaic efficiency, catalyst cost, prices of sulfur and sulfuric acid, the rate of return, and cost of electricity (from PV, grid, or batteries), CO_2 emissions, and a CO_2 tax. For each sensitivity analysis, the parameter of interest was varied while the current density and capacity factor of the plant changed to find the cheapest possible plant configuration. All other parameters were set to constant values. Parameter values as well as ranges for values are presented in Table 1. . Real data from lab scale SDEs were used for current density and corresponding voltages[51]. Current density was corrected based on an empirical relationship between voltage and faradic efficiency (see Figs. S4-S6 and eqs. S4-S6 for details). A detailed discussion of sensitivity parameter range selection may be found in Table S3

Comparing Cogeneration via SE to SMR

We seek to understand the LCH from SE compared to the LCH from the standard hydrogen generation process, SMR. It is difficult to make a direct comparison with the SE process because it makes two commodities, hydrogen and sulfuric acid, whereas SMR only makes a single hydrogen commodity. For the purposes of this analysis, we make this comparison by subtracting out the revenue of selling sulfuric acid ($7.02 per 49 kg), leaving only the minimum production price of hydrogen[62]. Another way of comparing these costs would be to subtract a levelized cost of sulfuric acid production via the CP which would represent a maximum LCH ($6.83 per 49 kg according to our model). We perform our analysis using both methods. We find negligible differences between the results, which agrees with the market reality that profit margins on commodity chemicals are thin (~10%)[62]. We present results from the former method because the selling price of sulfuric acid has been validated by the market whereas the levelized cost of sulfuric acid is an estimate (see tables S4-5 for details on levelized cost of sulfuric acid and hydrogen via the CP and SMR).

Results and Discussion

Levelized Cost of Hydrogen Under Standard Assumptions

First, we ran our model under standard assumptions to estimate the LCH from SE. Our techno-economic model estimates that the LCH from SE is - $0.75/kg H_2 for 70% sulfuric acid and $0.51/kg H_2 for 96% sulfuric acid (fig. 4). These prices are considerably lower than the LCH from SMR ($1.25

/kg H_2). These data suggest that hydrogen produced via SE may be able to enter the market in the very near term.

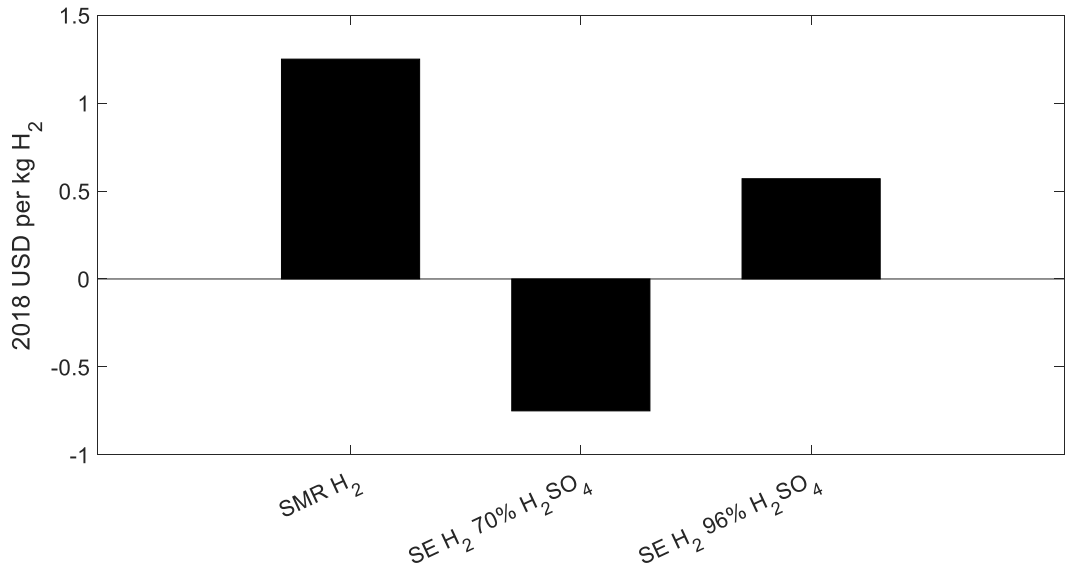

Figure 4: Levelized Costs Hydrogen from SMR and Grid-Assisted SE. Levelized costs of H_2/kg via Steam Methane Reforming (left), Sulfur Electrolysis with 70% H_2SO_4 (center), Sulfur Electrolysis with 96% H_2SO_4 (left). Sulfur Electrolysis was modeled herein and Steam Methane Reforming pricing was taken from 2018 NREL data (cite). All prices assume 350 to 400 tonnes/day H_2 production.

A sensitivity analysis for grid assisted SE may be found in figs S8-S9. Next, we investigate the production of totally CO_2-free hydrogen (according to the assumptions of our model). To do this, we prohibit our model from using grid electricity and allow it to alter the current density, capacity factor, and quantity of solar panels and batteries to find the cheapest LCH. Under standard assumptions, solar-only LCH is $1.29/kg when 70% sulfuric acid is cogenerated and $2.32/kg when 96% sulfuric acid is cogenerated (Fig. 5). Both of these values are more expensive than SMR, thus rendering it an

unlikely near-term industrial solution. One possible strategy to reduce the cost of this CO_2-production method could be to use other renewable electricity including wind, geothermal, and hydroelectric energy which could increase the capacity factor.

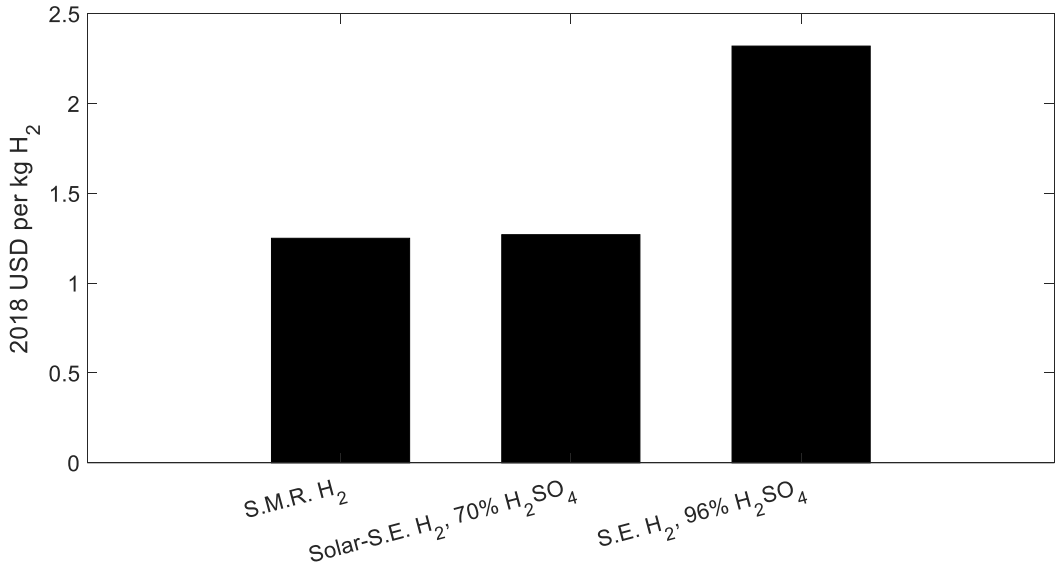

Fig. 5: Levelized Costs Hydrogen from SMR and Solar-Only SE. Cost of SMR (left), solar-only powered SE without concentration (center), and solar-only powered SE with concentration (right).

CO_2 Emissions Analysis

Emissions based on SMR

Under standard assumptions, the calculated cheapest price for hydrogen for sulfur electrolysis occurred when the reaction required was 10 kWhr/kg (33 kWhr/kg if no electricity is harvested from sulfur combustion). This happened to occur around the point where the current density switched from the mass transfer limited regime to the charge transfer limited regime (see fig. S4). With an economically optimal solar penetration, SE was found to have fewer greenhouse gas emissions than SMR by almost a factor of 2 even if sulfuric acid needed to be concentrated to 96% (fig. 6.)

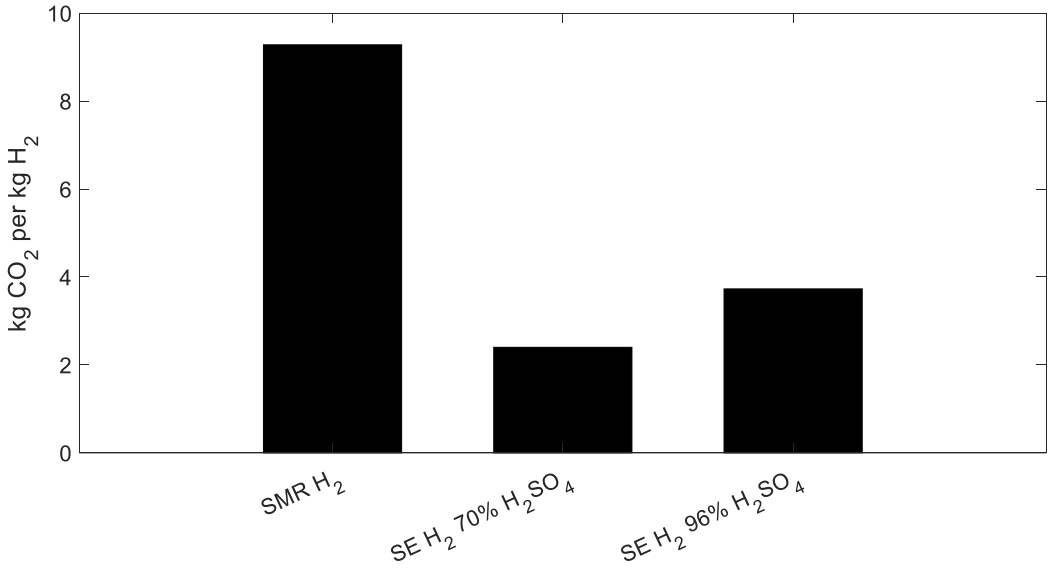

Fig. 6: CO_2 Emissions of SMR and Grid-Assisted SE. CO_2 emissions of SMR (left), grid powered sulfur electrolysis without concentration (middle), and grid powered sulfur electrolysis with concentration (right)

These data indicate that if SE were to meet the global demand for sulfuric acid (~3 teramoles in 2017)[48] and the produced hydrogen were to replace around 10% of global hydrogen demand as a commodity chemical, then up to 40 MMT of global CO_2 emissions could be avoided by the grid assisted SE method. Under a renewables-only scenario, current technology for SE is not cheap enough to make hydrogen that is competitive with hydrogen from SMR. If technological advances are able to make renewables-only SE cost competitive with SMR, the process could reduce CO_2 emissions by up to 120 MMT.

Pathways to Cheaper Clean Hydrogen

Under standard assumptions with sulfuric acid concentration and the use of only solar derived electricity, SE was modeled to make hydrogen that costs $1.29/kg for 70% sulfuric acid and $2.32/kg for 96% sulfuric acid (fig 6). This configuration would result in the greatest CO_2 emissions reduction. Because solar-only SE is CO_2-free according to the assumptions of this model, one way to make solar-only SE cost competitive with SMR is to levy a carbon tax of $115/tonne of CO_2.

We conduct a sensitivity analysis to understand what would be necessary for solar-only SE to be cost-competitive with SMR. We found that for SE, many individual improvements were more than enough to reduce the LCH to below that of SMR including reducing the voltage requirement, reducing the solar or battery module CapEx, and reducing the balance of systems or electrolyzer CapEx (fig 7). Consistent with prior research on noble metal based catalysts, even an order of magnitude increase in the CapEx of the catalyst did not increase the LCH by more than 3.6%. These data indicate that with reasonable R&D improvements, solar-only SE may be cost competitive with SMR.

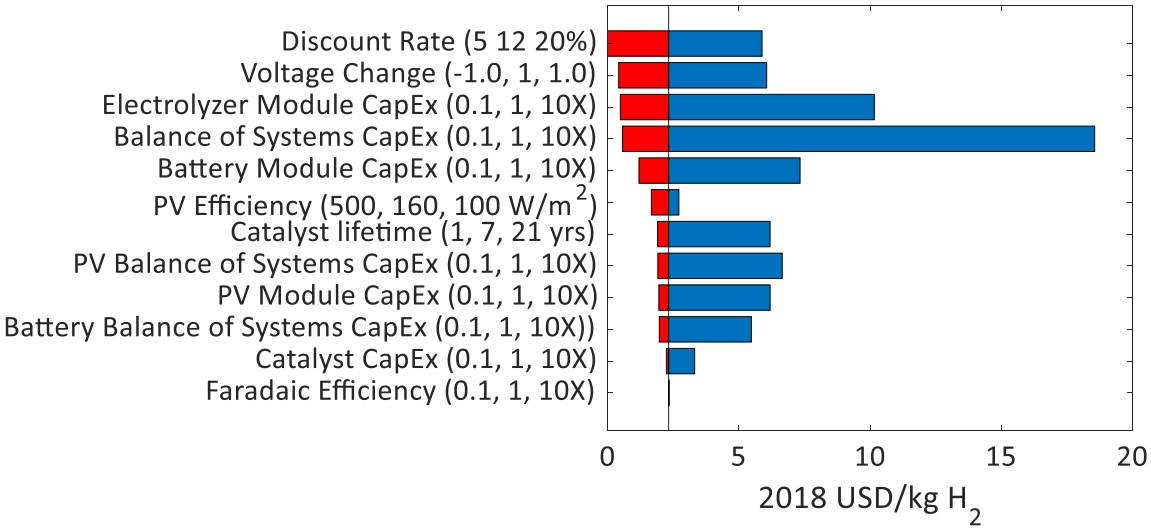

Figure 7: Sensitivity Analysis of Solar-Only Sulfur Electrolysis. The parenthetical numbers on the vertical axis indicate the low, standard, and high assumption for each case.

This analysis best way to reduce the cost of hydrogen from SE is to reduce the discount rate from 12% to 5%, this could be done by de-risking the technology which may happen gradually as the technology matures and becomes installed at larger scales and operated for longer times, or it may happen with government grants.

Comparison to Water Electrolysis

Lastly, we analyzed how the economics of making hydrogen from WE compares with SE (see figs. S6-7 for details on physical parameters of WE). We used H2A WE data in our model and found that the LCH for grid powered WE was \$5.72/kg H_2 (consistent with the H2A model plus our

conservative assumptions) while solar-only WE was $9.91/kg (consistent with Shaner et al.)[21]. Grid based WE is both more expensive and more CO_2 intensive than SMR according to the assumptions of our model. As such, we did not consider how to make it cheaper and instead focused on solar-only WE which could reduce CO_2 emissions. The LCH for solar-only WE is four times higher than the LCH for solar-only SE, largely driven by the higher energy consumption and lack of cogeneration product credit. Solar-only WE would require a considerably larger CO_2 tax, $933/tonne, to be cost competitive with SMR in comparison to solar-only SE's $115 required CO_2 tax.

We also conducted a sensitivity analyses on model parameters for solar-only WE and found that unlike solar-only SE, no single improvement could reduce the LCH from solar-only WE to be competitive with SMR. Instead, at least three improvements needed to be combined in order to reduce the cost of WE to below $1.25/kg H_2 (fig. 8). For example, if the peak power rating on PV was increased from 160 W/m^2 to 500 W/m^2, and the CapEx or batteries modules, electrolyzers, and plant balance of systems all decreased by an order of magnitude, solar-only WE would be cheaper than SMR. Finally, similar to previous findings, even reducing the CapEx of the catalyst by an order of magnitude would only reduce the LCH by 1.8%[21,26]. These data indicate that many more improvements would need to be made to a WE system than to a SE system to make solar-only hydrogen production cost competitive with SMR.

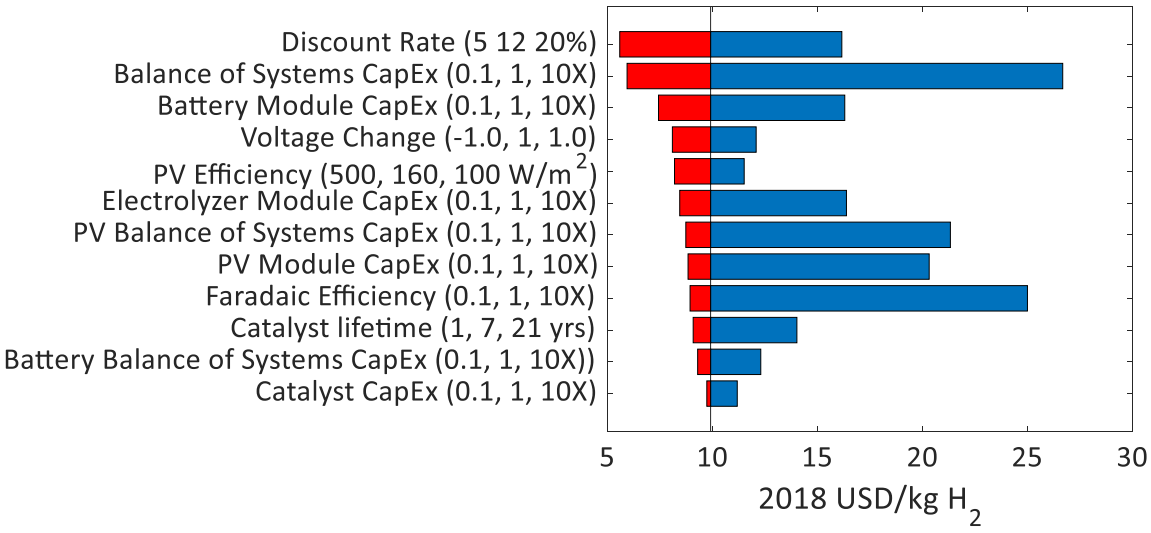

Figure 8: Sensitivity Analysis of Solar-Only Water Electrolysis. The parenthetical numbers on the vertical axis indicate the low, standard, and high assumption for each case.

Conclusions

In this study, we modeled the economics of electrochemical cogeneration of sulfuric acid and hydrogen via SE using demonstrated reaction conditions and CapEx and OpEx assumptions based on currently installed equipment. We find that with current technology, the hydrogen production from SE is lower cost, lower energy, and lower emissions than SMR when run on an average US grid. This process has both favorable thermodynamics and economically advantageous cogeneration and represents a viable current or near term pathway to reducing the CO_2 emissions associated with hydrogen production. We also investigated solar-only SE which is completely CO_2-free according to the assumptions of our model. We find that this process is nearly cost competitive with SMR. Finally, we compared the long-term feasibility of SE to WE and find that there are many more pathways to economic viability for SE than WE.

This is the first study that we are aware of that shows a potentially clean hydrogen production strategy that could be cheaper than SMR using existing technologies and produce hydrogen at an industrially relevant scale. We acknowledge that SE alone could not make enough hydrogen to meet the entire current demand and especially not the future demand for hydrogen if it becomes a major transportation fuel of energy carrier. However, we believe that cogeneration of hydrogen with major commodity chemicals in innovative ways (e.g. a 3:1 molar ratio of hydrogen and sulfuric acid or cogeneration of hydrogen and calcium oxide for cement) could represent a paradigm shift in producing economically advantageous, low greenhouse gas emissions hydrogen in the very near term.

Works Cited

1. Net-zero emissions energy systems | Science. https://science.sciencemag.org/content/360/6396/eaas9793/tab-figures-data.
2. Intergovernmental Panel on Climate Change. *Global warming of 1.5°C*. (2018).
3. Global Nitrous Oxide Production Determined by Oxygen Sensitivity of Nitrification and Denitrification - Ji - 2018 - Global Biogeochemical Cycles - Wiley Online Library. https://agupubs.onlinelibrary.wiley.com/doi/full/10.1029/2018GB005887.

4. The Kyoto Protocol and non-CO2 Greenhouse Gases and Carbon Sinks | SpringerLink. https://link.springer.com/article/10.1023/A:1020910820102.
5. Giant batteries and cheap solar power are shoving fossil fuels off the grid | Science | AAAS. https://www.sciencemag.org/news/2019/07/giant-batteries-and-cheap-solar-power-are-shoving-fossil-fuels-grid.
6. Wilson, M. Lazard's Levelized Cost of Storage Analysis—Version 4.0. 60.
7. Powering the Planet: Where in the World Will Our Energy Come From? - Nate Lewis - 5/25/2005 - YouTube. https://www.youtube.com/watch?v=EUKqx2uk-Gs.
8. British Columbia's Carbon Tax - Province of British Columbia. https://www2.gov.bc.ca/gov/content/environment/climate-change/planning-and-action/carbon-tax.
9. Waltzer, K. The Role of 45Q Carbon Capture Incentives in Reducing Carbon Dioxide Emissions. 3.
10. A Process for Capturing CO2 from the Atmosphere | Elsevier Enhanced Reader. https://reader.elsevier.com/reader/sd/pii/S2542435118302253?token=94C153D93CD1105CB152A64E509F13D1B4BA8AF8CB094A5A14CFC1FC96E505F69DA439AAE6342A3907B24539CB694923 doi:10.1016/j.joule.2018.05.006.
11. Implications for climate and sea level of revised IPCC emissions scenarios | Nature. https://www.nature.com/articles/357293a0.
12. Global water cycle agreement in the climate models assessed in the IPCC AR4 - Waliser - 2007 - Geophysical Research Letters - Wiley Online Library. https://agupubs.onlinelibrary.wiley.com/doi/full/10.1029/2007GL030675.

13. Biological Wastewater Treatment - Google Books. https://books.google.com/books?hl=en&lr=&id=41JButufnm8C&oi=fnd&pg=PA1&dq=biological+wastewater+treatment&ots=nSH1f3xB5i&sig=MqMlR69u-ju3gvnuKxy6keyNnZc#v=onepage&q=biological%20wastewater%20treatment&f=false.
14. Developments in wastewater treatment methods - ScienceDirect. https://www.sciencedirect.com/science/article/pii/S0011916404003558.
15. Breakpoint chlorination and free-chlorine contact time: Implications for drinking water N-nitrosodimethylamine concentrations - ScienceDirect. https://www.sciencedirect.com/science/article/abs/pii/S0043135406004441.
16. Contributions of electrochemical oxidation to waste-water treatment: fundamentals and review of applications - Anglada - 2009 - Journal of Chemical Technology & Biotechnology - Wiley Online Library. https://onlinelibrary.wiley.com/doi/abs/10.1002/jctb.2214.
17. Phosphate Recovery from Human Waste via the Formation of Hydroxyapatite during Electrochemical Wastewater Treatment | ACS Sustainable Chemistry & Engineering. https://pubs.acs.org/doi/abs/10.1021/acssuschemeng.7b03155.
18. Electrochemical disinfection of toilet wastewater using wastewater electrolysis cell - ScienceDirect. https://www.sciencedirect.com/science/article/pii/S0043135416300392.
19. Jasper, J. T., Yang, Y. & Hoffmann, M. R. Toxic Byproduct Formation during Electrochemical Treatment of Latrine Wastewater. *Environ. Sci. Technol.* **51**, 7111–7119 (2017).
20. Lee, D.-Y., Elgowainy, A. A. & Dai, Q. *Life Cycle Greenhouse Gas Emissions of By-product Hydrogen from Chlor-Alkali Plants*. https://www.osti.gov/biblio/1418333 (2017) doi:10.2172/1418333.

21. Shaner, M. R., Atwater, H. A., Lewis, N. S. & McFarland, E. W. A comparative technoeconomic analysis of renewable hydrogen production using solar energy. *Energy Environ. Sci.* **9**, 2354–2371 (2016).
22. Reinvent the Toilet Challenge & Expo - Bill & Melinda Gates Foundation. https://www.gatesfoundation.org/what-we-do/global-growth-and-opportunity/water-sanitation-and-hygiene/reinvent-the-toilet-challenge-and-expo.
23. Christopher, K. & Dimitrios, R. A review on exergy comparison of hydrogen production methods from renewable energy sources. *Energy Environ. Sci.* **5**, 6640–6651 (2012).
24. Wismann, S. T. *et al.* Electrified methane reforming: A compact approach to greener industrial hydrogen production. *Science* **364**, 756–759 (2019).
25. Petroleum Coke. https://www.eia.gov/dnav/pet/PET_PNP_CAPFUEL_A_(NA)_8FPP0_MBBL_A.htm.
26. H2A: Hydrogen Analysis Production Models | Hydrogen and Fuel Cells | NREL. https://www.nrel.gov/hydrogen/h2a-production-models.html.
27. How much carbon dioxide is produced per kilowatthour of U.S. electricity generation? - FAQ - U.S. Energy Information Administration (EIA). https://www.eia.gov/tools/faqs/faq.php?id=74&t=11.
28. webmaster. A Review of Water Scarcity Indices and Methodologies. *The Sustainability Consortium* https://www.sustainabilityconsortium.org/downloads/a-review-of-water-scarcity-indices-and-methodologies/.
29. Falkenmark, M. The Massive Water Scarcity Now Threatening Africa: Why Isn't It Being Addressed? *Ambio* **18**, 112–118 (1989).

30. 2015 - Water for a Sustainable World | United Nations Educational, Scientific and Cultural Organization. http://www.unesco.org/new/en/natural-sciences/environment/water/wwap/wwdr/2015-water-for-a-sustainable-world/.
31. Gerland, P. *et al.* World population stabilization unlikely this century. *Science* **346**, 234–237 (2014).
32. Lackner, K. S. CLIMATE CHANGE: A Guide to CO2 Sequestration. *Science* **300**, 1677–1678 (2003).
33. US EPA, O. Climate Impacts in the Southwest. /climate-impacts/climate-impacts-southwest.
34. The Water Crisis: Poverty and Water Scarcity in Africa. *The Water Project* https://thewaterproject.org/why-water/poverty.
35. Gleick, P. H. Basic Water Requirements for Human Activities: Meeting Basic Needs. *Water Int.* **21**, 83–92 (1996).
36. *Progress on drinking water and sanitation: 2014 update*. (World Health Organization, 2014).
37. Berge, N. D. *et al.* Hydrothermal Carbonization of Municipal Waste Streams. *Environ. Sci. Technol.* **45**, 5696–5703 (2011).
38. Abdeen, S., Di, W., Hui, L., Chen, G.-H. & van Loosdrecht, M. C. M. Fecal coliform removal in a sulfate reduction, autotrophic denitrification and nitrification integrated (SANI) process for saline sewage treatment. *Water Sci. Technol.* **62**, 2564–2570 (2010).
39. Solutions when the Solution is the Problem: Arraying the Disarray in Development - Working Paper 10. *Center For Global Development* https://www.cgdev.org/publication/solutions-when-solution-problem-arraying-disarray-development-working-paper-10.
40. Mobile cellular subscriptions (per 100 people) | Data. https://data.worldbank.org/indicator/IT.CEL.SETS.P2.

41. NW, 1615 L. St, Suite 800Washington & Inquiries, D. 20036USA202-419-4300 | M.-857-8562 | F.-419-4372 | M. Smartphone Ownership Is Growing Rapidly Around the World, but Not Always Equally. *Pew Research Center's Global Attitudes Project* https://www.pewresearch.org/global/2019/02/05/smartphone-ownership-is-growing-rapidly-around-the-world-but-not-always-equally/ (2019).
42. Water Quality and Treatment: A Handbook on Drinking Water, Sixth Edition. *AWWA-American Water Works Association* https://www.awwa.org/Store/{ProductName}/ProductDetail/{ProductId}?productId=6292.
43. Finke, C. E. *et al.* Maintenance self-diagnosis and guide for a self-contained wastewater treatment system. (2017).
44. Ogden, J. M. Prospects for building a hydrogen energy infrastructure. *Annu. Rev. Energy Environ.* **24**, 227–279 (1999).
45. Ave, H. Support for Cost Analyses on. 76 (2011).
46. Techno-Economic Analysis of Methane Pyrolysis in Molten Metals: Decarbonizing Natural Gas - Parkinson - 2017 - Chemical Engineering & Technology - Wiley Online Library. https://onlinelibrary.wiley.com/doi/abs/10.1002/ceat.201600414.
47. Catalytic molten metals for the direct conversion of methane to hydrogen and separable carbon | Science. https://science.sciencemag.org/content/358/6365/917/tab-figures-data.
48. A World of Sulfur. *World Fertilizer* https://www.worldfertilizer.com/special-reports/24122018/a-world-of-sulfur/ (2018).
49. Nieuwenhuyse, A. E. van. *Best Available Techniques for Pollution Prevention and Control in the Eiropean Fertilizer Industry*. vol. 8 (2000).

50. Kumareswaran Subasgar *et al.* Design of a Plant to Manufacture Sulfuric Acid from Sulfur. (2013) doi:10.13140/RG.2.1.1083.2724.

51. Weidner, J. W. Electrolyzer performance for producing hydrogen via a solar-driven hybrid-sulfur process. *J. Appl. Electrochem.* **46**, 829–839 (2016).

52. Nieuwenhuyse, A. E. van. *Best Available Techniques for Pollution Prevention and Control in the European Sulphuric Acid and Fertilizer Industries*. (European FertilizerManufacturers' Association, 2000).

53. Lulu, X., Ping, Z., Songzhe, C. & Laijun, W. Quantitative analysis of the cell voltage of SO2-depolarized electrolysis in hybrid sulfur process. *Nucl. Eng. Des.* **306**, 203–207 (2016).

54. Sulfuric Acid Corrosion | H2SO4 Corrosion | Sulphuric Acids. https://tubingchina.com/Sulfuric-Acid-H2SO4-Corrosion.htm.

55. Gorensek, M. B., Staser, J. A., Stanford, T. G. & Weidner, J. W. A thermodynamic analysis of the SO2/H2SO4 system in SO2-depolarized electrolysis. *Int. J. Hydrog. Energy* **34**, 6089–6095 (2009).

56. Economics and Chemical Engineering. in *Chemical Engineering for Non-Chemical Engineers* 79–87 (John Wiley & Sons, Ltd, 2017). doi:10.1002/9781119369196.ch6.

57. Li, F. *Situation and Practical Data of Sulfuric Acid Vacuum Concentration Unit of NCIC*.

58. EIA - Electricity Data. https://www.eia.gov/electricity/monthly/epm_table_grapher.php?t=epmt_5_6_a.

59. Shaner, M. R., Davis, S. J., Lewis, N. S. & Caldeira, K. Geophysical constraints on the reliability of solar and wind power in the United States. *Energy Environ. Sci.* **11**, 914–925 (2018).

60. Ardani, K. *et al. Installed Cost Benchmarks and Deployment Barriers for Residential Solar Photovoltaics with Energy Storage: Q1 2016*. http://www.osti.gov/servlets/purl/1338670/ (2016) doi:10.2172/1338670.
61. Jechura, J. Hydrogen from Natural Gas via Steam Methane Reforming (SMR). 21.
62. Green Markets. *Green Markets* https://fertilizerpricing.com/pricing-news/green-markets/.
63. Garrett, D. E. *Chemical Engineering Economics*. (Van Nostrand Reinhold, 1989).
64. Pierre Millet *et al.* Implementation of cobalt clathrochelates in polymer electrolyte water electrolysers for hydrogen evolution. *Chem. Eng. Trans.* **41**, 325–330 (2014).
65. O'Brien, T. F., Bommaraju, T. V. & Hine, F. *Handbook of Chlor-Alkali Technology: Volume I: Fundamentals, Volume II: Brine Treatment and Cell Operation, Volume III: Facility Design and Product Handling, Volume IV: Operations, Volume V: Corrosion, Environmental Issues, and Future Developments*. (Springer US, 2005).
66. SUMNER, J., BIRD, L. & DOBOS, H. Carbon taxes: a review of experience and policy design considerations. *Clim. Policy* **11**, 922–943 (2011).
67. Corgnale, C. & Summers, W. A. Solar hydrogen production by the Hybrid Sulfur process. *Int. J. Hydrog. Energy* **36**, 11604–11619 (2011).
68. Jayakumar, J. V. *et al.* Polybenzimidazole Membranes for Hydrogen and Sulfuric Acid Production in the Hybrid Sulfur Electrolyzer. *ECS Electrochem. Lett.* **1**, F44–F48 (2012).
69. Opperman, H., Kerres, J. & Krieg, H. SO2 crossover flux of Nafion® and sFS-PBI membranes using a chronocoulometric (CC) monitoring technique. *J. Membr. Sci.* **415–416**, 842–849 (2012).
70. Khan, H. A. *et al.* Pt encapsulated hollow mesoporous SiO2 sphere catalyst for sulfuric acid decomposition reaction in SI cycle. *Int. J. Hydrog. Energy* **44**, 2312–2322 (2019).

71. Kodera, F., Kuwahara, Y., Nakazawa, A. & Umeda, M. Electrochemical corrosion of platinum electrode in concentrated sulfuric acid. *J. Power Sources* **172**, 698–703 (2007).

72. Davie, M. G., Cheng, H., Hopkins, G. D., LeBron, C. A. & Reinhard, M. Implementing Heterogeneous Catalytic Dechlorination Technology for Remediating TCE-Contaminated Groundwater. *Environ. Sci. Technol.* **42**, 8908–8915 (2008).

73. Author, N. G. *Water and Wastewater Annual Price Escalation Rates for Selected Cities across the United States*. http://www.osti.gov/servlets/purl/1413878/ (2017) doi:10.2172/1413878.

74. Lalvani, S. B. & Dave, B. Simultaneous production of hydrogen and sulfuric acid from aqueous sulfur slurry. *Int. J. Hydrog. Energy* **11**, 639–646 (1986).

75. Ellis, L. D., Badel, A. F., Chiang, M. L., Park, R. J.-Y. & Chiang, Y.-M. Toward electrochemical synthesis of cement—An electrolyzer-based process for decarbonating $CaCO_3$ while producing useful gas streams. *Proc. Natl. Acad. Sci.* 201821673 (2019) doi:10.1073/pnas.1821673116.

Supplementary Information For:

An Economically Advantageous Method for Clean Hydrogen Production in the Present or Near-Term

Cody E. Finke, Neil A. Fromer, David Zheng, Fanfei Li, Michael R. Hoffmann

Contents:

CapEx of Sulfur Furnace

We estimated the CapEx of a sulfur furnace which generates electricity and separates SO_2 from flue gas to be the same as a contact process plant which generates electricity and separates SO_2 from flue gas as well as makes H_2SO_4 thermochemically. We believe that this is a conservative estimate because the contact process has everything that our sulfur burning process needs plus downstream reactors to make oleum from SO_2 and sulfuric acid from oleum. We used a known CapEx and size relationship from Garret, 1989 to estimate the economics of the contact process[63].

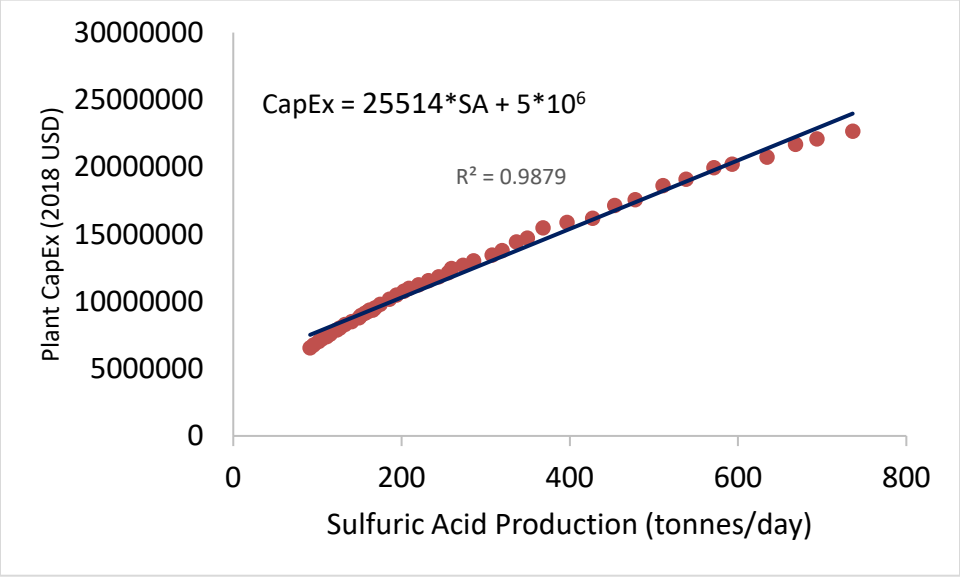

Fig. S1: CapEx of a sulfuric acid data. CapEx of contact process plants versus sulfuric acid production rate (orange dotted line), overlayed with the best linear fit (blue solid line)[63].

The relationship from the above graph may be found in equation S1. In Equation S1, SA is sulfuric acid production per day in metric tonnes and CapEx is overnight capital expenditure in 2018 USD.

$$CapEx = 25514*SA + 5*10^6 \quad (S1)$$

CapEx and OpEx of Sulfuric Acid Concentration

To determine the cost of electrochemical concentration of sulfuric acid, we modeled a sulfuric acid concentration process using real OpEx and CapEx data for a vacuum concentration process provided via personal correspondence with a senior manager at a Nanjing sulfuric acid vacuum concentration plant owned by Sinopec Nanjing Chemical Industry Co. Ltd (correspondence may be found in the pdf labeled *NanjingCorrespondence_report.pdf*). Data used for CapEx may be found in table S1. This plant concentrates sulfuric acid to 96%.

Table S1: CapEx for sulfuric acid concentration

Plant Size (tonnes H_2SO_4 / dy)	CapEx (2018 USD)
0.018	30,000
1.45	125,000
72	1,595,000
500	3,814,286
1,000	5,814,286

Data in table S1 were graphed in fig. S2 to find the empirical relationship in equation S2.

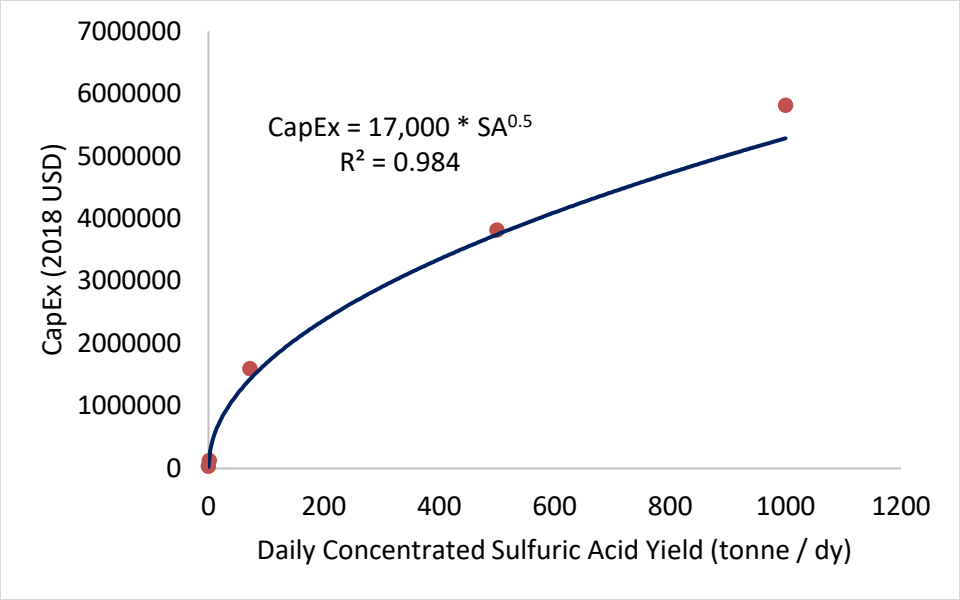

Fig. S2. CapEx of Sulfuric Acid Vacuum Concentration Plants. The best fit relationship between CapEx and Sulfuric Acid yield for a concentration plant (data from table S1). While this best fit line may be an underestimate of sulfuric acid concentration CapEx.

The relationship between CapEx and OpEx is in Eq. 2 where CapEx is the capital expenditure and SA is the amount of sulfuric acid produced in tonnes/day.

$$CapEx = 17{,}000 * SA^{0.5} \quad \text{(S2)}$$

OpEx data for this process may be found in table S2 below.

Table S2:

Initial Concentration of H_2SO_4 (%)	OpEx ($ / tonne H_2SO_4)
45	56.25
55	42.25
65	31.25
75	20.88
85	12.50

Data in table S2 were graphed in fig. S3 to find the empirical relationship in equation S3.

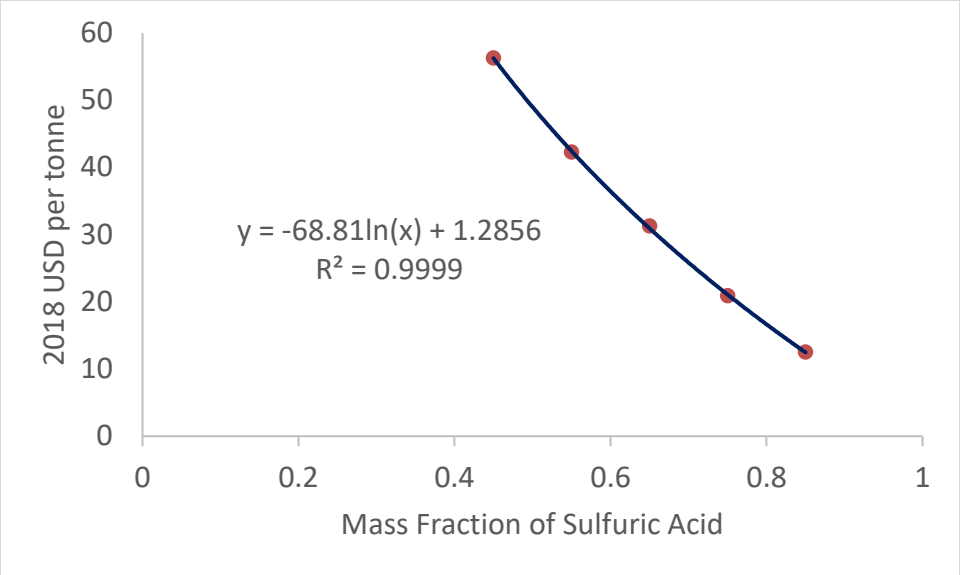

Fig. S3. OpEx of Sulfuric Acid Vacuum Concentration Plants. OpEx for sulfuric acid concentration from table S2. Sulfuric acid was concentrated from an initial concentration to 96%. The relationship between OpEx and sulfuric acid concentration is in Eq. S3 where OpEx is the OpEx per tonne sulfuric acid and C is the concentration of sulfuric acid in percent mass.

$$OpEx = -1.2443 * C + 118.16 \quad (S3)$$

Voltage and Current relationships

Sulfur and water electrolysis voltage and current density data were fit from real SDE data.

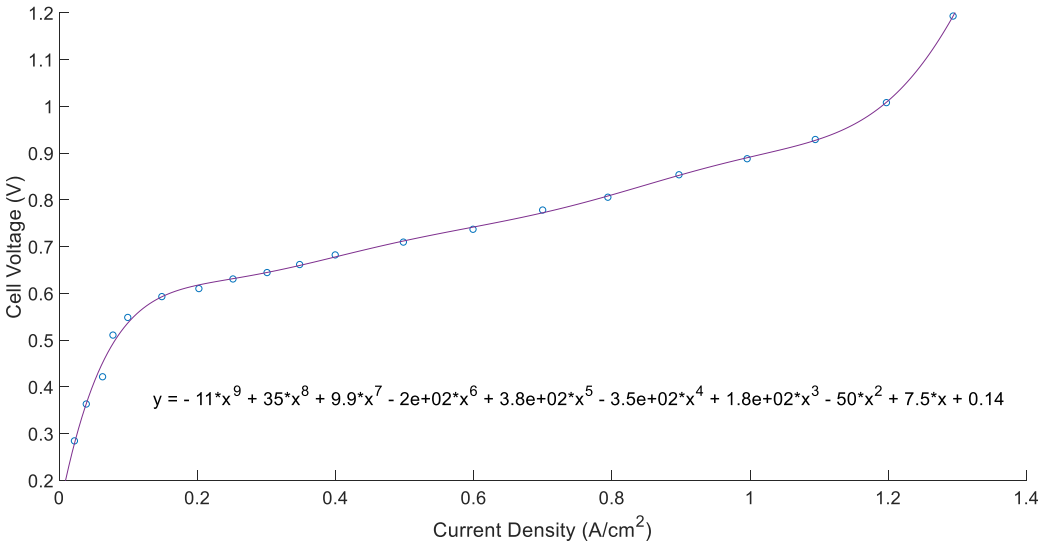

Fig. S4. Voltage and Current Relationship for an SDE. Data interpolation of a real lab scale sulfur depolarization electrolyzer[51].

The empirical relationship between cell voltage (V) and current density (CD) are in equation S4.

$$V = - 10.642*CD^9 + 35.299*CD^8 + 9.8505*CD^7 - 200.7*CD^6 + 379.95*CD^5 - 346.31*CD^4 + 175.38*CD^3 - 49.626*CD^2 + 7.5476*CD + 0.13509 \quad (S4)$$

A voltage shift to account for different starting concentrations of sulfuric acid was used.

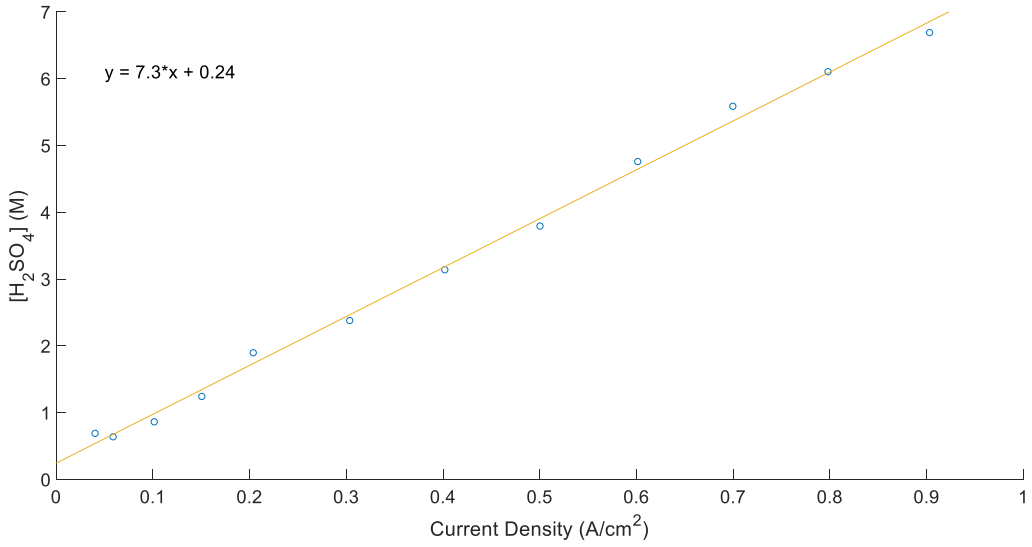

Fig. S5. Graph showing fit of sulfuric acid concentration. Data interpolation of a real lab scale sulfur depolarization electrolyzer[51]. The interpolated relationship can be found in Eq. S5.

The empirical relationship between cell sulfuric acid concentration in molar (SA) and current density (CD) may be found in Eq. S6 below. These data were used to determine the concentration of sulfuric acid that was output for a given current density.

$$SA = 7.3 * CD + 0.24 \quad (S5)$$

A voltage shift (ΔV) for different concentrations of sulfuric acid and solubility of SO_2 was applied to the equation based on an empirical relationship of applied potential vs acid concentration derived by Weidner et al, this relationship can be found in Eq. S6 where the shift is cell voltage relative to a water electrolyte is ΔV versus the concentration of sulfuric acid in molar (SA).

$$\Delta V = 0.00052 * SA^3 - 0.0087 * SA^2 + 0.07 * SA + 0.084 \quad \text{(S6)}$$

Voltage and Faradaic Efficiency

For both SE and WE the current density was corrected for faradic efficiency based on voltage from the below graph[64].

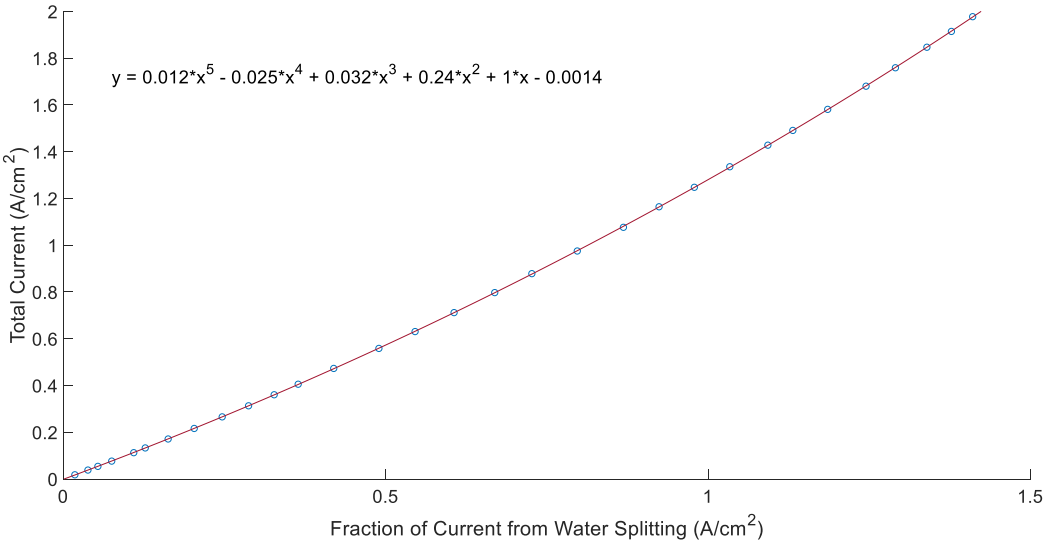

Fig. S6 Graph showing faradic efficiency for a water electrolysis system. The fraction of current from water splitting is the total current corrected to have 100% faradaic efficiency.

Sensitivity Analysis

Table S3: Annotated sensitivity analysis parameters.

Variable	Low Value	High Value	Standard Assumption	Discussiosn
Inputs and Outputs				
H_2 Produced[a]	1,000	400,000	400,000	1000 kg H_2 / dy is the H2A forecourt assumption while 400,000 kg H_2 / dy is the H2A centralized assumption[26].
Buying Price of Sulfur[c]	-0.1	0.45	0.13	This price range was taken from Bloomberg industrial analysis of high and low prices for sulfur. The standard price 2017 West Coast USA contract pricing[62].
Selling Price of Sulfuric Acid[d]	0.05	0.33	0.143	This price range was taken from Bloomberg industrial analysis of high and low prices for sulfuric acid. The standard assumption price was the price for 2017 West Coast USA contract pricing[62].

Buying Price of Grid Electricity[e]	0.1	0.3		High and low US energy information administration (EIA) prices. The standard price is the average US industrial price of electricity[58].
Selling Price of Grid Electricity[e]	0.005	0.18	0.07	High and low US energy information administration (EIA) prices[58].
Catalyst Parameters and Components				
SE[l] Catalyst Geometric Current Density[b]	0.33	1.5	1.21	The ranges for SE and WE were taken from real data on either a highly advanced prototype (SE)[51] or a commercial prototype (WE)[64]. All values were corrected to 100% faradaic efficiency
WE[m] Catalyst Geometric Current Density[b]	0.33	1.5	1.48	The ranges for SE and WE were taken from real data on either a highly advanced prototype

				(SE)[51] or a commercial unit (WE)[64]. All values were corrected to 100% faradaic efficiency
Voltage Shift[g]	-1.0	1	0	Shifting the voltage for a given current density up or down by a volt represents incredibly large changes in the quality of the catalyst[7].
Catalyst CapEx Cost Coefficient	0.1	1	1	An order of magnitude increase or decrease would be a very large change.
Catalyst Lifetime[i]	1	21	7	For the chlor-alkali process, the catalyst lifetime is around 7 years[65]. 7 years is also the H2A assumption. 21 years would be a major increase. Less than 1 year would be a very unstable catalyst[26].

Catalyst Faradic Efficiency Factor	0.1	10	1	An order of magnitude increase or decrease would be a very large change.
PV Parameters and Components				
PV Nameplate Peak Power[f]	0.1	0.5	0.16	0.16 kW/m^2 is a common solar peak power density. 0.5 kW/m^2 is a common research goal for PV researchers[59].
PV Balance of Systems Cost Coefficient	0.1	1	1	An order of magnitude increase or decrease would be a very large change.
PV Module Cost Coefficient	0.1	1	1	An order of magnitude increase or decrease would be a very large change.
Battery Components				
Battery Module Cost Coefficient	0.1	1	1	An order of magnitude increase or decrease would be a very large change.
Battery Balance of Systems Cost Coefficient	0.01	1	1	An order of magnitude increase or decrease would be a very large change.

Economic and Operating Parameters				
Capacity Factor	0.01	0.97	0.97	A capacity factor of 97% is the H2A assumption[26].
Rate of Return	0.05	0.20	0.12	A 12% rate of return is a high rate of return value that represents a large fraction of equity investment vs debt investment and has been used in previous conservative studies[21].
Carbon Tax[j]	0	1	0.00	0 represents no tax on carbon while 1 represents $1000/tonne which is very high tax on carbon, most proposed taxes are much lower[66].
Carbon Intensity of Grid Electricity[k]	0	1	0.29	0.29 is the carbon intensity of the US grid. 1 kg CO_2/ kWhr would

				represent wood burning or very dirty coal based electricity generation[27].
Initial Sulfuric Acid Concentration[h]	0.0	18.0	10.0	The higher the initial sulfuric acid concentration, the higher the final concentration can be based on the solubility of SO_2 and the flow rate in demonstrated reactors, 18.0 M H_2SO_4 is 98% sulfuric acid which is the highest grade concentration[55].
Electrolyzer Components				
Electrolyzer Balance of Systems Cost Coefficient	0.1	1	1	An order of magnitude increase or decrease would be a very large change.
Electrolyzer Cost Coefficient	0.1	1	1	An order of magnitude increase or decrease would be a very large change.

Note. [a] kg / dy [b] A / cm^2 [c] % / kg [d] $ / kg [e] $ / kWhr [f] kW / m^2 peak power [g] V [h] M [I]7 yrs [j] $ / kg CO_2. [k] Kg CO_2 / kg kWhr. [l] Sulfur Electrolysis. [m]Water Electrolysis.

Levelized Cost of Hydrogen production via the Steam Methane Reforming and Sulfuric Acid Production via the Contact Process

CapEx and OpEx data for an SMR plant that produces 341,448 kg/dy H_2 were taken directly from the National Renewable Energy Laboratory H2A model. These numbers were plugged into our LCH equation to determine an LCH from SMR under the same assumptions. The resulting LCH was $1.25 in 2018 USD, ten cents higher than the H2A value. A summary of OpEx and CapEx can be found in Table S4.

Table S4: Tabulated CapEx and OpEx values from the H2A study adjusted to 2018 USD using 2% annual inflation.

Plant Parameters	
Plant Lifetime[a]	40
Plant Output[b]	341,448
OpEx[c]	
Variable OpEx	$9,260,972
Fixed OpEx	$65,746,517
Unplanned Maintenance	$1,265,773
Scheduled Maintenance	$1,289,823
Total OpEx[c]	**$77,563,087**
CapEx[d]	
Plant CapEx	$258,537,342
Total CapEx[d]	**$258,537,342**

Notes: [a]years [b]kg H_2/day [c]2018 USD/yr [d]2018 USD

CapEx and OpEx data were taken from a previous analysis where CapEx was estimated using Fig. S1 and converted into 2018 USD[50]. Wages were converted into an average chemical plant engineer wages in the US and sulfur and sulfuric acid prices and associated laboratory, supervision, and overhead costs were adjusted for consistent assumptions (laboratory costs: 23 % of operating labor, supervision: 20% of operating labor, and plant overheads: 50% operating labor)[50]. We then plugged these CapEx and OpEx assumptions in eq. 8 from the main text assuming a 12% rate of return. It was found that the levelized cost of sulfuric acid was \$0.139/kg H_2SO_4 or \$6.83 for the 49 kg H_2SO_4 that would be co-generated with a kg of H_2 via SMR. Data used for this analysis is shown in table S4 below. All labor costs were scaled by a ratio of the cost of the 216 tonne/dy H_2SO_4 plant from the reference to the size of the plant we modeled herein. Consumable materials costs were scaled by the ratio of the produced sulfuric acid. Sulfur prices were set at \$130/tonne consistent with assumptions in our model.

Table S5: Tabulated CapEx and OpEx values were adjusted to 2018 USD using 2% annual inflation[50].

Plant Parameters	
Plant Lifetime[a]	40
Plant Output[b]	9,817
Variable OpEx[c]	
Sulfur (3,200 MTPD)	\$152,106,074
Electrciity	\$53,971,581
Heating oil	\$30,487,096
Steam	\$201,524,876
Other Utilities	\$29,160,096
Catalyst	\$2,389,128
Total Variable Total OpEx[c]	**\$469,638,853**
Fixed OpEx[c]	
Maintenance	\$1,520,560

Operating Labor	$31,190,845
Laboratory Costs	$7,173,894
Supervision Cost	$6,238,169
Plant Overheads	$15,595,422
Executive Wages	$925,622
Total Fixed OpEx	**$62,644,514**
Indirect OpEX	$97,040,496
Total OpEx[c]	**$159,685,010**
Capital Expenditure[d]	
Plant CapEx	$15,205,600
Catalyst capex	$2,831,096
Total CapEx [d]	**$18,036,696**

Notes: [a]years [b]tonnes H_2SO_4/day [c]2018 USD/yr [d]2018 USD

Comparison to Water Electrolysis

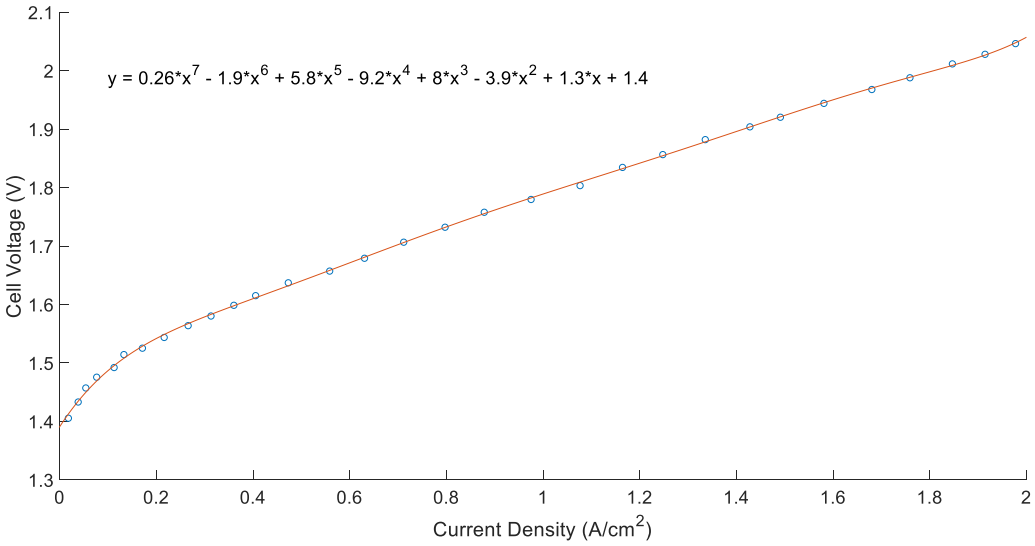

Fig. S7. Graph of WE Voltage and Current Density Relationship. Data interpolation of a real industrial scale water electrolyzer[64]. The interpolated relationship can be found in Eq. S7.

The empirical relationship between cell voltage (V) and current density (CD) may be found below.

$$V = 0.26*CD^7 - 1.9*CD^6 + 5.8*CD^5 - 9.2*CD^4 + 8*CD^3 - 3.9*CD^2 + 1.3*CD + 1.4 \quad (S7)$$

Key Technical Challenges for SE

Poor solubility of SO_2 in concentrated sulfuric acid

Reaching the valuable >69% sulfuric acid concentrations purely electrochemically in all demonstrated SDEs known to these authors requires, at some point in the flow cell, dissolution of SO_2 in highly concentrated sulfuric acid[51,55,67]. The solubility of SO_2 decreases with increased sulfuric acid concentration which leads to increased cell voltages. Engineering controls which increase the solubility of SO_2, possibly using a gas diffusion electrode or temperature controls, may further reduce the cost of SE. In this model, demonstrated data was used which accounted for this solubility, however further stability testing may be necessary to determine how important SO_2 concentration is in the long term.

Membrane hydration issues with concentrated sulfuric acid

When >40% sulfuric acid concentrations exist in the electrolyzer, the membrane which is necessary to prevent wasteful redox shuttling, may dehydrate and therefore become highly resistive. Two strategies have been used in the literature to account for this, one is using membranes that do not depend heavily on hydration (e.g. polybenzimidazole type membranes) or ensuring that the pressure in the catholyte chamber is higher than the pressure in the anolyte chamber thus forcing hydration of the membrane[68,69]. Production of sulfuric acid in >90% sulfuric acid has been demonstrated in these systems, however, only at very high overpotentials, low current densities, and for short times and more testing and engineering is likely necessary to determine if this is actually feasible therefore we decided to not include the electrochemical production of >90% sulfuric acid in our model[70].

Catalyst Fouling with Reduced Sulfur Species

Elemental sulfur may plate on catalysts both reductively and oxidatively. If there is leakage of SO_2 across the membrane, SO_2 may reduce to S_x and block active sites on the cathode[71]. In the anodic chamber, if any (poly)sulfides are present in solution, these may oxidatively plate out on the anode as S_x, again causing fouling[72]. Certainly, membrane integrity and oxygen pressure in the furnace should be controlled precisely to prevent SO_2 in the catholyte and (poly)sulfides in the anolyte. In this analysis we assumed that catalyst fouling was well controlled and catalyst replacement was only necessary once every seven years. No sulfur electrolysis system has been run for this long, however, so we used the chlor-alkali process as a guide which has similar fouling issues. Under these assumptions, our catalyst and membranes were replaced once every seven years.

Sensitivity Analysis of Grid-Assisted Sulfur Electrolysis

Even though grid-assisted SE is cheaper than SMR under standard model assumptions, we applied a sensitivity analysis to understand how the price could be reduced further. The order of sensitivities is somewhat different than for solar-only SE plant (fig. 7) because the grid assisted plant is far lower CapEx and OpEx than the solar-only plant. The CapEx for the grid-assisted plant is lower because the grid assisted plant does not need to install extra electrolyzers or batteries to account for the sun's variability and intermittency. The grid-assisted plant's OpEx is lower than the solar-only plant's OpEx because maintenance is 3% of annual CapEx and the solar-only plant has very high CapEx. The discount rate compounds annually meaning that high OpEx plants have high sensitivity to discount rates. While both grid-assisted and solar-only SE plants have high OpEx, the solar-only plant has relatively higher OpEx and is therefore most sensitive to the discount rate while that discount rate is only the second largest sensitivity for the grid assisted plant (figs 7 and S8). The largest cost for the grid-assisted plant is the balance of systems, and therefore, the grid assisted plant is most sensitive to this parameter (fig. 8). The third largest sensitivity for the grid-assisted plant is the price of electricity. Because the price of electricity for the grid assisted plant is higher than for the solar-only system, electricity has a large bearing on the sensitivity to electricity price of the grid-assisted plant (fig 7 and S8). The electrolyzer module is the largest component of CapEx, and therefore the grid-assisted plant is highly sensitive to it (fig. 8). A voltage change reduces the amount of energy that is consumed, but does not reduce the price of the energy consumed per unit energy. Given that SE is bound by a minimum thermodynamic energy requirement that is fairly close to the operating voltage, voltage decreases are important, but not as important as electricity price for the grid-assisted plant. The solar-only system, however, is more sensitive to voltage changes because lower voltage means fewer batteries need to be installed and therefore lower CapEx (fig. 7). In both the solar-only and grid assisted cases the remaining sensitivities are very small and have to do with catalyst parameters that are already very good (i.e. stability and faradaic efficiency) and the price of PV which is already very low.

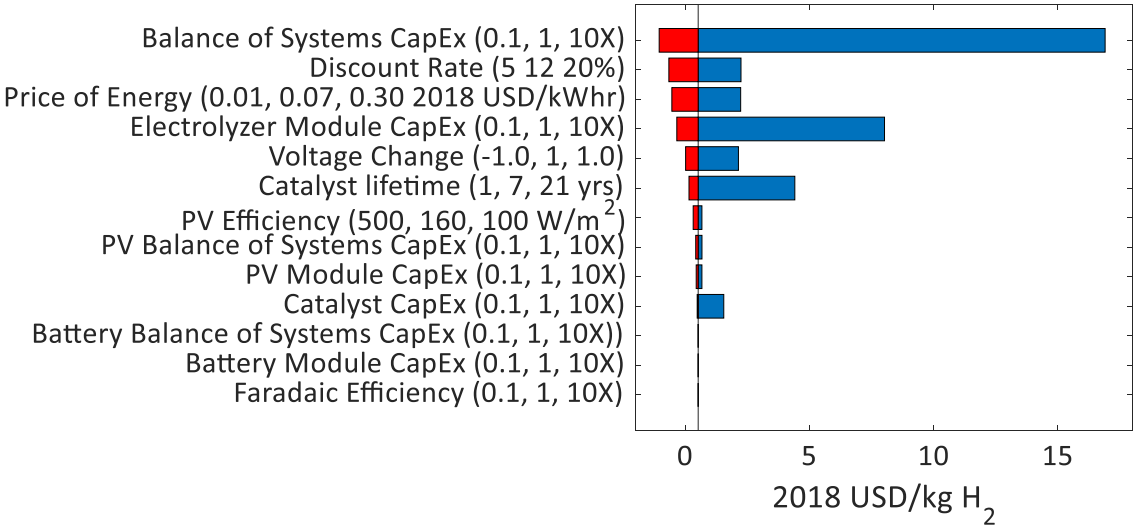

Fig S8. Sensitivity Analysis of Grid Powered Sulfur Electrolysis. The parenthetical numbers on the vertical axis indicate the low, standard, and high assumption for each case.

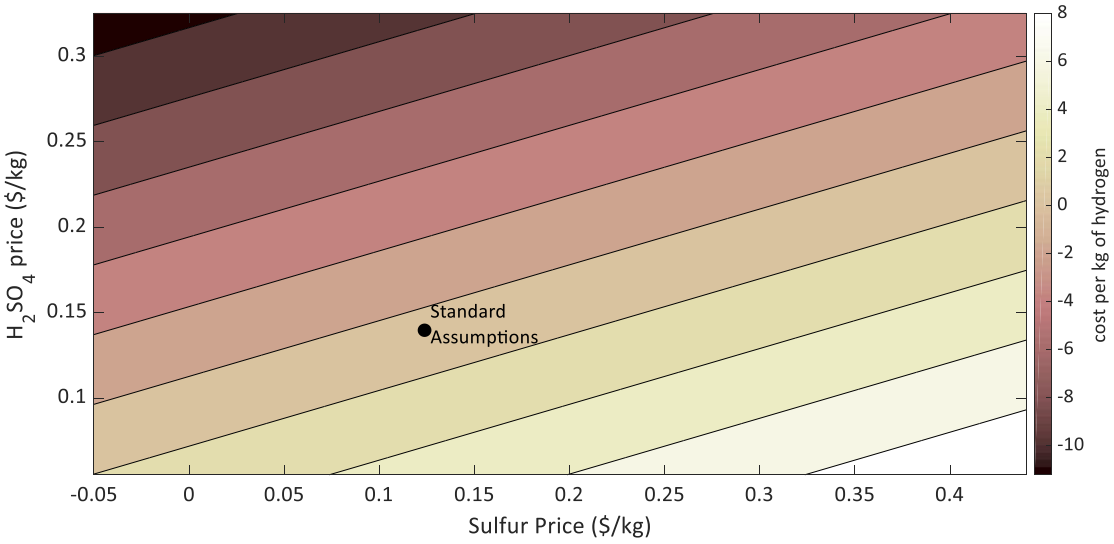

Fig. S9. Sulfur and Sulfuric Acid Sensitivity Analysis. Plot of the price of hydrogen minus a sulfuric acid credit. Black contours are every $2. The black circle indicates the price of hydrogen under standard model assumptions ($0.52).

Correspondence with Sinopec Nanjing Chemical Company May be found in the pdf labeled: NanjingCorrespondence_report.pdf.

All code for this model has been uploaded to the repository.

Chapter 5

Conclusions and Future Work

In this thesis, I have presented work focused on addressing global environmental problems by developing strategies to reduce the cost of technological solutions. In each of the chapters, I work on electrochemical technologies as with the rise of renewable electricity, one strategy to fight climate change is to turn previously thermochemical processes into electrochemical processes. I take a different approach in each chapter. First, I work on a maintenance solution to make the balance of systems cheaper. Next, I take an active component approach by working directly on the electrocatalyst. Finally, I take a systems level approach by attempting to find a new way to address the problem at hand with a different system. I present my conclusions from each chapter here followed by an outlook on the state of electrifying the production of hydrogen.

I have learned through working with private companies to commercialize the technologies in the Hoffmann lab, that when evaluating new technologies, it is important to ask the following questions:

1. *How much cheaper can this system be?*
2. *What can be done to make this system cheaper without sacrificing the scientific and environmental benefit?*
3. *Is there a more economically promising way to solve the problem?*

These questions directly outline a strategy for evaluating the potential impact of any research project. First, perform a techno-economic analysis. Second, determine what the easiest way to make the technology cheaper. Finally, determine if it is reasonable to make it cheap enough to compete in the open market. In academia, if we want the technologies that we work on to make a real impact, applying these questions could be a good place to start.

Chapter 2: Non-Sewered Sanitation

Chapter Two describes my work that may allow for efficient maintenance of a non-sewered sanitation system which has the potential to make off-grid, decentralized, electrochemical wastewater treatment cheaper. I argue that maintenance is an important cost factor in making a system economical and sustainable. This culmination of this work led to the company, Eram

Scientific, agreeing to develop this maintenance technology to integrate into their existing electrochemical, non-sewered, wastewater treatment system. However, while improved maintenance would certainly make the system cheaper, it is still unclear whether or not my maintenance technology would reduce costs enough to allow non-sewered sanitation to enter the mainstream market.

More recent data indicates that regardless of maintenance, these technologies are not cheap enough to be adopted by customers in the developing world and a different technology may be necessary to solve the wastewater treatment problem. Eco-san is a Chinese company that has developed a commercial product using the Caltech wastewater treatment technology. Eco-san estimates that their non-sewered sanitation system, among the cheapest commercially available decentralized options, costs a user around $0.02 per flush to treat wastewater.[22] People in the United States pay between $0.001 and $0.01 per flush for wastewater treatment[73]. This means that with current technology, if people used the Caltech treatment system, people in low income countries would need to pay at least double if not 200X what people in the Unites States pay for wastewater treatment on a per-flush basis. A rigorous techno-economic analysis of the Caltech and other non-sewered sanitation systems should be done to determine how much maintenance costs and how much a maintenance technology could reduce the costs of non-sewered sanitation. However, based on order of magnitude estimates from water electrolysis technologies, improving maintenance is unlikely to make the system 2X cheaper let alone 200X cheaper. A sensitivity analysis of costs would help direct research into how to reduce costs but given staggeringly large gaps in the price of the Caltech non-sewered treatment system versus the cost of a sewer system in the United States, we may need to find new strategies to solve the wastewater treatment problem.

One potential system level change to a non-sewered sanitation system is non-sewered centralized wastewater treatment instead of small scale units. In the absence of sewers, centralized sanitation may be achieved by using vacuum trucks or other non-sewered technologies. Cost estimates for these technologies are more like $0.002 per day, similar to what is paid in the United States.[22] However, people in low-income countries where non-sewered sanitation is necessary may not be able to pay the same as what is paid in the United States. A rigorous analysis of willingness to pay for sanitation would be a valuable addition to this work to provide benchmarks for researchers

to investigate the feasibility of potential technologies and determine the best way to solve the problem of water treatment in the developing world.

Chapter 3: Tuning Electrode Parameters

In Chapter Three, I discovered and characterized a method to tune the stability and activity of electrodes via deposition of thin layers of TiO_2. In unpublished work, I have also shown that this technique may be used to tune faradic efficiency. I proposed a group electronegativity based theory to understand how this process works; group electronegativity works just as well as binding energies for understanding the activity of oxygen evolution reaction electrocatalysts. This indicates that group electronegativity could be a very useful design tool for future researchers, especially if they are able to use thin layers to easily tune the technology catalyst parameters using group electronegativity as a guide.

The next step in this work should be to understand if using molecularly thin layers to tune electrocatalytic parameters is a general phenomenon. A detailed mechanistic study should be done to determine how thin layers may affect the activity of underlying catalysts and by which mechanism. Understanding this mechanism may allow scientists to build an optimal dimensionally stable anode for both chlorine and oxygen production. This could reduce the cost of many electrolytic systems including Water Electrolysis, the Chlor-Alkali process, and even the Oxygen Evolution Reaction in metal electrowinning. A larger study should also be done to understand how this tool may be used with additional materials and reactions. Finally, experiments using annealing or other catalyst-post processing techniques should be done to explore whether or not tuning catalyst properties using molecularly thin layers could result in a stable change in the catalytic properties on the timescale of years. If properly studied, and found to be long term and widely active, this method could be used in conjunction with a techno-economic sensitivity analysis to optimize any electrochemical system.

My work, as well as many other studies, has shown that, at least for water electrolysis, improvement in any given catalyst parameter (e.g. voltage) may not be enough to make water electrolysis cost competitive with traditional hydrogen production methods like Steam Methane Reforming (SMR).[26] It appears that most efforts in the research community to make water electrolysis a reality, including my own, are centered around the membrane electrode assembly (i.e. catalyst and membrane) while relatively little effort is directed towards the balance of systems for an electrolyzer. Given that the scale of the impact from improving the catalyst would likely not be

large enough to make hydrogen from water electrolysis cheaper than hydrogen from SMR, more research effort should be directed towards improving the cost of the electrolyzer stack.

Chapter 4: Techno-economics of electrochemical hydrogen production

In the final chapter of my thesis, I abandon water electrolysis as a strategy for making hydrogen because I believe that the economics are not near-term. Instead, I analyzed a cogeneration technology which has the potential to make cheap hydrogen because it uses a single CapEx and OpEx to make two products, hydrogen and sulfuric acid. This analysis provided the first, to my knowledge, industrially relevant hydrogen production strategy that was not currently in use. This strategy could produce hydrogen at a price that was lower than the price of hydrogen made via SMR. This is impactful because it could offer a near term solution to allow for clean hydrogen production which could enter the market without a carbon tax.

These analyses also provided another data point indicating that changing the cost of materials in the catalyst does not significantly impact the price of hydrogen. Therefore, despite suggestions from previous work, the price of the catalyst does not impact the price of the system appreciably for Chlor-Alkli, Water Electrolysis, and Sulfur Electrolysis (cite). This phenomenon should be investigated to determine whether or not it is generally true that reducing the material cost of a catalyst does very little to the cost of electrochemical system. It should be noted, however, at very large scales, rare earth metals (e.g. Ir) may not be abundant enough to be used in electrolysis, and finding different, possibly low cost materials may be important in the distant future.

This study indicates that cogeneration of hydrogen and other commercially valuable materials could be a near term solution to making hydrogen production affordable. Future research should further investigate cogeneration mechanisms.

Synthesis and Outlook

Low Greenhouse Gas Emissions Via Electrification

My work generally recognizes that the global economy transitions to what is cheapest, usually slowly, by building new capacity with the cheapest current technology and only replacing existing technology when it is economical to decommission a plant. It is important to consider the economic realities of any new technology. Here, I will provide further discussion on the potential for clean hydrogen production at an industrial scale.

Hydrogen may become an energy storage molecule or a transportation fuel, but it is currently of highest value as a commodity chemical. As a commodity chemical, clean hydrogen could replace dirty hydrogen as well as other hydrocarbon-based reducing agents (e.g. petcoke and methane). However, this is unlikely to happen if clean hydrogen is not cheaper than dirty hydrogen. My data indicate that water electrolysis is likely not an economically efficient way to make cheap, clean hydrogen. Therefore, new hydrogen generation technologies like methane pyrolysis should be considered. My data indicate that cogeneration of hydrogen and other commodities may also be a near-term, economic way to produce hydrogen. In order to cogenerate hydrogen at a meaningful scale there needs to be a market for the co-product. Unfortunately, by mol, hydrogen is the most demanded commodity chemical on the planet and therefore producing a pure chemical as a co-product would not produce enough hydrogen to replace fossil fuels.

To pair hydrogen generation with a cogeneration product, the coproduct must be produced oxidatively. The largest oxidative commodity chemical is sulfuric acid, which I examine in my work. Unfortunately, the entire demand for sulfuric acid is only 10% of the current molar demand for hydrogen. In my analysis, I chose a sulfuric acid process where it is generated in a 1:1 molar ratio with hydrogen. However, hydrogen and sulfuric acid co-generation is possible at a 3:1 H_2:H_2SO_4 molar ratio.[74] Even with a molar ratio of 4:1, only 30% of the current hydrogen demand could be met by sulfuric acid cogeneration. If the demand for hydrogen rose, even a smaller fraction of hydrogen could be met by this process. Perhaps in a future where ammonia production became electrochemical via reaction of N_2 with H_2O, the demand for H_2 could shrink and these processes could meet the H_2 demand.

The only oxidized material with a higher molar demand than hydrogen is cement which is primarily CaO as a component of cement. For example, a hydrogen generation cycle which cogenerates hydrogen and CaO at a 1:1 molar ratio could make 4X the current demand for hydrogen if this process were to produce all of the cement in the world.[75]

This thesis shows that both catalyst optimization and systems level changes may influence the cost of a given technology. Catalyst level changes are likely not going to be impactful enough to make decentralized non-sewered sanitation or water electrolysis competitive with the current market offerings. I have suggested that system level changes to these technologies be explored and in the

case of hydrogen generation, I modeled a new production strategy. I encourage early economic thinking to guide scientific research in order to more efficiently solve important problems.

BIBLIOGRAPHY

1. Net-zero emissions energy systems | Science. https://science.sciencemag.org/content/360/6396/eaas9793/tab-figures-data.
2. Intergovernmental Panel on Climate Change. *Global warming of 1.5°C*. (2018).
3. Global Nitrous Oxide Production Determined by Oxygen Sensitivity of Nitrification and Denitrification - Ji - 2018 - Global Biogeochemical Cycles - Wiley Online Library. https://agupubs.onlinelibrary.wiley.com/doi/full/10.1029/2018GB005887.
4. The Kyoto Protocol and non-CO2 Greenhouse Gases and Carbon Sinks | SpringerLink. https://link.springer.com/article/10.1023/A:1020910820102.
5. Giant batteries and cheap solar power are shoving fossil fuels off the grid | Science | AAAS. https://www.sciencemag.org/news/2019/07/giant-batteries-and-cheap-solar-power-are-shoving-fossil-fuels-grid.
6. Wilson, M. Lazard's Levelized Cost of Storage Analysis—Version 4.0. 60.
7. Powering the Planet: Where in the World Will Our Energy Come From? - Nate Lewis - 5/25/2005 - YouTube. https://www.youtube.com/watch?v=EUKqx2uk-Gs.
8. British Columbia's Carbon Tax - Province of British Columbia. https://www2.gov.bc.ca/gov/content/environment/climate-change/planning-and-action/carbon-tax.
9. Waltzer, K. The Role of 45Q Carbon Capture Incentives in Reducing Carbon Dioxide Emissions. 3.

10. A Process for Capturing CO2 from the Atmosphere | Elsevier Enhanced Reader. https://reader.elsevier.com/reader/sd/pii/S2542435118302253?token=94C153D93CD1105CB152A64E509F13D1B4BA8AF8CB094A5A14CFC1FC96E505F69DA439AAE6342A3907B24539CB694923 doi:10.1016/j.joule.2018.05.006.
11. Implications for climate and sea level of revised IPCC emissions scenarios | Nature. https://www.nature.com/articles/357293a0.
12. Global water cycle agreement in the climate models assessed in the IPCC AR4 - Waliser - 2007 - Geophysical Research Letters - Wiley Online Library. https://agupubs.onlinelibrary.wiley.com/doi/full/10.1029/2007GL030675.
13. Biological Wastewater Treatment - Google Books. https://books.google.com/books?hl=en&lr=&id=41JButufnm8C&oi=fnd&pg=PA1&dq=biological+wastewater+treatment&ots=nSH1f3xB5i&sig=MqMlR69u-ju3gvnuKxy6keyNnZc#v=onepage&q=biological%20wastewater%20treatment&f=false.
14. Developments in wastewater treatment methods - ScienceDirect. https://www.sciencedirect.com/science/article/pii/S0011916404003558.
15. Breakpoint chlorination and free-chlorine contact time: Implications for drinking water N-nitrosodimethylamine concentrations - ScienceDirect. https://www.sciencedirect.com/science/article/abs/pii/S0043135406004441.
16. Contributions of electrochemical oxidation to waste-water treatment: fundamentals and review of applications - Anglada - 2009 - Journal of Chemical Technology & Biotechnology - Wiley Online Library. https://onlinelibrary.wiley.com/doi/abs/10.1002/jctb.2214.

17. Phosphate Recovery from Human Waste via the Formation of Hydroxyapatite during Electrochemical Wastewater Treatment | ACS Sustainable Chemistry & Engineering. https://pubs.acs.org/doi/abs/10.1021/acssuschemeng.7b03155.
18. Electrochemical disinfection of toilet wastewater using wastewater electrolysis cell - ScienceDirect. https://www.sciencedirect.com/science/article/pii/S0043135416300392.
19. Jasper, J. T., Yang, Y. & Hoffmann, M. R. Toxic Byproduct Formation during Electrochemical Treatment of Latrine Wastewater. *Environ. Sci. Technol.* **51**, 7111–7119 (2017).
20. Lee, D.-Y., Elgowainy, A. A. & Dai, Q. *Life Cycle Greenhouse Gas Emissions of By-product Hydrogen from Chlor-Alkali Plants*. https://www.osti.gov/biblio/1418333 (2017) doi:10.2172/1418333.
21. Shaner, M. R., Atwater, H. A., Lewis, N. S. & McFarland, E. W. A comparative technoeconomic analysis of renewable hydrogen production using solar energy. *Energy Environ. Sci.* **9**, 2354–2371 (2016).
22. Reinvent the Toilet Challenge & Expo - Bill & Melinda Gates Foundation. https://www.gatesfoundation.org/what-we-do/global-growth-and-opportunity/water-sanitation-and-hygiene/reinvent-the-toilet-challenge-and-expo.
23. Christopher, K. & Dimitrios, R. A review on exergy comparison of hydrogen production methods from renewable energy sources. *Energy Environ. Sci.* **5**, 6640–6651 (2012).
24. Wismann, S. T. *et al.* Electrified methane reforming: A compact approach to greener industrial hydrogen production. *Science* **364**, 756–759 (2019).
25. Petroleum Coke. https://www.eia.gov/dnav/pet/PET_PNP_CAPFUEL_A_(NA)_8FPP0_MBBL_A.htm.

26. H2A: Hydrogen Analysis Production Models | Hydrogen and Fuel Cells | NREL. https://www.nrel.gov/hydrogen/h2a-production-models.html.
27. How much carbon dioxide is produced per kilowatthour of U.S. electricity generation? - FAQ - U.S. Energy Information Administration (EIA). https://www.eia.gov/tools/faqs/faq.php?id=74&t=11.
28. webmaster. A Review of Water Scarcity Indices and Methodologies. *The Sustainability Consortium* https://www.sustainabilityconsortium.org/downloads/a-review-of-water-scarcity-indices-and-methodologies/.
29. Falkenmark, M. The Massive Water Scarcity Now Threatening Africa: Why Isn't It Being Addressed? *Ambio* **18**, 112–118 (1989).
30. 2015 - Water for a Sustainable World | United Nations Educational, Scientific and Cultural Organization. http://www.unesco.org/new/en/natural-sciences/environment/water/wwap/wwdr/2015-water-for-a-sustainable-world/.
31. Gerland, P. *et al.* World population stabilization unlikely this century. *Science* **346**, 234–237 (2014).
32. Lackner, K. S. CLIMATE CHANGE: A Guide to CO2 Sequestration. *Science* **300**, 1677–1678 (2003).
33. US EPA, O. Climate Impacts in the Southwest. /climate-impacts/climate-impacts-southwest.
34. The Water Crisis: Poverty and Water Scarcity in Africa. *The Water Project* https://thewaterproject.org/why-water/poverty.
35. Gleick, P. H. Basic Water Requirements for Human Activities: Meeting Basic Needs. *Water Int.* **21**, 83–92 (1996).
36. *Progress on drinking water and sanitation: 2014 update*. (World Health Organization, 2014).

37. Berge, N. D. *et al.* Hydrothermal Carbonization of Municipal Waste Streams. *Environ. Sci. Technol.* **45**, 5696–5703 (2011).

38. Abdeen, S., Di, W., Hui, L., Chen, G.-H. & van Loosdrecht, M. C. M. Fecal coliform removal in a sulfate reduction, autotrophic denitrification and nitrification integrated (SANI) process for saline sewage treatment. *Water Sci. Technol.* **62**, 2564–2570 (2010).

39. Solutions when the Solution is the Problem: Arraying the Disarray in Development - Working Paper 10. *Center For Global Development* https://www.cgdev.org/publication/solutions-when-solution-problem-arraying-disarray-development-working-paper-10.

40. Mobile cellular subscriptions (per 100 people) | Data. https://data.worldbank.org/indicator/IT.CEL.SETS.P2.

41. NW, 1615 L. St, Suite 800Washington & Inquiries, D. 20036USA202-419-4300 | M.-857-8562 | F.-419-4372 | M. Smartphone Ownership Is Growing Rapidly Around the World, but Not Always Equally. *Pew Research Center's Global Attitudes Project* https://www.pewresearch.org/global/2019/02/05/smartphone-ownership-is-growing-rapidly-around-the-world-but-not-always-equally/ (2019).

42. Water Quality and Treatment: A Handbook on Drinking Water, Sixth Edition. *AWWA-American Water Works Association* https://www.awwa.org/Store/{ProductName}/ProductDetail/{ProductId}?productId=6292.

43. Finke, C. E. *et al.* Maintenance self-diagnosis and guide for a self-contained wastewater treatment system. (2017).

44. Ogden, J. M. Prospects for building a hydrogen energy infrastructure. *Annu. Rev. Energy Environ.* **24**, 227–279 (1999).

45. Ave, H. Support for Cost Analyses on. 76 (2011).

46. Techno-Economic Analysis of Methane Pyrolysis in Molten Metals: Decarbonizing Natural Gas - Parkinson - 2017 - Chemical Engineering & Technology - Wiley Online Library. https://onlinelibrary.wiley.com/doi/abs/10.1002/ceat.201600414.
47. Catalytic molten metals for the direct conversion of methane to hydrogen and separable carbon | Science. https://science.sciencemag.org/content/358/6365/917/tab-figures-data.
48. A World of Sulfur. *World Fertilizer* https://www.worldfertilizer.com/special-reports/24122018/a-world-of-sulfur/ (2018).
49. Nieuwenhuyse, A. E. van. *Best Available Techniques for Pollution Prevention and Control in the Eiropean Fertilizer Industry*. vol. 8 (2000).
50. Kumareswaran Subasgar *et al.* Design of a Plant to Manufacture Sulfuric Acid from Sulfur. (2013) doi:10.13140/RG.2.1.1083.2724.
51. Weidner, J. W. Electrolyzer performance for producing hydrogen via a solar-driven hybrid-sulfur process. *J. Appl. Electrochem.* **46**, 829–839 (2016).
52. Nieuwenhuyse, A. E. van. *Best Available Techniques for Pollution Prevention and Control in the European Sulphuric Acid and Fertilizer Industries*. (European FertilizerManufacturers' Association, 2000).
53. Lulu, X., Ping, Z., Songzhe, C. & Laijun, W. Quantitative analysis of the cell voltage of SO2-depolarized electrolysis in hybrid sulfur process. *Nucl. Eng. Des.* **306**, 203–207 (2016).
54. Sulfuric Acid Corrosion | H2SO4 Corrosion | Sulphuric Acids. https://tubingchina.com/Sulfuric-Acid-H2SO4-Corrosion.htm.
55. Gorensek, M. B., Staser, J. A., Stanford, T. G. & Weidner, J. W. A thermodynamic analysis of the SO2/H2SO4 system in SO2-depolarized electrolysis. *Int. J. Hydrog. Energy* **34**, 6089–6095 (2009).

56. Economics and Chemical Engineering. in *Chemical Engineering for Non-Chemical Engineers* 79–87 (John Wiley & Sons, Ltd, 2017). doi:10.1002/9781119369196.ch6.

57. Li, F. *Situation and Practical Data of Sulfuric Acid Vacuum Concentration Unit of NCIC*.

58. EIA - Electricity Data. https://www.eia.gov/electricity/monthly/epm_table_grapher.php?t=epmt_5_6_a.

59. Shaner, M. R., Davis, S. J., Lewis, N. S. & Caldeira, K. Geophysical constraints on the reliability of solar and wind power in the United States. *Energy Environ. Sci.* **11**, 914–925 (2018).

60. Ardani, K. *et al. Installed Cost Benchmarks and Deployment Barriers for Residential Solar Photovoltaics with Energy Storage: Q1 2016*. http://www.osti.gov/servlets/purl/1338670/ (2016) doi:10.2172/1338670.

61. Jechura, J. Hydrogen from Natural Gas via Steam Methane Reforming (SMR). 21.

62. Green Markets. *Green Markets* https://fertilizerpricing.com/pricing-news/green-markets/.

63. Garrett, D. E. *Chemical Engineering Economics*. (Van Nostrand Reinhold, 1989).

64. Pierre Millet *et al.* Implementation of cobalt clathrochelates in polymer electrolyte water electrolysers for hydrogen evolution. *Chem. Eng. Trans.* **41**, 325–330 (2014).

65. O'Brien, T. F., Bommaraju, T. V. & Hine, F. *Handbook of Chlor-Alkali Technology: Volume I: Fundamentals, Volume II: Brine Treatment and Cell Operation, Volume III: Facility Design and Product Handling, Volume IV: Operations, Volume V: Corrosion, Environmental Issues, and Future Developments*. (Springer US, 2005).

66. SUMNER, J., BIRD, L. & DOBOS, H. Carbon taxes: a review of experience and policy design considerations. *Clim. Policy* **11**, 922–943 (2011).

67. Corgnale, C. & Summers, W. A. Solar hydrogen production by the Hybrid Sulfur process. *Int. J. Hydrog. Energy* **36**, 11604–11619 (2011).

68. Jayakumar, J. V. *et al.* Polybenzimidazole Membranes for Hydrogen and Sulfuric Acid Production in the Hybrid Sulfur Electrolyzer. *ECS Electrochem. Lett.* **1**, F44–F48 (2012).

69. Opperman, H., Kerres, J. & Krieg, H. SO2 crossover flux of Nafion® and sFS-PBI membranes using a chronocoulometric (CC) monitoring technique. *J. Membr. Sci.* **415–416**, 842–849 (2012).

70. Khan, H. A. *et al.* Pt encapsulated hollow mesoporous SiO2 sphere catalyst for sulfuric acid decomposition reaction in SI cycle. *Int. J. Hydrog. Energy* **44**, 2312–2322 (2019).

71. Kodera, F., Kuwahara, Y., Nakazawa, A. & Umeda, M. Electrochemical corrosion of platinum electrode in concentrated sulfuric acid. *J. Power Sources* **172**, 698–703 (2007).

72. Davie, M. G., Cheng, H., Hopkins, G. D., LeBron, C. A. & Reinhard, M. Implementing Heterogeneous Catalytic Dechlorination Technology for Remediating TCE-Contaminated Groundwater. *Environ. Sci. Technol.* **42**, 8908–8915 (2008).

73. Author, N. G. *Water and Wastewater Annual Price Escalation Rates for Selected Cities across the United States*. http://www.osti.gov/servlets/purl/1413878/ (2017) doi:10.2172/1413878.

74. Lalvani, S. B. & Dave, B. Simultaneous production of hydrogen and sulfuric acid from aqueous sulfur slurry. *Int. J. Hydrog. Energy* **11**, 639–646 (1986).

75. Ellis, L. D., Badel, A. F., Chiang, M. L., Park, R. J.-Y. & Chiang, Y.-M. Toward electrochemical synthesis of cement—An electrolyzer-based process for decarbonating $CaCO_3$ while producing useful gas streams. *Proc. Natl. Acad. Sci.* 201821673 (2019) doi:10.1073/pnas.1821673116.